



**UNIVERSITY
OF TURKU**

This is a self-archived – parallel-published version of an original article. This version may differ from the original in pagination and typographic details. When using please cite the original.

AUTHOR Sonia Iyer, Shuang Zhang, Simge Yucel, Heiko Horn, Sean G Smith, Ferenc Reinhardt, Esmee Hoefsmit, Bimarzhan Assatova, Julia Casado, Marie-Charlotte Meinsohn, M Inmaculada Barrasa, George W Bell, Fernando Perez-Villatoro, Kaisa Huhtinen, Johanna Hynninen, Jaana Oikkonen, Pamoda M Galhenage, Shailja Pathania, Paula T Hammond, Benjamin G Neel, Anniina Färkkilä, David Pépin, Robert A. Weinberg

TITLE Genetically defined syngeneic mouse models of ovarian cancer as tools for the discovery of combination immunotherapy

YEAR 2020

DOI 10.1158/2159-8290.CD-20-0818

VERSION Final draft

CITATION Genetically defined syngeneic mouse models of ovarian cancer as tools for the discovery of combination immunotherapy.
Sonia Iyer, Shuang Zhang, Simge Yucel, Heiko Horn, Sean G Smith, Ferenc Reinhardt, Esmee Hoefsmit, Bimarzhan Assatova, Julia Casado, Marie-Charlotte Meinsohn, M Inmaculada Barrasa, George W Bell, Fernando Perez-Villatoro, Kaisa Huhtinen, Johanna Hynninen, Jaana Oikkonen, Pamoda M Galhenage, Shailja Pathania, Paula T Hammond, Benjamin G Neel, Anniina Färkkilä, David Pépin, and Robert A. Weinberg. *Cancer Discov* November 6 2020 DOI: 10.1158/2159-8290.CD-20-0818.

Genetically defined syngeneic mouse models of ovarian cancer as tools for the discovery of combination immunotherapy.

Sonia Iyer¹, Shuang Zhang², Simge Yucel¹, Heiko Horn^{3,4}, Sean G. Smith⁵, Ferenc Reinhardt¹, Esmee Hoefsmit¹, Bimarzhan Assatova¹, Julia Casado⁶, Marie-Charlotte Meinsohn⁴, M. Inmaculada Barrasa¹, George W. Bell¹, Fernando Pérez-Villatoro⁶, Kaisa Huhtinen⁷, Johanna Hynninen⁸, Jaana Oikkonen⁶, Pamoda M Galhenage⁹, Shailja Pathania⁹, Paula T. Hammond⁵, Benjamin G. Neel², Anniina Farkkila^{6,10}, David Pépin^{4*} and Robert A. Weinberg^{1*}

¹Whitehead Institute for Biomedical Research, Cambridge, MA, ²Laura and Isaac Perlmutter Cancer Center, NYU-Langone Medical Center, NY, ³Stanley Center, Broad Institute of MIT and Harvard, Cambridge, MA, ⁴Pediatric Surgical Research Laboratories, Massachusetts General Hospital; Department of Surgery, Harvard Medical School, Boston, MA, ⁵Marble Center for Cancer Nanomedicine, Koch Institute for Integrative Cancer Research, Massachusetts Institute of Technology, Cambridge, MA, ⁶Research program in Systems Oncology, University of Helsinki and Helsinki University Hospital, ⁷Institute of Biomedicine and FICAN West Cancer Centre, University of Turku, Turku, Finland, ⁸Department of Obstetrics and Gynecology, University of Turku and Turku University Hospital, Turku, Finland, ⁹Center for Personalized Cancer Therapy, University of Massachusetts, Boston, MA, ¹⁰Dana-Farber Cancer Institute Harvard Medical School, Boston, MA,

Corresponding authors- David Pépin^{4} (DPEPIN@mgh.harvard.edu) and Robert A. Weinberg^{1*} (weinberg@wi.mit.edu)

Conflict of interest

S.I. is currently an employee at AstraZeneca as of May 26th, 2020. S.I. received no funding from AstraZeneca. P.T.H. is a co-founder and member of the Board of Directors of LayerBio, Inc. She is on the Scientific Advisory Board of Moderna, Inc. and the Board of Directors of Alector, Inc., and she receives consulting fees and holds equity in these companies. P.T.H. is not aware of any conflicts of interest concerning the content and topic of the manuscript and these entities. B.G.N. is a co-founder, holds equity in, and is a member of the Scientific Advisory Board at Navire Pharmaceuticals. He also holds equity in and is a member of the Scientific Advisory Board at Avrinis, Inc. B.G.N. was an expert witness for the Johnson and Johnson ovarian cancer talc litigation in U.S. Federal Court. His spouse has equity in Amgen, Avrinis, Inc, Gilead Sciences, and Regeneron. R.A.W. is a scientific advisor for and holds equity interest in Verastem, Inc. The other authors declare no conflicts of interest.

Abstract

Despite advances in immuno-oncology, the relationship between tumor genotypes and response to immunotherapy remains poorly understood, particularly in high-grade serous ovarian cancer (HGSC). To address this gap, we developed a series of mouse models of this disease that carry some of the genotypes of human HGSCs and can grow in syngeneic immunocompetent hosts. We transformed murine fallopian tube epithelial cells to phenocopy homologous recombination-deficient tumors through the combined loss of *p53*, *Brca1*, *Pten*, *Nf1*, and overexpression of *Myc* and mutant *p53*^{R172H}, which was contrasted to an otherwise identical model carrying *Brca1* wild-type alleles. In a second panel, modeling homologous recombination-proficient tumors, we constructed genotypes bearing combinations of loss of *p53*, and overexpression of *Ccne1*, *Akt2*, mutant *p53*^{R172H}, and mutant *KRAS*^{G12V}, as well as variants of this model, overexpressing *Brd4* or *Smarca4* instead of *KRAS*^{G12V}. When implanted into C57BL/6 hosts, these cells form tumors recapitulating human disease, including genotype-driven differences in response to treatment. Strikingly, we identified clones of the homologous recombination-proficient model that exhibited resistance to checkpoint inhibitors in a follistatin-dependent manner. These data provide proof of concept that our novel genetically defined models can identify new therapeutic targets modulating resistance to immunotherapies in HGSC.

Statement of significance

We engineered a panel of murine fallopian tube epithelial cells bearing mutations typical of high-grade serous ovarian cancer and capable of forming tumors in syngeneic immunocompetent hosts. These models recapitulate tumor microenvironments and drug responses characteristic of human disease. In a *Ccne1*-overexpressing model, immune checkpoint resistance was driven by follistatin.

Running Title- Genetically defined high grade serous ovarian cancer models

Introduction

High grade serous ovarian cancer (HGSC) is characterized by significant structural genomic changes and almost-universally mutated *TP53* gene (1). More than 50% of HGSCs have defects in the homologous recombination-dependent repair (HR) pathway primarily associated with genetic and epigenetic alterations of HR pathway genes, such as *BRCA1*, *BRCA2*, and *PTEN*. HGSCs with defective HR initially respond well to platinum-based chemotherapy and poly (adenosine diphosphate-ribose) polymerase (PARP) inhibitors (2). A second, distinct subgroup of ovarian tumors involves approximately 20% of the clinically encountered HGSCs. These tumors exhibit Cyclin E1 (*CCNE1*) gene amplification, exhibit an intact HR pathway (3) and are associated with a worse response to platinum-based chemotherapy and inferior clinical outcomes (3,4). This explains why there is an urgent need to develop new therapeutic interventions for the treatment of the various HGSC tumor subtypes, particularly the HR-proficient subgroups.

Immuno-oncology approaches that reverse the immune-suppressive microenvironments of tumors have successfully unleashed the immune system against several tumor types. Still, their successes have been limited in the case of HGSCs (5,6). Thus, recent clinical data regarding the efficacy of single-agent immune checkpoint blockade (ICB) therapies indicate limited benefit in recurrent ovarian cancer (7,8) compared to other tumor types. Precisely why this is the case remains poorly understood, highlighting the need to study the underlying biology of immune evasion in ovarian cancer using immunocompetent animal models. Unfortunately, until now, the preclinical models required to address questions regarding the contribution of specific HGSC genotypes to immune evasion have been limited. Moreover, since the responses to ICB vary by genotype (9), models that recapitulate the various genomic profiles observed in HGSC are needed.

Currently used models to study HGSC include patient-derived xenografts (PDXs) growing in immunodeficient hosts, which limits the study of tumor-immune interactions (10). In contrast, syngeneic models, such as the commonly used ID8 murine model (11), together with genetically modified versions of these cells (12,13), have been extensively used to investigate the roles of the immune system in HGSC progression and to study therapeutic responses. Nonetheless, the ID8 model does not carry the common mutations and somatic copy number alterations that are observed in human HGSCs (12). Over the years, several genetically engineered transgenic mouse models (GEMM) models (14-17) have been developed, including those derived from fallopian tube epithelial (FTE) cells—the presumed normal cells-of-origin of HGSCs (17-19); while

useful, complex combination genotypes are laborious to construct via crosses between germline mutation-bearing mouse strains. Moreover, such models lack the flexibility to control the timing of tumor outgrowth, rendering them less suitable as preclinical models.

Herein, we generated genetically distinct HGSC cell line models bearing genetic alterations that are representative of human tumors and can be propagated in fully immunocompetent, syngeneic mouse hosts. We selected the most common combinations of co-occurring mutations observed in the homologous recombination (HR)-deficient spectrum and the HR-proficient spectrum HGSC patient samples from The Cancer Genome Atlas (TCGA). We introduced them into $p53^{-/-}$ or $p53^{-/-}Brca1^{-/-}$ mutant (20) FTE cells of C57BL/6 mice using the CRISPR/Cas9 methodology to introduce bi-allelic deletions and/or lenti- or retroviral gene transduction to model overexpression. These proof-of-concept preclinical models allowed us to characterize the influence of certain mutational spectra on the tumor-immune microenvironment and to test new combinations of standard therapies and immunotherapies. Given the unrealized potential of ICB and resistance to current therapies in HGSC, models such as these could reveal novel treatment strategies and identify therapeutic targets to improve the response rates of women under treatment.

Results-

Generating and validating the engineered murine-FTE derived cells with clinically relevant driver mutations

To produce transformed murine-fallopian tube epithelial (m-FTE) cells bearing patient-relevant mutant genotypes, we identified the most common combinations of mutations observed in homologous recombination (HR)-deficient spectrum and HR-proficient spectrum HGSC patient samples listed in The Cancer Genome Atlas (TCGA) dataset (**Supplemental Figure 1A**). The generation of HR-deficient spectrum genotypes are shown in **Figure 1 A**. The BPPNM ($p53^{-/-}R172HBrca1^{-/-}Pten^{-/-}Nf1^{-/-}Myc^{OE}$ genotype) is HR deficient, and the PPNM ($p53^{-/-}R172HPten^{-/-}Nf1^{-/-}Myc^{OE}$ genotype) cell line does not correspond precisely with a known HR-deficient human HGSC genotype is therefore deemed "non-classified (**Figure 1A**). For the HR-proficient cell lines, we overexpressed combinations of *CCNE1*, *AKT2*, *BRD4*-short isoform, and *SMARCA4* genes, as well as a *KRAS*; these mutant alleles are observed clinically in HGSC tumors with frequencies of 19%, 6%,12%,10%, and 12%, respectively (**Supplemental Figure 1A**). Derivation of the HR proficient genotypes is shown in **Figure 1 B**. Of note, *KRAS* G12V-activating mutation were introduced in the cells to model overexpression (21).

We confirmed the introduced genetic alterations at both the gene and protein levels. Genomic assays were used that were appropriate to the mutant allele being analyzed. *Brca1*^{-/-} (**Supplemental Figure 1B**), *p53*^{R172H} mutation (**Supplemental Figure 1C**), and *KRAS*^{G12V} mutation (**Supplemental Figure 1D**) were confirmed using PCR-based analyses. CRISPR-mediated deletion of *Pten* and *Nf1* in the BPPNM and PPNM cell lines was confirmed using the Surveyor assay (22) (**Supplemental Figure 1E**). Protein expression was confirmed using western blot analyses and compared to known HGSC cell lines harboring similar mutations (**Supplemental Figure 1F-G**).

To validate the functionality of the mutations that we had introduced into the engineered m-FTEs cells, we performed western blot analyses of the downstream signaling phosphoproteins targets. In the BPPNM and PPNM cells, loss of *Pten* and *Nf1* genes led to increased AKT, mTOR, and ERK1/2 activation (**Supplemental Figure 1H**). m-FTEs cells harboring the *p53* mutation failed to induce p21 expression upon nocodazole treatment in contrast to corresponding *p53* wild-type cells (Supplemental Figure 1I). Additionally, to test the functionality of the KPCA *Kras*^{G12V} overexpressing expressing cell line, we gauged the drug sensitivity *in vitro* to the EGFR inhibitor Erlotinib (23) (**Supplemental Figure 1J**). To summarize these results, validation of downstream target activation confirmed the expression of mutant *K-Ras* and *p53* alleles, and the loss of functional *Pten* and *Nf1* genes led to anticipated changes in biochemical and biological responses.

We also used immunofluorescence (**Figure 1C**) to verify the continued expression in all of the cell lines of the key FTE markers Pax8 and cytokeratin-7 (CK7) (17-19). To determine the HR DNA damage repair efficiency, we tested Rad51 nuclear focus formation in response to ionizing radiation (IR) (**Figure 1D**). As anticipated, the HR-deficient BPPNM cell line and the non-classified PPNM cells showed fewer Rad51 nuclear foci relative to HR-proficient cells (**Figure 1D**).

We further explored allelic imbalance profiles to assess genomic scarring associated with HR deficiency using shallow whole-genome sequencing in the engineered m-FTEs cells. Loss of Heterozygosity (LOH) is an allelic imbalance signature specific for HR-deficiency as a result of uniparental disomy due to inaccurate repair of sister chromatids during the S/G2 phase of the cell cycle in HR deficient cells (24-26). Consistently, the BPPNM cells exhibited the highest number of LOH events amongst the engineered m-FTEs cells (**Supplemental Figure 2A-B**). Of additional interest, the SPCA cells had the highest number of LOH events amongst the HR-proficient

mutation harboring cell lines. These findings confirm the predicted HR- DNA repair capacities of the engineered m-FTE cells.

Engineered m-FTE cells exhibit expected drug sensitivities *in vitro*

We proceeded to evaluate the *in vitro* drug sensitivities of the HR-deficient BPPNM and the PPNM cell lines as well as the HR-proficient BPCA, SPCA, and KPCA cell lines. As predicted by their respective genotypes, the *Brca1*-deficient cell line, BPPNM were more sensitive to both Carboplatin and Cisplatin and PARP inhibitors, Olaparib and Niraparib, than the *Brca1* wild-type PPNM and HR-proficient cell lines, BPCA, SPCA, and KPCA (**Figure 1E-F, Supplemental Figure 2C-D**). Of note, the p53-null cells (devoid of any other additional introduced mutations) were similarly sensitive to carboplatin and cisplatin treatments *in vitro* to the BPPNM cells.

Despite evidence in the literature suggesting that loss of *PTEN* sensitizes cells to PARP inhibitors (27-29), PPNM cells, which lack *PTEN* function, were not unusually sensitive to PARP inhibitors (**Figure 1F**). We also evaluated the CHK1 inhibitor, Prexasertib (LY2606368), which is known to trigger replication catastrophe (30) and is currently in clinical trials in HGSC patients (31). We observed similar sensitivity to Prexasertib in all of the lines with IC50 values of 2-6 nM regardless of genotype (**Figure 1G**). In the BRD4-overexpressing cell line (BPCA), we evaluated the responses to several BET bromodomain inhibitor/epigenetics targeting drugs, such as Birabresib (OTX015), CPI-203, and JQ1. The BPCA cells were more sensitive to CPI-203 and JQ1 than the SPCA cells, with the A2780 human ovarian cancer cell line serving as a positive control (**Supplemental Figure 2E-G**). The nonlinear regression analyses, including the IC50 for the drugs and cell lines mentioned above, are summarized in **Supplemental Table 1**. Given their faithful modeling of the drug sensitivities of the corresponding human diseases, we chose to focus on their *in vivo* characterization.

Engineered m-FTE cells recapitulate the histopathological and clinical features seen in HGSC patients

We next sought out to determine the tumorigenic potential of the engineered m-FTE cells in immunocompetent C57BL/6 hosts (**Figure 2A**). The HGSCs most often present clinically as metastases disseminated throughout the abdominal cavity (32,33), which was recapitulated in our murine cell lines (**Figure 2B**). The comparative Kaplan–Meier survival curves of mice bearing the genetically defined engineered cell lines are depicted in **Figure 2C-D** and are summarized in

Supplemental Table 2. We also confirmed that the BPPNM, PPNM, BPCA, SPCA, and KPCA tumors growing in syngeneic C57BL/6 hosts recapitulated typical HGSC histopathology (**Supplemental Figure 2H** and **Figure 2E**). In the work described below, we chose to focus on BPPNM, PPNM, and KPCA lines for further characterization.

To begin, we determined the responses of host mice implanted with the BPPNM, PPNM, or KPCA cells and treated with either single-agent Carboplatin (30 mg/kg), Olaparib (50 mg/kg), or Prexasertib (10 mgs/kg) (**Figure 2F**). As expected, single-agent Carboplatin was the most effective in the BPPNM tumor model, extending median survival to 116 days versus 56 days for the vehicle-treated controls ($p < 0.02$). (**Figure 2G**). Mice implanted with BPPNM cells also displayed a trend for a modest response to single-agent Olaparib (median survival 67 days) relative to the vehicle-treated control group (median survival of 56 days). In contrast, PPNM and KPCA did not exhibit any survival benefit in response to Olaparib (**Figure 2H**).

In the KPCA tumor-bearing mice, single-agent Prexasertib elicited a statistically significant prolongation of median survival to 46 days, relative to the vehicle-treated control group (median survival of 35 days, $p < 0.0038$). In contrast, mice bearing BPPNM and PPNM tumors did not exhibit any apparent beneficial response (**Figure 2I**). These *in vivo* results (**Figure 2G-H**) were consistent with the *in vitro* cytotoxicity responses of the BPPNM, PPNM, and KPCA cell lines (**Supplemental Table 1**) and supported the clinical fidelity of these models, including the chemotherapy resistance of the HR-proficient spectrum genotypes.

Ovarian tumors with different genotypes evoke distinct immune microenvironments

To characterize the cellular microenvironment of the BPPNM, PPNM, and KPCA models, we surveyed cell types and cell states using single-cell RNA sequencing (scRNA seq) (34) (**Figure 3A** and **Supplemental Figure 3A**). In doing so, we identified transcriptionally distinct clusters corresponding to innate immune, adaptive immune, carcinoma, and stromal/non-immune mesenchyme cell types (**Figure 3A-B**) using previously described markers (see **Supplemental Table 3-4**). In all three tumor models, omental metastases were dominated by cells identified as either neoplastic or myeloid with substantial proportions of stromal neutrophils and lymphoid cells (**Figure 3A-B**). The scRNA seq also indicated dramatically higher infiltration of myeloid cells in the BPPNM tumors, 44.5% compared to approximately 19.8%, and 24.3% in PPNM and KPCA tumors, respectively (inset of **Figure 3A**).

We performed immune profiling and validation of the scRNAseq at the protein level using multi-parameter flow cytometry and immunohistochemistry (**Figure 3C-D and Supplemental Figure 3B-E** and see **Supplemental Figure 4A-D** for flow cytometry gating strategies). The BPPNM tumors were the most inflamed, with elevated proportions of CD3e-positive T-cells relative to PPNM tumors (2.3-fold higher $p < 0.017$) and KPCA tumors (3.7-fold higher, $p < 0.0001$). The BPPNM tumors also exhibited elevated proportions of CD8⁺ T-cells relative to KPCA tumors (6.9-fold higher, $p < 0.004$). The BPPNM tumors were also heavily infiltrated with CD11c tumor-associated macrophages (TAMS) (35), which comprised 18% of all analyzed cells, a value that was significantly higher than PPNM- (4.3-fold higher) and KPCA- (2.6-fold higher) tumors. The KPCA tumors exhibited considerably higher proportions of Ly6G⁺Ly6C⁺ myeloid cells (3.5-fold higher, $p < 0.0175$) and Ly6G^{low}/Ly6C^{high} granulocytic myeloid cells (5.4-fold elevated relative in comparison to BPPNM tumors, $p < 0.0073$) (**Figure 3C**).

Exhaustion markers on CD8 T-cells were co-expressed (36,37) in all of the tumor types. However, highly exhausted CD8 T-cells co-expressing PD-1, TIGIT, and TIM-3 were significantly elevated in the KPCA tumors, comprising 31% of all CD8⁺ T-cells; this represented a value of nearly 10-fold higher than that observed in the BPPNM tumors ($p < 0.024$, **Supplemental Figure 3C**). In addition to characterizing the immunophenotypes, we evaluated PD-L1 expression, which was elevated in the KPCA and BPPNM tumors relative to PPNM tumors, suggesting distinct genotype-driven immunosuppressive mechanisms. We also used immunohistochemistry to confirm the results of our flow cytometry analysis (**Supplemental Figure 3E**). Altogether, these data indicated that T-cell suppression in BPPNM tumors is heavily influenced by myeloid cells, especially M2-like macrophages (**Supplemental Figure 3B**). In contrast, CD8 T-cell function in KPCA tumors is suppressed via Tregs and immunosuppressive Ly6G⁺Ly6C⁺ myeloid cells (38).

Each of the carcinoma cell genotypes also influenced the immune composition of the tumor-associated ascites (**Figure 3D**). Thus, we observed distinct immune cell repertoires within ascites as compared to the corresponding omental metastases, as has been observed in HGSC patients (39). In particular, the ascites of the KPCA tumors were associated with the highest proportion of Tregs — almost 5-fold higher ($p < 0.037$) than in BPPNM ascites. The ascitic fluid in the BPPNM tumor-bearing mice was heavily infiltrated with Ly6G^{high}/Ly6C^{low} granulocytes, which comprised nearly 33% of all cells, suggestive of a highly immunosuppressive immune microenvironment (38). By comparison, less than 17% of cells were Ly6G^{high}/Ly6C^{low} granulocytes in the ascites of the KPCA tumor-bearing mice (**Figure 3D**). The ascites from the PPNM tumor-bearing mice had elevated proportions of highly exhausted CD8 T-cells co-expressing the PD-1, TIGIT, and TIM-3

markers in contrast to KPCA tumors (6.6-fold higher, $p < 0.00037$ **Supplemental Figure 3D**), indicative once again of impaired effector T-cell functions (36,37).

We also performed an extensive analysis of cytokines present in the conditioned media of the three cell lines propagated in culture (39,40). As we found, many cytokines were elevated in the supernatants of BPPNM cultures relative to both PPNM and KPCA cell lines (**Supplemental Figure 3G-H**). Consistent with BRCA1 deficiency in other models (41), there was a 6.5-fold elevation of IFN- γ concentration in BPPNM relative to KPCA ($p < 0.001$) and a 9-fold elevation relative to PPNM ($p < 0.01$). Strikingly, higher levels of known drivers of myeloid and granulocytic chemotaxis and maturation cytokines were present in the BPPNM supernatant medium relative to those of the KPCA cell lines, including 280-fold higher GM-CSF ($p < 0.000006$), 30-fold more G-CSF ($p < 0.0001$), 20-fold more MCP1 ($p < 0.0002$), and an 80-fold elevation of MIP2 ($p < 0.0042$) (**Supplemental Figure 3H**). In light of the known biological effects of these secreted cytokines, we concluded that the BPPNM cells, as gauged by their behavior *in vitro*, induce a strongly immunosuppressive tumor microenvironment *in vivo* composed of specific subsets of myeloid cells.

We compared the above data derived from analyses of conditioned media *in vitro* with the spectrum of cytokines in the ascitic fluid generated by the various tumor-bearing mice *in vivo*, which were quite distinct (**Figure 3E** and **Supplemental Figure 3F**). Thus, the ascites from the PPNM tumor-bearing mice contained the highest levels of TGF β 1, 7-fold elevated relative to ascites in KPCA tumor-bearing mice. In general, however, there were elevated levels of both TGF β 1 and TGF β 2 across the three cell lines (**Figure 3E**). Ascites from BPPNM tumors contained increased concentrations of chemotactic factors relative to ascites formed by KPCA tumors, including MIP-1 β (2.7-fold, $p < 0.017$), Eotaxin/Ccl11 (1.5-fold, $p < 0.032$), and MIP-3 β (2.8-fold, $p < 0.011$). Ascites from KPCA tumors relative to BPPNM also contained elevated concentrations of immunosuppressive IL-6 (4.6-fold higher, $p < 0.04$) and IL-10 (4.4-fold higher, $p < 0.01$) (**Figure 3E**). The putative cellular source of the cell types responsible for secreting the cytokines highlighted above could be inferred from the scRNA seq data, which suggested an outsized contribution of immunosuppressive, tumor-associated myeloid cells to the secretome, which are highly abundant in these tumors (**Figure 3F**). Along with demonstrating dramatic effects of genotype on the spectrum of cytokines released by the various m-FTE cell lines, these analyses indicated that the behavior of these cells *in vitro* does not fully predict the secretory behavior of the corresponding tumors *in vivo*, which also include the contribution of stromal and immune cell types.

Because cytokines are important mediators of the immune microenvironments, we examined the contribution of specific m-FTE-derived cytokines/chemokines that are thought to mediate the recruitment of specific immune cells to the tumor microenvironment. More specifically, we focused on evaluating the effect of functional blocking of GM-CSF and TGF β 1/2/3 on BPPNM- and TGF β 1/2/3 on KPCA- tumors using neutralizing antibodies. In fact, these cytokines were abundant in the conditioned media derived from cultures of the BPPNM and KPCA cell lines (**Supplemental Figure 3G-H**). Using an *in vitro* Transwell chemotaxis assay, we evaluated their effects on immune cell migration (**Supplemental Figure 4E-F**). In the case of the KPCA model, neutralization of TGF β 1/2/3 reduced total CD45+ lymphocyte migration relative to the control ($p < 0.03$) (**Supplemental Figure 4G**); however, no significant suppression of migration by myeloid cells was seen (**Supplemental Figure 4H**). In the BPPNM model, neutralization of GM-CSF suppressed migration of total CD45+ cells ($p < 0.008$) and Ly6G^{high}/Ly6C^{low} granulocytes ($p < 0.01$). Neutralization of TGF β 1/2/3 reduced the migration of Ly6G^{high}/Ly6C^{low} granulocytes relative to the control ($p < 0.007$) and slightly increased macrophage migration relative to control ($p < 0.03$) (**Supplemental Figure 4I-L**). These findings were consistent with the known roles of GM-CSF and TGF β as a chemoattractant for CD45+ myeloid cells and support the notion that genotype-driven differences in chemokine secretion by cancer cells can mediate recruitment of specific immune cell populations to the tumor microenvironment

To determine whether the mouse models described here can recapitulate some of the cytokine profiles found in human HGSOC tumors, we analyzed ascites of 10 *BRCA1/2*- mutated and 7 *CCNE1*- amplified HGSOC patients (<https://www.project-hercules.eu/>). The ascites profiles showed seven cytokines differentially expressed (**Supplemental Figure 3I**), and the profiles also showed high inter-patient heterogeneity characteristic of HGSOC. We next calculated fold-changes of the cytokine expressions between the *BRCA1/2* mutated and *CCNE1* amplified human ascites samples and the corresponding fold-changes between the BPPNM and KPCA mouse models. The heatmap of this comparison is shown in **Supplemental Figure 3J**. Both pairings show similar fold-changes in 17 (65%) out of the 26 cytokines, and opposite trends in nine. Of note, IL-20 levels were significantly lower in *BRCA*- mutated compared to *CCNE1* -driven tumor ascites in both human and mouse samples. Altogether, the scRNA seq, flow cytometry, and ascitic cytokine data combined to describe distinct immunosuppressive microenvironments across the spectrum of the tumor-cell genotypes compared here, this being reminiscent of the heterogeneity seen among tumors borne by HGSC patients (42,43).

Evaluating optimal combination treatment strategies in *BRCA1*-null HGSC ovarian tumors

We proceeded to evaluate the responses to certain commonly used targeted clinical therapies in the HR-deficient BPPNM and non-classified PPNM tumor models. Prexasertib and Olaparib combination proved synergistic *in vitro* for both the PPNM model (Bliss score =1.8) and the BPPNM model (Bliss score = 1.01) (Bliss scores greater than zero indicate synergy, **Figure 4A-B**). *In vivo*, the combination of Prexasertib and Olaparib treatment demonstrated survival benefits in the BPPNM tumor-bearing mice (**Figure 4C-D**, $p < 0.032$), and in the PPNM tumor-bearing mice (**Figure 4C and E**, $p < 0.0054$).

Next, we proceeded to determine whether the genotype-driven drug sensitivities of each model could be combined with immune-checkpoint blockade (ICB) therapy. We observed elevated levels of PD-L1 expression in BPPNM tumors (**Supplemental Figure 3D**), causing us to examine the impact of PD-L1 inhibition (44,45) in combination with Olaparib therapy (46,47). In the BPPNM tumors, a significant extension of long-term survival was achieved using Olaparib in combination with anti-PD-L1 treatment, with the vehicle-treated control group surviving a median of 56 days while 80% the combination-treated mice survived over 180 days. At that point, with no evidence of disease, the experiment was discontinued (**Figure 4C-D**, $p < 0.0018$). Such significant survival benefit was not observed in the PPNM tumor-bearing mice, which carry wild-type *Brca1* alleles, suggesting that *Brca1* deficiency is necessary for responses to PARP inhibitors applied in combination with an immune checkpoint blockade therapy. Based on these limited observations, we tentatively concluded that targeted therapy involving inhibition of the PARP pathway in combination with an immune checkpoint therapy in ovarian cancer offers the potential to tailor treatment for patients bearing *BRCA1*-defective HGSC tumors.

Growing evidence supports the important role of immune signatures associated with the HGSC tumor microenvironment as useful predictors of response to immunotherapies. To identify the tumor-associated immune signatures of *Brca1*-null BPPNM tumors (**Figure 4G**) and the *Brca1*-wild-type- harboring PPNM tumors (**Figure 4H**), we performed bulk tumor RNA-sequencing. Differential expression analysis revealed extensive gene expression differences between these tumors (**Figure 4F**). Thus, we performed gene set enrichment analysis (GSEA) and cross-referenced these data with results emerging from the use of the Gene Ontology Consortium (GO) and Hallmark analyses (48). We also interrogated these differentially expressed genes to identify pathways that might have contributed to the differences observed in the responses to

immunotherapies (**Figure 4F**). Consistent with previous studies of HR-deficient HGSC patient cohorts (41,49), IFN- γ , IFN- α and inflammatory signatures were most upregulated in *Brca1*-null BPPNM tumors in comparison to *Brca1*-wild-type PPNM tumors. These IFN signatures likely contribute to the enhanced responses to ICBs, as observed in HR- deficient human HGSCs (41,49). Hence, these models faithfully recapitulate these aspects of the human disease and may have broader implications for understanding the antitumor immune responses in *BRCA1*-null tumors.

***Ccne1*-overexpressing ovarian model is exquisitely sensitive to combinations of cell cycle checkpoint kinase and immune checkpoint inhibitors**

Studies combining genome-wide analysis and expression profiling in ovarian cancer patients have suggested that patients harboring *CCNE1* gene amplification driving over-expression of the encoded Cyclin E1 protein confront the worst overall survival (1,50). This indicates the unmet clinical need to identify and target pathways associated with *CCNE1*-overexpressing HGSC tumors. We designed our therapeutic strategy to sensitize the KPCA tumor model, the cells of which overexpress *Ccne1* based on their modestly effective single agent Prexasertib response (as seen in **Figure 2I**) and their immunosuppressive tumor microenvironment.

Initially, we chose to examine the impact of PD-L1 inhibition on reversing the observed T-cell dysfunction that could, we reasoned, have been caused by high levels of PD-L1 expression by the KPCA tumor cells (44,45) (**Supplemental Figure 3C and 3E**). We additionally investigated CTLA4 inhibition (51), which can inhibit Treg function (elevated in KPCA tumors) and can promote T-cell infiltration (low in KPCA tumors) (**Figure 3C-D**). Single-agent anti-PD-L1 or anti-CTLA4 and combination anti-PD-L1 and anti-CTLA4 treatments were modestly effective, resulting in 46 days ($p < 0.003$), 51 days ($p < 0.033$), and 63 days ($p < 0.033$) median survival respectively in comparison to 35 days median survival of vehicle treatment control group (**Figure 5A, B and D**).

We next evaluated the ability of Carboplatin or Prexasertib to sensitize the KPCA tumor model to these various checkpoint immunotherapies (52) (**Figure 5B and 5D**). The combination of Carboplatin plus anti-PD-L1 and anti-CTLA4 (termed here the CPC protocol) therapies conferred a significant 140% increase in median survival time over the vehicle treatment control group (repeated in three independent cohorts, $p < 0.0005$). However, no complete long-term responses were achieved (**Figure 5D**). Prexasertib administered together with both anti-PD-L1 and anti-

CTLA4 ICB in treating mice bearing KPCA tumors induced remarkable long-term tumor regression and overall survival benefit in the KPCA tumor model (**Figure 5B**). Remarkably, the application of this triple combination protocol (hereafter termed PPC) to the treatment of 12 mice bearing KPCA tumors resulted in a complete response in 10 mice (83% complete response rate, repeated in three independent cohorts, $p < 0.0001$). These responses were durable, being observed for 120 days after initiation of treatment. The depletion of CD8+ cytotoxic T-cells before treatment with this PPC therapy prevented complete responses, with only a small increase in median survival retained, highlighting the critical contribution of CD8+ T cells (**Figure 5F-G**).

We next interrogated the memory T-cell response in surviving tumor-free mice by re-challenging six mice with the same KPCA cell line (at least seven months post last therapy, N=6). All mice that had previously exhibited a complete response rejected the re-challenge (survival > 2.5 months), while all tumor-naïve mice succumbed to disease ($p < 0.0022$, **Supplemental Figure 5A**). Together, these data indicated that CHK1 inhibition by Prexasertib in the KPCA tumors was able to induce a strong response to dual ICB therapy that depended on CD8+ T-cells and was capable of producing long-term immunological memory to the KPCA tumors.

Spontaneous resistance to triple combination therapy in clones of the *Ccne1*-overexpressing ovarian model may be driven by Follistatin overexpression in cancer cells

Given the robust responses of KPCA tumors to the triple PPC therapy, we decided to evaluate its efficacy in a second independently derived FTE clone bearing the same introduced genetic lesions as the KPCA tumor cell line studied above; we termed this second line KPCA.C hereafter (**Figure 1B**). We confirmed the presence of genetic alterations in the KPCA.C cell line that replicated those present in the KPCA cells (**Supplemental Figure 5B-D**). We also compared the genetic similarity of KPCA.C cells to KPCA cells using whole-exome sequencing analysis (**Supplemental Figure 5E**) and assessed allelic imbalance profiles using shallow whole-genome sequencing (**Supplemental Figure 5F-G**). No apparent differences were observed in examining the genetic similarity of KPCA.C cells to KPCA cells. We also showed that KPCA.C cells exhibited a similar response to Prexasertib *in vitro* in terms of DNA damage induction and replication stress (30), as seen in the related KPCA cell line (**Supplemental Figure 5H**). Additionally, we confirmed the serous ovarian cancer histopathology features of KPCA.C-induced tumors (**Supplemental Figure 5I**).

However, while we observed significant responses of the KPCA tumors, both the Prexasertib plus anti-PD-L1 and anti-CTLA4 blockade therapies (PPC therapy) (**Figure 5C**) and Carboplatin plus anti-PD-L1 and anti-CTLA4 (CPC) (**Figure 5E**) treatment of the closely related KPCA.C tumors yielded only very modest therapeutic responses. The median survival of PPC (26 days, $p < 0.0001$) and CPC (28 days, $p < 0.001$) extended median survival over vehicle control (21 days) only incrementally (results of 3 independent experiments).

The depletion of CD8⁺ T-cells before PPC therapy of the KPCA.C cells eliminated even the modest increase in survival produced by PPC (**Figure 5H**), suggesting that even this modest response depended on CD8⁺ T-cells. Collectively, all mice treated with PPC showed a modest antitumor response and were sacrificed due to excessive tumor burden. Thus, the KPCA.C tumors, in contrast to the closely related KPCA, were largely resistant to combination Prexasertib plus anti-PD-L1 and anti-CTLA4 blockade therapies (**Figure 5C and E**).

We then sought to identify the factors driving the differential responses of the KPCA and KPCA.C populations to PPC therapy. Multi-parameter flow cytometry monitoring immune cells revealed modest differences in tumors seeded by each clone (**Supplemental Figure 6A-D**). Thus, the KPCA.C tumors were associated with a higher proportion of immunosuppressive T-regs in both the omental tumors (3.2-fold more, $p < 0.04$) as well as in the ascites (3-fold more, $p < 0.02$) relative to the KPCA tumors (**Supplemental Figure 6A-B**). The KPCA tumors were infiltrated with more Ly6G^{high}/Ly6C^{low} granulocytes (2.4-fold higher, $p < 0.03$) in comparison to KPCA.C tumors (**Supplemental Figure 6A**). The ascites of the KPCA tumor-bearing mice contained far more CD8⁺ T-cells (3.8-fold more $p < 0.02$) relative to the ascites generated by the KPCA.C tumors. In contrast, the KPCA omental tumors had higher levels of exhausted TIGIT- and TIM-3-positive CD8⁺ T cells relative to KPCA.C tumors (1.5-fold more, $p < 0.035$, **Supplemental Figure 6C-D**). These observations suggest complex differences between the immune microenvironments of KPCA versus KPCA.C tumors.

The differences in immune populations in the tumors generated by each clonal population were also assessed following treatment with PPC. Thus, omental tumors were harvested and weighed midway through the typical treatment regimen with PPC before undergoing flow cytometry analysis (**Figure 5I-K** and **Supplemental Figure 6E-F**). In consonance with the survival data, tumor weight decreased after treatment with PPC for the KPCA clone, but not for KPCA.C when relative to untreated control (**Supplemental Figure 6F**). PPC treatment drove an influx of immune

cells into both the KPCA and the KPCA.C tumors; however, the KPCA tumors were infiltrated by more immunocytes with smaller proportions of immunosuppressive cells (**Figure 5I-K**).

Given the lack of apparent differences in the genomes between the KPCA and KPCA.C cell lines based on the whole-exome and shallow whole-genome sequencing analysis (**Supplemental Figure 5F-H**), we hypothesized that differences in gene expression might drive the differential response seen in the KPCA (exceptional responders) and KPCA.C tumors (partial-responders). To test this notion, we performed bulk RNA-seq on both types of tumors. Bulk RNA-seq of tumors derived from each clone revealed extensive gene expression differences. We interrogated these differentially expressed genes to identify pathways that might have contributed to the treatment resistance of the KPCA.C tumors (**Figure 6A**). Furthermore, we performed scRNA sequencing to compare cell types and cell states between KPCA and KPCA.C, doing so to identify potential differences underlying the more immunosuppressive omental tumor microenvironment of the KPCA.C tumors (**Figure 6B**, **Supplemental Figure 7A** and **Supplemental Table 3, 5-6**).

We initially focused our attention on gene expression differences between KPCA and KPCA.C associated with the cancer cell cluster identified in the bulk RNA-seq dataset (**Figure 6C**). More specifically, we identified as high-priority candidates, genes that were significantly overexpressed in the therapy-resistant KPCA.C tumors relative to the exceptional responders in the KPCA-bearing cohort. We also validated the overexpression of these genes in the cancer cell lines *in vitro*. To further restrict our candidate list to potentially actionable immunotherapeutic targets, we performed gene set enrichment analysis (GSEA) and cross-referenced these data to results emerging from the use of the Gene Ontology Consortium (GO) and Hallmark analyses (48) to identify immune-modulating secreted factors.

Using the above analytical methods, we prioritized the following candidate three gene targets: *Fst*, *S100a4*, and *Il33* (**Figure 6D** and **Supplemental Figure 7B-C**). When comparing cell culture supernatants of the KPCA.C cell lines relative to those of their KPCA counterparts, we confirmed the elevated expression of follistatin (FST) (**Figure 6E**) by ELISA. The KPCA.C cells exhibited a 7.5-fold elevated expression of FST compared to KPCA cells (**Figure 6E**). We then tested the hypothesis that KPCA but not KPCA.C could further upregulate FST expression in response to transforming growth factor (TGF β), a potent inducer of this pathway (53,54). Strikingly, following TGF β stimulation, KPCA.C cells exhibited a 32-fold greater elevation of expression of FST compared to KPCA by ELISA (**Figure 6E**). Furthermore, when comparing lysates of the KPCA.C

cell lines relative to those of their KPCA counterparts, we found elevated expression of S100A4 and IL33 using western blot analysis (*data not shown*). To examine the possible functions of S100A4 and IL33 in the observed differences in therapeutic responses, we generated knockouts of the *S100a4* and *Il33* gene in the genome of cells of the KPCA.C line using the CRISPR/Cas9 approach. Here, we observed only modest differences in survival with Prexasertib plus anti-PD-L1 and anti-CTLA4 (PPC) blockade therapies when comparing the survival of the *S100a4*- or *Il33*-knockout (KO) tumors relative to their matched controls (**Supplemental Figure 7D-E**).

We then focused our analyses on the third gene of possible interest, which encodes follistatin (*Fst*), an autocrine glycoprotein that primarily binds and bio neutralizes members of the TGF- β superfamily (55). Follistatin has been used clinically as a marker for shorter overall survival of ovarian cancer patients (56). FST is an inhibitor of activin and is involved in the regulation of myeloid (57), dendritic, and T-cell functions (58). We confirmed the elevated expression of FST in KPCA.C tumors in comparison to KPCA in the omental tumors using RNA in situ (RNA-scope) methodology (59) (**Figure 6F**).

To uncover the possible functional contributions of *Fst* to the observed therapeutic responses, we generated a knockout of the *Fst* gene in the genome of the KPCA.C cells using the CRISPR/Cas9 approach. We confirmed the loss of its encoded product by ELISA of medium supernatants generated by the knockout cells (**Figure 6E**). We then treated mice bearing KPCA.C *Fst* KO tumors with the triple Prexasertib plus anti-PD-L1 and anti-CTLA4 (PPC) blockade therapy protocol (see treatment regime in **Figure 6G**) and compared the overall survival to untreated-matched controls. We also measured omental tumor weights at the mid-point timepoint of the treatment and compared them to the untreated cohorts. (**Figure 6H**, repeated in two independent cohorts). In the *Fst* KO cells (*sgFst* pool) untreated cohort, we observed a median survival of 28.5 days ($p < 0.0001$) (**Figure 6I**) in comparison to a median survival of 21 days in parental untreated KPCA.C tumor-bearing mice. Remarkably, tumor regression and highly significant overall survival benefit were observed in the triple combination of Prexasertib plus anti-PD-L1 and anti-CTLA4 blockade therapies in the *Fst* KO tumors (*sgFst* pool). Of the nine KPCA.C *Fst* KO tumor-bearing mice treated with the triple combination, six mice exhibited a complete response observed for 48 days following treatment ($p < 0.0001$, **Figure 6I**, repeated in two independent cohorts). This contrasts with the behavior of KPCA.C tumor-bearing mice, which were largely resistant to triple Prexasertib plus anti-PD-L1 and anti-CTLA4 blockade therapy.

Given the robust responses of *Fst* KO KPCA.C tumors to the triple PPC therapy, we decided to evaluate its efficacy in yet another independently derived FTE clone bearing the same introduced genetic lesions as the KPCA and KPCA.C tumor cell line; we termed this cell line KPCA.A hereafter. We confirmed the presence of genetic alterations (**Supplemental Figure 5B-D**), compared the genetic similarity of KPCA.A cells to KPCA cells using whole-exome sequencing analysis (**Supplemental Figure 5E**) and whole-genome sequencing (**Supplemental Figure 5F-G**). In the whole-exome sequencing analysis, we observed some differences at the single-nucleotide level between KPCA.A versus KPCA cells (denoted in blue, **Supplemental Figure 5E, Supplemental Table 6**). Besides, we showed that KPCA.A cells exhibited a response to Prexasertib *in vitro* in terms of DNA damage induction and replication stress (30), similar to that seen in the related KPCA cell line (**Supplemental Figure 5H**). Additionally, we confirmed the serous ovarian cancer histopathology features of KPCA.A-induced tumors (**Supplemental Figure 5I**).

Similar to our approach described earlier, we confirmed the elevated expression of FST by ELISA (**Figure 6J**) and *in situ* (RNA-scope) methodology (**Figure 6J** inset). Similar to our approach with the KPCA.C cells, we generated a knockout of the *Fst* gene in the genome of the KPCA.A cells using the CRISPR/Cas9 approach and confirmed the loss of its encoded product by ELISA (**Figure 6J**). We then treated mice bearing KPCA. A *Fst* KO tumors with the triple Prexasertib plus anti-PD-L1 and anti-CTLA4 (PPC) blockade therapy protocol (see treatment regime in **Figure 6K**) and compared the overall survival to untreated-matched controls. We measured omental tumor weights at the mid-point timepoint of the treatment and compared them to the untreated cohorts. (**Figure 6L**, repeated in two independent cohorts). Remarkably, tumor regression and highly significant overall survival benefit were observed in the triple combination of Prexasertib plus anti-PD-L1 and anti-CTLA4 blockade therapies in the *Fst* KO tumors (*sgFst* pool). Of the ten *Fst* knockout KPCA.A tumor-bearing mice treated with the triple combination, seven mice exhibited a complete response and remarkable long-term survival for over 130 days following treatment ($p < 0.0001$, **Figure 6M**, repeated in two independent cohorts). We concluded that FST functioned as a potent driver of the observed resistance to the triple Prexasertib plus anti-PD-L1 and anti-CTLA4 (PPC) treatment protocol of KPCA.C and KPCA.A tumors.

To further unravel the molecular basis of *Fst* overexpression in the Prexasertib plus anti-PD-L1 and anti-CTLA4 therapy-resistant KPCA.C and KPCA.A clones, we assessed copy number changes at the *Fst* loci using shallow whole-genome analysis (**Supplemental Figure 7F**). We did

not observe an amplification in the KPCA.C and KPCA.A model or deletions KPCA models in the *Fst* locus. Given the lack of apparent genetic differences at the *Fst* locus among the three cell lines, i.e., KPCA, KPCA.A and KPCA.C), we hypothesized that the differential response seen in the KPCA (exceptional responders) and KPCA.C and KPCA.A tumors (partial-responders) might be driven by an epigenetic mechanism. To explore this possibility, we analyzed chromatin accessibility by ATAC-seq in KPCA, KPCA.C, and KPCA.A models at the *Fst* locus (**Figure 7A**). We observed evidence of epigenetic regulation of *Fst* regulatory elements concordant with the expression data (**Figure 7B**).

The observations suggested that FST expression can serve as a predictive biomarker for both ICB and Prexasertib combination treatment response; accordingly, we assessed the effects of *Fst* overexpression (OE) in the PPC treatment responsive KPCA model. For this purpose, we overexpressed *Fst* in KPCA cell lines by lentiviral vector transduction and confirmed the elevated Follistatin levels of the cell culture supernatants by ELISA (**Figure 7C**). We then treated KPCA *Fst* OE tumor-bearing mice with the combination treatment of Prexasertib plus anti-PD-L1 and anti-CTLA4 (**Figure 7D**). Indeed, forced *Fst* overexpression reversed the PPC treatment sensitivity of the KPCA tumors (**Figure 7D**). Median survival was significantly reduced to 50 days in PPC treated KPCA *Fst* OE tumor-bearing mice, compared to up to more than 120 days long-term overall survival in KPCA models undergoing the same combination treatment, $p < 0.0001$ (**Figure 7D**, repeated in three independent cohorts). We concluded that elevated levels of follistatin are sufficient, on their own, to induce resistance to the combination treatment of Prexasertib plus anti-PD-L1 and anti-CTLA4 in previously sensitive-KPCA models.

Furthermore, differential expression analysis between KPCA *Fst* OE and KPCA tumors revealed extensive gene expression differences between these tumors (**Figure 7E**) that might have broader utility in mounting an antitumor immune response. Collectively, the *Ccne1*-overexpressing-models KPCA and KPCA.C (**Figure 7F-G**) and KPCA.A uncovered that inhibition of CHK1 potentiates immune checkpoint response in a follistatin-dependent manner.

Given that high FST expression could be found to drive treatment resistance in the *Ccne1*-amplified mouse model, we next examined whether FST expression could predict progression-free survival for platinum-based chemotherapy in human HGSCs using the TCGA dataset (1). Intriguingly, high FST expression significantly predicted shorter progression-free survival (PFS) selectively in patients with *CCNE1*-amplified HGSCs (**Figure 7H**; $p = 0.0009$, Log-rank test), but

not among the patients with *BRCA1/2* deficient tumors (**Figure 7I**). High FST expression significantly predicted shorter PFS in the *CCNE1*-amplified tumor cohort as a continuous variable (HR; Hazard Ratio 19.7, 95%CI 3.8 – 109.9, $p=0.0003$), and also independently after adjusting for tumor stage and patient age at diagnosis (HR 24.4, 95%CI 4.8 – 133.6, $p=0.0001$). The overall survival showed a similar trend (**Supplementary Figure 7G-H**). These data provide a strong indication that FST overexpression, which is common in HGSCs and is clinically associated with shorter overall survival, may limit clinical responses of HGSC tumors to checkpoint blockade immunotherapy and may, therefore, represent an important target of inhibition undertaken to potentiate the clinical utility of immune checkpoint blockade therapies of ovarian cancer patients.

Discussion

The currently available therapies applied to the treatment of ovarian carcinomas are limited in their efficacy, in part because these tumors constitute a heterogeneous disease with a number of distinct mutant genotypes that exert varied, poorly understood effects on the tumor phenotype, including its microenvironment and drug response. This heterogeneity has been particularly challenging when evaluating new immunotherapies, given our lack of understanding of how cancer genotypes drive both immunophenotypes and therapeutic responses.

In this study, we generated a series of genetically defined mouse HGSC cells lines that (i) were derived from fallopian tube epithelial (FTE) cells—the presumed normal cells-of-origin of HGSCs (17-19); (ii) carry constellations of mutant alleles present in human HGSC genomes, and (iii) form tumors in syngeneic immunocompetent C57BL/6 mice. Our central goal in this effort was to determine how alternative genotypes of HGSCs growing in syngeneic hosts govern the composition of tumor-associated immune microenvironments and modulate the responsiveness to currently available immunotherapies. With these models in hand, we hope to enable future studies by ourselves and others focused on determining the influence of various genomic states on the tumor microenvironment, clinical progression, and treatment responses.

The strength of our models is that the mutations employed capture some of the most prominent pathways dysregulated in homologous recombination-deficient and -proficient HGSC patient samples. These genetically defined, engineered m-FTE cell lines recapitulated the histology and clinical behavior of human HGSCs in their spread through the peritoneal cavity, their preferential adhesion to intra-peritoneal sites including the omentum, and their responsiveness to both DNA-damaging agents and PARP inhibitors. The clinical fidelity of these murine models was further

supported by the increased responses to platinum-based reagents (Carboplatin and Cisplatin), as well as PARP inhibitors (Olaparib and Niraparib), in the *Brca1* mutant, HR-deficient cell line. By contrast, the DNA-damaging therapies afforded little improvements in the overall survival of HR-proficient HGSC genotypes, reflecting the poor treatment responses also observed in the clinical setting. Notably, preclinical models recapitulating the complex biology of *CCNE1*-driven HGSC tumors have not been available until now, highlighting the potential of the presently described models to answer a clinically unmet need for improved therapeutic options for patients with HR-proficient HGSCs.

We initiated studies to explore the dynamic interplay between various genetically defined tumor models and the corresponding tumor-associated immune microenvironments that they recruit. In our hands, the comprehensive analyses of the omental tumor microenvironments revealed distinct immune landscapes associated with different tumor genotypes. Somewhat unsurprisingly, the tumors with deficient HR DNA repair (BPPNM) were most heavily infiltrated with immune cells, suggesting a more immunogenic phenotype. These tumors carried the highest proportions of CD3e-positive T-cells, highly exhausted CD8 T-cells, M2-like macrophages, and the lowest proportion of Tregs. These differences correlated with elevated levels of cytokines known to drive T-cell suppression and myeloid cell infiltration, including MIP-3 β , TGF β 1, and TGF β 2 (60-62). Notably, the immunological signatures detected in human tumors (41,49) resembled the cytokine and gene expression profiles of the genetically defined HR-deficient mouse models described here.

Heavily inflamed tumors of other tumor types expressing high PD-L1 levels are often considered as useful predictive indicators of successful ICB therapies in the clinic (63). However, BPPNM tumors were unresponsive to single-agent PD-L1 and only produced long-term survival when ICB was combined with Olaparib, reflecting reported clinical data (46,49,63). These data suggest that PD-L1 expression and inflammatory status alone may not be sufficient on their own predict the success of ICB in these tumors and that immune-stimulating alterations to the tumor microenvironment incurred by adjuvant treatments such as chemotherapy may be necessary for a significant response to checkpoint inhibitors (43,64). Nonetheless, more generally, targeted therapy based on inhibiting the DNA damage response pathway in combination with ICB therapy in ovarian cancer offers the potential to tailor treatment for patients with *BRCA1* mutant HGSC.

The HR-Proficient KPCA tumors displayed a more immunosuppressive microenvironment than that assembled by the BPPNM tumors and exhibited an entirely different response to immunotherapeutic combinations. The KPCA tumors, which showed high PD-L1 expression, were poorly infiltrated with T-cells and had higher proportions of exhausted CD8 cells co-expressing PD-1, TIGIT, and TIM-3, comprising 31% of all CD8+ cells— a value nearly 10-fold higher than that of BPPNM tumors. The KPCA tumors were also infiltrated with higher proportions of immunosuppressive cells, including Tregs, Ly6G+Ly6C+ myeloid cells, and Ly6G^{low}/Ly6C^{high} granulocytic myeloid cells (38). The ascites of KPCA tumor-bearing mice also contained elevated levels of many cytokines known to be immunosuppressive, such as TGF β and IL-10 (40,62,65-67). Single and double combinations of anti-CTLA4, anti-PD-L1, Carboplatin, Olaparib, and Prexasertib were all mostly ineffective in treating these tumors. However, a triple combination of anti-CTLA4, anti-PD-L1, and Prexasertib showed remarkable benefits, including complete responses that were dependent on the presence of cytotoxic CD8+ T-cells. Collectively, these data may presage a use for CHK1 inhibition by Prexasertib to potentiate ICB efficacy in *CCNE1*-amplified HGSCs.

The behavior of the KPCA.C and KCPA.A variant clones, which were relatively resistant to the same triple-combination therapy involving Prexasertib plus anti-PD-L1 and anti-CTLA4 that eliminated the related KPCA tumors, was unanticipated, if only because they ostensibly carry the same genetic alterations as KPCA cells. A comparison of gene expression between these differentially responding variant clones identified *Fst* as a potential determinant of resistance that was further pursued, leading eventually to the identification of *Fst* as an important determinant of responsiveness to the triple therapy described here. Furthermore, to understand the molecular basis of *Fst* overexpression in the PPC treatment, resistant KPCA.C, and KCPA.A cells, we investigated epigenetic differences between these cells and compared them to PPC treatment sensitive KPCA cell line. We identified putative *Fst* regulatory elements using ATAC-seq that might underlie its overexpression. Rigorous overexpression studies confirmed *Fst* is an important determinant of therapeutic response.

The precise mechanisms of action of *Fst* and its contribution to the immunosuppressive microenvironment of KPCA.C tumors are unclear at present. FST is a secreted inhibitor of activin, a TGF β family ligand previously linked to shorter overall survival in ovarian cancer (56,68). FST can also bind and regulate other TGF β family ligands such as myostatin, and BMPs, albeit with lower affinity (54,69). Knocking out follistatin expression in the previously resistant KPCA.C and

KPCA. A tumor cells restored much of the efficacy of the triple combination, with a majority of tumor-bearing hosts showing a complete response. Given the reported function of activin in regulating myeloid cells, which are abundant in these tumors (57,58), it is tempting to speculate that FST secretion by cancer cells might block an essential signal required to coordinate innate and adaptive immune response against the tumor. These data suggest FST could represent a novel predictive biomarker of sensitivity to ICB blockade and a therapeutic target whose inhibition could sensitize HGSC to immunotherapy (70,71).

In conclusion, our study highlights the unrealized potential of tumor genotype-driven strategies for optimizing the designing of protocols employing combination checkpoint immunotherapy. The present proof-of-concept studies validate the use of novel syngeneic preclinical immunocompetent mouse models as experimental systems to explore tumor heterogeneity and treatment modalities of HGSCs.

Materials and Methods

Cell Lines and Cell Culture

Fallopian tube cells were isolated from $p53^{flox/flox}$ (Jackson laboratory) and $Brca1^{flox/flox}p53^{flox/flox}$ (20) C57BL/6 mice female mice. The from $p53^{flox/flox}$ and $Brca1^{flox/flox}p53^{flox/flox}$ fallopian tube organoids were generated as described in (72). To deplete $p53$ and $Brca1$, $p53^{flox/flox}$ and $Brca1^{flox/flox}p53^{flox/flox}$ fallopian tube organoids were dissociated into single cells and then infected with 10^5 pfu Adenovirus-CMV-Cre (Vector Development Lab, Baylor College of Medicine) and confirmed as previously described (73). The $p53^{-/-}$ and $p53^{-/-}Brca1^{-/-}$ fallopian tube cells were released from the Matrigel, and single-cell sorted to introduce genetic alterations by using lentiviral gene transduction (for mutations and over-expression) and CRISPR/Cas9 (for deletions) methodology as described in Figure 1A-B. All cell lines were cultured in fallopian tube cells media (FT-media); DME media supplemented with 1% Insulin-Transferrin-Selenium (Thermo Fisher Scientific; ITS-G, 41400045), 100 μ l EGF (10ug/ml), 4% heat-inactivated fetal bovine serum (Thermo Fisher Scientific; IFS, F4135) and 1% penicillin and streptomycin. All cultures were checked for mycoplasma using MycoAlert Plus Mycoplasma Detection Kits assay (Lonza LT07).

Site-specific point mutation using NEB Q5 *Site-Directed* Mutagenesis Kit was used on mouse $p53$ plasmid (Addgene plasmid #22725) to generate mouse $p53^{R172H}$ expressing plasmid. Subsequently, mutant mouse $p53^{R172H}$ was cloned into pLV-EF1a-IRES-Hygro (Addgene plasmid #85134). Mouse *Ccne1* (Sino biological, MG50896-ACG) was cloned into pLV-EF1a-IRES-Neo (Addgene plasmid #85139). Mouse *Akt2* (Addgene plasmid #64832) was cloned into pLV-EF1a-IRES-Blast (Addgene plasmid #85133). For *Myc* overexpression, we used MSCV-Myc-PGK-Puro-IRES-GFP (Addgene plasmid #75124), and for *Kras*^{G12V}, we used pUG2K (Addgene plasmid #35493). The lentiviral vector used to overexpress *Brd4-short isoform*, *Smarca4* and Follistatin (*Fst*) in our study, pLV[Exp]-EF1A>mBrd4[NM_198094.2](ns):P2A:EGF and pLV[Exp]-EF1A>mSmarca4 [NM_001357764.1] (ns):P2A:EGFP and pLV[Exp]-mCherry-EF1A>mFst[NM_001301373.1] (VB200220-1171ukt) overexpression plasmids were used that were constructed by VectorBuilder. The vector ID is VB191212-2643ptd, VB191205-1922bak, and VB200220-1171ukt, which can be used to retrieve detailed information about the vector on www.vectorbuilder.com. Lentivirus-based constructs were packaged with the pMD2.G (VSVG) (Addgene plasmid #12259) and psPAX2 plasmids (Addgene plasmid #12260). Retrovirus-based constructs were packaged with the pUMVC (Addgene plasmid #8449) and pMD2.G (VSVG)

(Addgene plasmid #12259). Viral infections were performed using 10 µg/mL polybrene transfection reagent (Thermo Fisher Scientific; TR1003G) for 8 hours. After viral transduction selection was performed, using Hygromycin B (Life Technologies 10687010), neomycin-Geneticin Selective Antibiotic (G418 Sulfate), Powder (Life Technologies 11811031), and Blasticidin S HCl (Life Technologies R21001). Genetic alterations by using lentiviral gene transduction (for mutations and over-expression) and CRISPR/Cas9 (for deletions) were confirmed by PCR-based analysis and immunoblotting. For PCR-based verification of *KrasG12V*, mutant *p53* (R172H), and *Brca1*, the primers are listed in the table below. Briefly, the genomic DNA was extracted from cells using the Purelink Genomic DNA Mini kit (Life Technologies, K182001), following the manufacturer's instructions. Subsequently, 2X Q5 High-Fidelity Polymerase (New England Biolabs, M0494L) in Nuclease-free (Life Technologies, AM9937) was used to amplify the locus of interest using the manufacturer's instructions. PCR products were separated on 1% agarose gel; see Supplementary Method Table 1-Primer sequences for PCR. For induction of p21 in a p53-dependent manner, we treated the m-FTE cell lines and MEF's (ATCC SCRC-1040) with or without Nocodazole (0.125 µg/ml (74); Selleckchem, S2775) for 24 hrs.

CRISPR/Cas9 targeting and confirmation using Sanger Sequencing of Modified Loci

Murine CRISPR/Cas9-GFP expressing knock-out plasmids were obtained from Santa Cruz Biotechnology. For *Pten* (SC-422475), *Nf1* (SC-421861), *S100a4* (SC-422782), *Fst* (SC- 420417) and *I/33* (SC- 429508). Briefly, 0.5x10⁶ cells/well were seeded into a 6-well tissue culture plate and incubated overnight. CRISPR/Cas9 Knock-out plasmids were transfected according to the manufacturer's instructions. For isolation Cas9-GFP-expressing cell populations, cells were sorted by flow cytometry (sorted for GFP positive cells) and seeded as single cells into 96-well flat-bottom plates (Westnet Inc., 3595). The sgRNA sequences are listed in the Supplementary Method Table 2.

Confirmation of clonal expanded CRISPR/Cas9 knock-out cell lines was performed by Sanger DNA sequencing. Genomic DNA was extracted from cells using the Purelink Genomic DNA Mini kit (Life Technologies, K182001), following the manufacturer's instructions. Next, the deleted DNA regions were PCR amplified. The respective locus (<1000 ng) was amplified using primers (0.5 µM) spanning potential sites of deletion with 2X Q5 High-Fidelity Polymerase (New England Biolabs, M0494L) in Nuclease-free (Life Technologies, AM9937), following the manufacturer's instructions. PCR products were separated on 1% agarose gel. DNA fragments were excised

from the agarose gel, and DNA was gel purified using Zymoclean Gel DNA Recovery Kit (Zymo Research, 77001-146), following the manufacturer's instructions. Next, PCR products of the *PTEN* and *NF1* genomic regions were cloned using CloneJET PCR Cloning Kit (Life Technologies, K123240). Transformation products were spread on LB Agar Carbenicillin plates and incubated overnight at 37°C. Colonies were sequenced, and data was analyzed using SnapGene 5.1 (BioTech), in which reads were mapped to the reference sequences. See Supplementary Method Table 2. CRISPR/Cas9 Plasmids and sgRNA sequences for CRISPR/Cas9 targeting and confirmation using Sanger Sequencing of Modified Loc

Animal experiments

For animal studies, C57BL/6 mice (Jackson Laboratory, stock no. 000664). Before injection, three million cells were suspended in Matrigel (Corning Matrigel matrix, 47743-710): FT-media (1:1). The cell mix with Matrigel was administered intraperitoneally into 8-12-week-old female mice. Tumor burden was monitored using 2D *in vivo* imaging system (IVIS) bioluminescence imaging. Briefly, the mice were injected with 150 mg/kg D-luciferin Firefly (PerkinElmer, 122799), and luminescence was assessed 15 mins later by using the Xenogen IVIS-100 Imaging System. Images were analyzed with Living Image Software 4.7.3. As per the indicated treatment strategy, mice were injected intraperitoneal with the indicated doses. Carboplatin (Patterson Veterinary Supply, 07-890-7778) (dose-30 mgs/kg), Olaparib (Selleckchem, S1060) (dose- 50mgs/kg) (75) and Prexasertib (Selleckchem, S7178) (dose-10mgs/kg) were used. Olaparib and Prexasertib were resuspended for *in vivo* injections according to the manufacturers' instructions. For immunotherapy, anti-CTLA4 (dose-50 µg, Bioxcell, BE0131) and anti-PDL1 (dose-50 µg, Bioxcell, BE0101) were used respectively. Treatments were repeated twice a week for a total of four weeks. Control mice were injected with either saline or 4% DMSO or isotype control antibody. *In vivo* depletion of CD8 T-cells was achieved by intraperitoneal injection of 200 µg per mouse YST-169.4 (anti-CD8) monoclonal antibody (BioXcell, West Lebanon). The treatment regimen is illustrated in Figure 5G, one weekly dose was administered intraperitoneally for four weeks, and mice were monitored for survival. T-cell depletion experiment was repeated independently two times with 3-4 mice per group. For the re-challenge experiment, one million/mouse KPCA cells were injected intraperitoneally, as described earlier. The MIT Committee on Animal Care approved all animal study protocols. All cell lines were murine pathogen tested and confirmed mycoplasma negative by using MycoAlert Plus Mycoplasma Detection Kits assay (Lonza LT07).

Western Blot

For protein isolation, cells were washed twice with ice-cold cold PBS– and placed on ice. Cells were lysed with the RIPA Buffer (Sigma Aldrich, R0278) supplemented with protease inhibitor (Sigma Aldrich, 11873580001) and phosphatase inhibitor (Roche Diagnostics, 4906845001) on ice then flash frozen on dry ice. Before analysis, lysates were spun down at 15,000 g for 15 minutes at 4°C, and the supernatants were used for all subsequent procedures. Proteins with low concentration were filtered by Amicon Ultra-0.5ml centrifugal filters (Millipore, UFC500396). The protein concentration was analyzed by the DC Protein Assay Kit (Bio-Rad, DC Protein Assay Kit II, 5000112) according to the manufacturer's instructions. 25 µg of cell lysate was loaded to NuPAGE Novex 4-12% Bis-Tris gels (Thermo Fisher Scientific) and then transferred to nitrocellulose membrane (Thermo Fisher Scientific) by electroblotting following the manufacturers' recommendations. Membranes were blocked using 5% non-fat milk in 1X Tris-buffered Saline, 0.1% Tween 20 (TBST) for 1 hour, and subsequently washed two times in 0.1% TBST. Primary antibodies dilutions were used as mentioned in the antibodies table below and incubated overnight at 4°C. Blots were washed, and the secondary antibody was used at 1:2000 dilution. Antigen detection was done by luminol-based enhanced using Western Lightning Plus-ECL, Enhanced Chemiluminescence Substrate (Perkin Elmer, NEL104001EA), and exposed to X-ray film (Thermo Fisher Scientific, PI34091). See Supplementary Method Table 3 for antibodies used.

Immunofluorescence

Engineered m-FTE cells (0.03×10^6 cells/well) were seeded to Nunc Lab-Tek II CC2 8-well Chamber Slides (Life Technologies, 154941). After 24 hours, cells were fixed with 4% PFA (Life technologies, 28906) for 10 min and then permeabilized with 0.2% Triton X-100 in PBS for 5 min. Blocking was done with 5% bovine serum albumin (Sigma, A2153) in PBS for 1 hour, and then cells were incubated with various primary antibodies (see antibodies table below) for 1.5 hours at room temperature. After that, secondary antibodies (1:500; Biotum) were used according to the primary antibody species. The cells were incubated with secondary antibody diluted in blocking buffer for 1 hour and washed with PBS. For nuclear staining, cells were incubated with DAPI (1:1000; Life Technologies, 62248) for 5 min. The cells were washed two times with PBS and mounted with Prolong Gold antifade reagent (Life Technologies, P36930). Slides were covered and stored in the dark at 4°C. Subsequently, images were acquired at 63x magnification by using a Zeiss inverted microscope. Zen Lite Digital Imaging (AxioVision, Zeiss) software platform was used for the image processing and analyses. See Supplementary Method Table 3 for antibodies used.

IR induced RAD51 foci

Engineered m-FTE cells were irradiated with a 10Gy dose of IR and then fixed 6hrs post IR. Cells were washed with CSK buffer (100mM NaCl, 300mM sucrose, 10mM PIPES pH 7.0, 3mM MgCl₂) and permeabilized with 0.2% Triton X-100 in CSK buffer for 2.5 min. Cells were washed in PBS and then fixed cells with 4% PFA; washed twice with PBS and blocked with 5% BSA in PBS for 15 min at room temperature. Cells were incubated with primary antibody RAD51 (Santa Cruz; SC-8349; 1:150), and g-H2AX (Millipore; 05-636; 1:5000) in 5% BSA for 35min at 37°C followed by incubation of secondary antibodies in 1% PBS for 25min at 37°C. Cells were mounted with DAPI, and images were acquired with an AxioCam 506 camera, controlled by Zen software. The RAD51 foci were quantified with CellProfiler image analysis software.

Cell Cytotoxicity Assay

In vitro cell cytotoxicity assays were performed with CellTiter-Glo Luminescent Cell Viability Assay (Promega), according to manufacturer's instructions. Cells were seeded to opaque-walled black clear-bottom 96-well plates (Thermo Fisher Scientific) and incubated overnight. The next day, indicated concentrations the drugs being tested were added Carboplatin (Patterson Veterinary Supply, 07-890-7778), Cisplatin (Patterson Veterinary Supply, 07-893-4099), Prexasertib (Selleckchem, S71178), Olaparib (Selleckchem, S1060), Niraparib (Selleckchem, S7625), OTX015 (MK 8628/ Birabresib) (Selleckchem, S7360), CPI-203 (Selleckchem, S7304), (+)-JQ1, BET bromodomain inhibitor (Abcam, ab146612) for 72 hours. For synergy analysis of Prexasertib and Olaparib treatment (Figure 4A-B), cells were plated as above, and the Bliss synergy score was calculated using SynergyFinder: a web application for analyzing drug combination dose-response matrix data (76). Luminescent Cell Viability Assay using CellTiter-Glo (Promega, G7571) was performed as per manufacturer's instructions. IC₅₀ values were determined using Graphpad Prism 8 (see Supplemental Table 1).

Immunohistochemistry

Omental tumor tissues were fixed with 10% Neutral buffered formalin (Sigma Aldrich, HT501128) overnight. The fixed samples were passed through the alcohol series, cleared with xylene, and embedded in paraffin blocks. Subsequently, 5- μ m-thick sections were cut from the paraffin-embedded blocks. For immunohistochemistry analyses, firstly, slides were dewaxed at 60°C for 20 min and rehydrated with following graded ethanol washing steps. After antigen retrieval (with either citrate buffer or HIER buffer according to the antibody) in a pressure cooker, blocking was done with PBS with 0.3% TritonX-100 + 1% donkey serum for 20 min. After blocking, sections

were incubated with various antibodies overnight at 4°C. The next day, slides were washed with PBS, and VECTASTAIN Elite ABC Kits (Vector Laboratories) were used for secondary antibody according to the manufacturers' instructions. Staining was developed with the IMMUPACT DAB HRP substrate kit (Vector Laboratories, SK-4105), and counterstaining was done with hematoxylin. Slides were mounted, and whole-slide scanned (20X magnification) at the Histology Core Facility, Koch Institute for Integrative Cancer Research at MIT, see Supplementary Method Table 3 for the antibodies used.

Tissue Processing

Omental tumors were collected and digested with collagenase (Sigma Aldrich, 11088793001), hyaluronidase (Sigma Aldrich, H3506), and DNAase (Sigma Aldrich) at 37°C for 45 min. The single-cell suspension was obtained by passage through a 70 µm filter (Westnet Inc., 35235) and with several washing steps with PBS. Pellet was resuspended with ACK lysis buffer (Life Technologies, A1049201) to lyse red blood cells at room temperature for 10 min and washed with PBS. Ascites were harvested, spun down at 1000 g for 10 minutes at 4°C, and the supernatants were stored for cytokine analysis. The pellet was lysed with ACK lysis buffer to lyse red blood cells at room temperature for 10 min and washed with PBS. After obtaining single-cell suspensions, cells were counted and then used for sc RNA-sequencing and multi-parameter flow cytometry analyses. For sc RNA seq, whole omental tumors (pooled four omental tumors/genotype) at the terminal time point of tumor growth from mice implanted with either the BPPNM, PPNM, KPCA, or KPCA.C cells for analysis.

Single-cell RNA sequencing

Cell Ranger (version 3.0.2) using standard parameter was used, and samples were aligned against the refdata-cell ranger-mm10-1.2.0 reference sequences. For details about the samples, please see (Supplemental Table 3). Samples were analyzed using Seurat 3.1.0. Samples were filtered for mitochondrial percentage <20% and merged based on the Seurat "Integration and Label Transfer" vignette using 3000 integration features while keeping all shared genes for further analysis (Please see attached analysis code, Supplemental Table 6). Standard parameters for visualization and clustering were used throughout the analysis. Clusters were identified based on marker genes and subsequently joined into larger groups (Supplemental Table 3-6).

Multi-parameter Flow Cytometry

Cells were plated to 96-well V-bottom plate (Westnet Inc., 3894) and incubated with Zombie NIR Fixable Viability Kit (BioLegend, 423105) for 15 min at room temperature. The cells were washed with the staining buffer (PBS + 1% BSA + 0.1% Sodium Azide) and then blocked with anti-mouse CD16/32 (BioLegend, 101302) in staining buffer for 10 min on ice. Cells were incubated with primary antibodies for 30 min on ice and then washed with staining buffer. The antibody panels and the list of the antibodies are given in flow cytometry antibody tables below. Detection of intracellular markers was carried out using the FoxP3 intracellular staining kit (Thermo 00-5523-00) following the manufacturer's protocol. Immunostained cells were run on an LSR Fortessa HTS or LSR Fortessa with FACS DIVA software and analyzed using FlowJo V10.5.3. See supplementary Method Table 4-5 for the antibody panels used for multi-parameter flow cytometry.

RNA-sequencing

For bulk-tumor RNA-seq, omental tumors were harvested and then flash-frozen in liquid nitrogen. For total RNA extraction, *mirVana* miRNA Isolation Kit, with phenol (Thermo Fisher Scientific, AM1560), was used according to the manufacturer's instructions. For RNA extraction from cell lines, cells were lysed with QIAzol lysis reagent and then flash-frozen in liquid nitrogen. For total RNA extraction, the miRNeasy RNA extraction kit (Thermo Fisher Scientific, 217004) was used according to the manufacturer's instructions. All the samples in this study were sent to BPF Next-Gen Sequencing Core Facility at Harvard Medical School for RNA sequencing.

For RNA-seq analysis: mapping, differential expression, and gene enrichment analysis- The 75 nt long reads were mapped with STAR 2.7.1 (77) to the mm10 version of the mouse genome using the "sjdbOverhang" parameter set to 74, an annotation file from ENSEMBL version GRCm38.97 and the "alignIntronMax" parameter set to 50000. We had between 9 and 17 million reads per sample and mapped between 7.5 and 14 million reads per sample.

The number of counts per gene was obtained using featureCounts (78) with the "-s" parameter set to 2, the same annotation file used for mapping, and the rest of the parameters left as the default option. Normalization and differential expression were done with DESeq2 (79); the genes with zero counts were removed in all samples. We converted mouse symbols to human symbols using orthologues from ENSEMBL. After that, we had between 14000 and 15000 genes that we ranked by fold changes and used as input into the GseaPreranked tool from the Broad Institute (48). We run the GseaPreranked tool using the hallmark annotation, "h.all.v7.1.symbols.gmt", and

the GO annotation, "c5.all.v7.1.symbols.gmt", files downloaded from the Broad Institute. Dot plots of the enrichment analysis were done using a custom R script and the outputs from the GseaPreranked tool.

***In situ* Hybridization**

RNAscope 2.5 HD Detection Kit (Advanced Cell Diagnostics, ACD) was used for the *in-situ* Hybridization of Follistatin (FST) (RNAscope Probe no. Mm-Fst-454331) according to the manufacturer's instructions for formalin-fixed paraffin-embedded tissue sections. Briefly, the fixed omental samples were passed through the alcohol series, cleared with xylene, and embedded in paraffin blocks. Subsequently, 5- μ m-thick parts were cut from the paraffin-embedded blocks. RNAscope 2.5 HD Detection Reagent – RED (ACD, 322360) kit, along with assay controls RNAscope Probe - Mm-Ppib (ACD, 313911) and RNAscope Probe – DapB (ACD, 310043) was used according to the manufacturer's instructions. After the staining, slides were mounted, and whole-slide scanned (20X magnification) at the Histology Core Facility, Koch Institute for Integrative Cancer Research at MIT.

Cytokine and Chemokine Analysis

The Mouse Cytokine Array/Chemokine Array 44-Plex (MD44) and Cytokine Array, TGF-beta 3-Plex (Multi-Species) (TGFB1-3) were used at the recommended dilutions. For HGSC mouse models, the cytokine and chemokine analyses were performed from both cell culture- and ascites-supernatant samples. For HGSC mouse models, the cytokine and chemokine analysis on cell culture supernatants, cells were seeded to a 12-well tissue culture plate and were allowed to adhere overnight. The next day the cells were washed twice with PBS and then replenished with serum-free DME plus 1% penicillin/streptomycin media. After 24 hours, cell culture supernatants were collected on ice and then flash-frozen on dry ice. Ascites- and cell culture- supernatants were profiled for cytokine and chemokines using services at Eve Technologies (Calgary, Canada).

For mouse cytokine/chemokine analysis, the intensity measurements out of the observed range in >60% of the samples were removed from the analysis (TIMP, IL-16, 6Ckine/Exodus 2). Concentrations corresponding to intensity values out of range were imputed with the most extreme value from the expected concentration in the standard curve for each cytokine. Samples were grouped based on the genotype and subjected to the non-parametric Mann-Whitney test to identify differentially expressed cytokines between the two groups, and visualized using z-score column normalization and hierarchical clustering.

The Human Cytokine/Chemokine 65-Plex Panel (HD65) and TGF-beta 3-Plex (Multi-Species) Cytokine Array (TGFB1-3) were used at the recommended dilutions. Cytokines with out of the observed range intensity measurements in >60% of the samples were removed from the analysis (TIMP, IL-16, 6Ckine/Exodus 2). Concentrations corresponding to intensity values out of range were imputed with the most extreme value from the expected concentration in the standard curve for each cytokine. Outliers in the human samples were detected with multidimensional scaling and removed (ascites and serum 2, 5, 10, 14). Samples were grouped into HR-proficient and HR-deficient based on the genotype and subjected to the non-parametric Mann-Whitney test to identify differentially expressed cytokines between the two groups. Patient ascites supernatants were profiled for cytokine and chemokines using services at Eve Technologies (Calgary, Canada). The patient gave their informed consent to participate in the Hercules study, and the study was conducted in accordance with Declaration of Helsinki, and approved by The Ethics Committee of the Hospital District of Southwest Finland, päätös: ETMK Dnro: 145 /1801/2015.

ELISA from cell culture supernatants measured the levels of Follistatin (FST). Mouse FST ELISA Kit (Ray Biotech, ELM-FST-1) was used according to manufacturers' instructions. Briefly, cells were seeded to a 12-well tissue culture plate and allowed to adhere overnight. The next day the cells were washed twice with PBS and then replenished and stimulated with serum-free DME plus the stimulants or unstimulated (as a control group) for ELISA. For FST ELISA assay, TGF- β (R&D Systems, 240-B-002) was added as the stimulant for 24hours before the collection of the supernatant. Absorbances were measured according to the manufacturer's instructions. Graphpad Prism 8 was used for analysis.

Chemotaxis Cell Migration Assay

To examine tumor-infiltrating immune cell migration, we used *in vitro* Transwell chemotaxis assay (QCM Chemotaxis Cell Migration Assay, 24-well (5 μ m), Fluorimetric Activity Assay (MilliporeSigma, ECM507). Briefly, we collected cell culture supernatants (as described above) from BPPNM and KPCA cells and freshly isolated purified CD45+ cells (CD45 (TIL) MicroBeads, mouse (Miltenyi Biotec, 130-110-618) from BPPNM and KPCA tumors (Supplemental Figure 4E). Purified CD45+ cells (CD45 Microbeads, mouse (Miltenyi Biotec, 130-097-153) were used to control check purity of sorted CD45+ cells (Supplemental Figure 4E). Freshly purified bulk CD45+ cells from BPPNM or KPCA tumors were placed in the top well of the Transwell chamber. Supernatants from BPPNM or KPCA cells were placed in the lower chamber with or without appropriate neutralizing antibodies (Mouse GM-CSF Antibody (0.3 μ g/mL R&D Systems,

MAB415) and TGF-beta 1,2,3 (3 µg/mL R&D Systems, MAB1835)). The Transwell plates were incubated for 16-18 hours at 37C under a 5% CO₂ atmosphere. The inserts were removed, and cells that had migrated to each bottom well were collected and then incubated with primary antibodies (cell surface antibodies) for 30 min on ice and then washed with staining buffer with DAPI (for Live/Dead staining). The antibody panels and the list of the antibodies are given in flow cytometry antibody tables below. Immunostained cells were run on an LSR Fortessa with FACS DIVA software and analyzed using FlowJo V10.5.3. Each antibody and controls were tested in triplicate. The data presented are pooled from two independent experiments. See Supplementary Method Table 4-5 for the Antibody panels used for multi-parameter flow cytometry.

Whole-Exome Sequencing

DNA was extracted from cells using the Purelink Genomic DNA Mini kit (Life Technologies, K182001), following the manufacturer's instructions. The samples were sent to the Beijing Genomics Institute (BGI) for DNBseq whole-exome sequencing. Exome reads were filtered to remove low-quality reads and then mapped to the mouse genome (mm10) using bwa mem (version 0.7.15). Multi-mapped reads were removed, producing 190-fold coverage across targeted regions. Single-nucleotide variants (SNVs) were identified in both samples using GATK's HaplotypeCaller. SNVs were filtered with GATK (using `--filterExpression "QD<2.0 || FS>60 || MQ<40 || MQRankSum<-12.5 || ReadPosRankSum<-8.0"`). SNV positions were further characterized using bam-readcount (version 0.7.4) by counting reads supporting each allele at each position. The overall most prevalent variant at each SNV position was determined, and the fraction of reads supporting that allele was calculated for each sample. After adding 0.1 to each fraction (to avoid division by 0), these allele fractions were compared at each SNV position. Furthermore, to identify variants, positions with coverage of at least 50 reads and at least a 2-fold difference between samples were highlighted in blue.

Analysis of copy number alterations and HRD-LOH score

DNA was extracted from cells using the Purelink Genomic DNA Mini kit (Life Technologies, K182001), following the manufacturer's instructions. The samples were sent to NYU Langone's Genome Technology Center for low pass whole-genome sequencing. Paired reads from whole-genome sequencing were mapped to the mouse genome (mm10) using bwa mem (version 0.7.15) with default settings. After removing any mappings to chrM or chrY, read-depth variations and CNAs were identified using the program Control-FREEC (24) v11.6 using SNPs from Ensembl Release 101, a GEM mappability file, and the following settings: window=50000,

breakPointThreshold=0.6, minimalCoveragePerPosition=1, minimalQualityPerPosition=5, ploidy=2, sex=XX, and shiftInQuality=33. CNAs with a high level of uncertainty (> 95 percentage) were ignored. The LOH events > 15MB (25) were identified using the program scarHRD (26).

ATAC-seq analysis

Cells were harvested and frozen in culture media containing FBS and 5% DMSO. Cryopreserved cells were sent to Active Motif to perform the ATAC-seq assay. The cells were then thawed in a 37C water bath, pelleted, washed with cold PBS, and tagmented as previously described (1), with some modifications based on (2). Briefly, cell pellets were resuspended in lysis buffer, pelleted, and tagmented using the enzyme and buffer provided in the Nextera Library Prep Kit (Illumina). Tagmented DNA was then purified using the MinElute PCR purification kit (Qiagen), amplified with ten cycles of PCR, and purified using Agencourt AMPure SPRI beads (Beckman Coulter). The resulting material was quantified using the KAPA Library Quantification Kit for Illumina platforms (KAPA Biosystems) and sequenced with PE42 sequencing on the NextSeq 500 sequencer (Illumina).

Paired-end reads were filtered to remove low-quality reads and then mapped to the mouse genome (mm10) using bwa mem (version 0.7.12), and peaks were called with MACS v2.1.0. Peaks were merged across samples, and read coverage of each peak was determined with "bedtools coverage." For each Fst peak, chromatin accessibility was compared between samples with Fisher's exact test, using contingency tables of read counts for one peak and for all peaks on that chromosome. The p-values were FDR corrected. For the combined Fst peaks, chromatin accessibility was compared similarly, using contingency tables of read counts across four peaks and for all peaks on that chromosome.

TCGA ovarian cancer survival analysis

Using genomic and transcriptomic data from the TCGA, we identified 78 patients with *BRCA1/2* deficiency as defined by *BRCA1/2* somatic or germline mutation or hypermethylation, and 72 patients with *CCNE1* amplified tumors with corresponding transcriptomic gene-expression and survival data. The FST mRNA expression levels were normalized for fragments per kilobase million (FPKM), log-transformed, and divided into high and low based on the median expression. Differences between the progression-free survival as the time from diagnosis to recurrence, or overall survival as the time from diagnosis to death, were evaluated with the Kaplan-Meier method

using the Log-rank test or Cox regression analysis. The results shown here are in whole or part based upon data generated by the TCGA Research Network: <https://www.cancer.gov/tcga>.

Statistical analysis

Statistical analysis was performed using GraphPad Prism 8 software (GraphPad Software, Inc.), using an independent sample *t*-test unless otherwise indicated. $P \leq 0.05$ was considered as significant. Data are represented as mean \pm standard error of the mean (SEM). The log-rank (Mantel-Cox) test was used to analyze the survival difference in the treatment and the untreated-matched cohorts

Acknowledgments

We would like to thank members of the Weinberg lab, Richard Goldsby and Kevin M. Elias, for essential comments and suggestions during this work. We would also like to thank Yeku Oladapo and Patricia K Donahoe for their comments on the manuscript. We would like to thank Duygu Hatice Saatcioglu and Raghav Mohan for assistance in processing tissues for scRNA sequencing. We would like to thank Dong Dong, Tian Xia, Omer Faruk Karakaya, and Tony E Chavarria for assistance in processing tumor tissues. We would like to thank Sunny Das for help in the synergy analysis. We would like to thank Roderick T. Bronson for assistance in the histopathological examination of the tumors. The cartoons were created with BioRender.com. We would like to thank the Flow Cytometry Core Facility at the Whitehead Institute for Biomedical Research. We would like to thank Hope Babette Tang Histology Facility, Swanson Biotechnology Center Flow Cytometry Core, and High Throughput Sciences Core Facilities at Koch Institute for Integrative Cancer Research at MIT. We thank BPF Next-Gen Sequencing Core Facility at Harvard Medical School for RNA sequencing. We thank the NYU Langone's Genome Technology Center for whole-genome sequencing. We thank the Active Motif for the ATAC-seq assay. We thank the Beijing Genomics Institute (BGI) for whole-exome sequencing. We thank the Eve Technologies (Calgary, Canada) services for cytokine and chemokines.

SI was supported by the post-doctoral fellowship by Ludwig Fund for Cancer Research and Amgen. RAW was funded by grants from the National Institutes of Health (R01 CA0784561 and P01 CA080111), Samuel Waxman Cancer Research Foundation, Breast Cancer Research Foundation, and Ludwig Fund for Cancer Research. This work was supported by the Bridge Project, a partnership between the Koch Institute for Integrative Cancer Research at MIT and the Dana-Farber/Harvard Cancer Center. DP was supported by the Assistant Secretary of Defense

for Health Affairs, through the Ovarian Cancer Research Program under Award No. W81XWH-17-1-0212. The US Army Medical Research Acquisition Activity, 820 Chandler Street, Fort Detrick MD 21702-5014 is the awarding and administering acquisition office. Opinions, interpretations, conclusions, and recommendations are those of the author and are not necessarily endorsed by the Department of Defense. In conducting research using animals, the investigator(s) adheres to the laws of the United States and regulations of the Department of Agriculture.

Reference:

1. Cancer Genome Atlas Research N. Integrated genomic analyses of ovarian carcinoma. *Nature* **2011**;474(7353):609-15 doi 10.1038/nature10166.
2. Moore K, Colombo N, Scambia G, Kim BG, Oaknin A, Friedlander M, *et al.* Maintenance Olaparib in Patients with Newly Diagnosed Advanced Ovarian Cancer. *N Engl J Med* **2018** doi 10.1056/NEJMoa1810858.
3. Konstantinopoulos PA, Ceccaldi R, Shapiro GI, D'Andrea AD. Homologous Recombination Deficiency: Exploiting the Fundamental Vulnerability of Ovarian Cancer. *Cancer Discov* **2015**;5(11):1137-54 doi 10.1158/2159-8290.CD-15-0714.
4. Au-Yeung G, Lang F, Azar WJ, Mitchell C, Jarman KE, Lackovic K, *et al.* Selective Targeting of Cyclin E1-Amplified High-Grade Serous Ovarian Cancer by Cyclin-Dependent Kinase 2 and AKT Inhibition. *Clin Cancer Res* **2017**;23(7):1862-74 doi 10.1158/1078-0432.CCR-16-0620.
5. Coukos G, Tanyi J, Kandalaft LE. Opportunities in immunotherapy of ovarian cancer. *Ann Oncol* **2016**;27 Suppl 1:i11-i5 doi 10.1093/annonc/mdw084.
6. Ribas A, Wolchok JD. Cancer immunotherapy using checkpoint blockade. *Science* **2018**;359(6382):1350-5 doi 10.1126/science.aar4060.
7. Matulonis UA, Shapira-Frommer R, Santin AD, Lisyanskaya AS, Pignata S, Vergote I, *et al.* Antitumor activity and safety of pembrolizumab in patients with advanced recurrent ovarian cancer: results from the phase II KEYNOTE-100 study. *Ann Oncol* **2019**;30(7):1080-7 doi 10.1093/annonc/mdz135.
8. Disis ML, Taylor MH, Kelly K, Beck JT, Gordon M, Moore KM, *et al.* Efficacy and Safety of Avelumab for Patients With Recurrent or Refractory Ovarian Cancer: Phase 1b Results From the JAVELIN Solid Tumor Trial. *JAMA Oncol* **2019**;5(3):393-401 doi 10.1001/jamaoncol.2018.6258.
9. Keenan TE, Burke KP, Van Allen EM. Genomic correlates of response to immune checkpoint blockade. *Nat Med* **2019**;25(3):389-402 doi 10.1038/s41591-019-0382-x.
10. Kuhn E, Tisato V, Rimondi E, Secchiero P. Current preclinical models of ovarian cancer. *J Carcinog Mutagen* **2015**;6(2):220.
11. Roby KF, Taylor CC, Sweetwood JP, Cheng Y, Pace JL, Tawfik O, *et al.* Development of a syngeneic mouse model for events related to ovarian cancer. *Carcinogenesis* **2000**;21(4):585-91 doi 10.1093/carcin/21.4.585.
12. Walton J, Blagih J, Ennis D, Leung E, Dowson S, Farquharson M, *et al.* CRISPR/Cas9-Mediated Trp53 and Brca2 Knockout to Generate Improved Murine Models of Ovarian High-Grade Serous Carcinoma. *Cancer Res* **2016**;76(20):6118-29 doi 10.1158/0008-5472.CAN-16-1272.
13. Janat-Amsbury MM, Yockman JW, Anderson ML, Kieback DG, Kim SW. Comparison of ID8 MOSE and VEGF-modified ID8 cell lines in an immunocompetent animal model for human ovarian cancer. *Anticancer Res* **2006**;26(4B):2785-9.
14. Stuckelberger S, Drapkin R. Precious GEMMs: emergence of faithful models for ovarian cancer research. *J Pathol* **2018**;245(2):129-31 doi 10.1002/path.5065.
15. Zhai Y, Wu R, Kuick R, Sessine MS, Schulman S, Green M, *et al.* High-grade serous carcinomas arise in the mouse oviduct via defects linked to the human disease. *J Pathol* **2017**;243(1):16-25 doi 10.1002/path.4927.
16. Kim J, Coffey DM, Creighton CJ, Yu Z, Hawkins SM, Matzuk MM. High-grade serous ovarian cancer arises from fallopian tube in a mouse model. *Proc Natl Acad Sci U S A* **2012**;109(10):3921-6 doi 10.1073/pnas.1117135109.
17. Perets R, Wyant GA, Muto KW, Bijron JG, Poole BB, Chin KT, *et al.* Transformation of the fallopian tube secretory epithelium leads to high-grade serous ovarian cancer in Brca;Tp53;Pten models. *Cancer Cell* **2013**;24(6):751-65 doi 10.1016/j.ccr.2013.10.013.

18. Karst AM, Levanon K, Drapkin R. Modeling high-grade serous ovarian carcinogenesis from the fallopian tube. *Proc Natl Acad Sci U S A* **2011**;108(18):7547-52 doi 10.1073/pnas.1017300108.
19. Crum CP, Drapkin R, Kindelberger D, Medeiros F, Miron A, Lee Y. Lessons from BRCA: the tubal fimbria emerges as an origin for pelvic serous cancer. *Clin Med Res* **2007**;5(1):35-44 doi 10.3121/cmr.2007.702.
20. Liu X, Holstege H, van der Gulden H, Treur-Mulder M, Zevenhoven J, Velds A, *et al.* Somatic loss of BRCA1 and p53 in mice induces mammary tumors with features of human BRCA1-mutated basal-like breast cancer. *Proc Natl Acad Sci U S A* **2007**;104(29):12111-6 doi 10.1073/pnas.0702969104.
21. Alamo P, Gallardo A, Di Nicolantonio F, Pavon MA, Casanova I, Trias M, *et al.* Higher metastatic efficiency of KRas G12V than KRas G13D in a colorectal cancer model. *FASEB J* **2015**;29(2):464-76 doi 10.1096/fj.14-262303.
22. Qiu P, Shandilya H, D'Alessio JM, O'Connor K, Durocher J, Gerard GF. Mutation detection using Surveyor nuclease. *Biotechniques* **2004**;36(4):702-7 doi 10.2144/04364PF01.
23. Pao W, Wang TY, Riely GJ, Miller VA, Pan Q, Ladanyi M, *et al.* KRAS mutations and primary resistance of lung adenocarcinomas to gefitinib or erlotinib. *PLoS Med* **2005**;2(1):e17 doi 10.1371/journal.pmed.0020017.
24. Abkevich V, Timms KM, Hennessy BT, Potter J, Carey MS, Meyer LA, *et al.* Patterns of genomic loss of heterozygosity predict homologous recombination repair defects in epithelial ovarian cancer. *Br J Cancer* **2012**;107(10):1776-82 doi 10.1038/bjc.2012.451.
25. Boeva V, Popova T, Bleakley K, Chiche P, Cappo J, Schleiermacher G, *et al.* Control-FREEC: a tool for assessing copy number and allelic content using next-generation sequencing data. *Bioinformatics* **2012**;28(3):423-5 doi 10.1093/bioinformatics/btr670.
26. Sztupinszki Z, Diossy M, Krzystanek M, Reiniger L, Csabai I, Favero F, *et al.* Migrating the SNP array-based homologous recombination deficiency measures to next generation sequencing data of breast cancer. *NPJ Breast Cancer* **2018**;4:16 doi 10.1038/s41523-018-0066-6.
27. Mendes-Pereira AM, Martin SA, Brough R, McCarthy A, Taylor JR, Kim JS, *et al.* Synthetic lethal targeting of PTEN mutant cells with PARP inhibitors. *EMBO Mol Med* **2009**;1(6-7):315-22 doi 10.1002/emmm.200900041.
28. Yin Y, Shen WH. PTEN: a new guardian of the genome. *Oncogene* **2008**;27(41):5443-53 doi 10.1038/onc.2008.241.
29. Shen WH, Balajee AS, Wang J, Wu H, Eng C, Pandolfi PP, *et al.* Essential role for nuclear PTEN in maintaining chromosomal integrity. *Cell* **2007**;128(1):157-70 doi 10.1016/j.cell.2006.11.042.
30. Qiu Z, Oleinick NL, Zhang J. ATR/CHK1 inhibitors and cancer therapy. *Radiother Oncol* **2018**;126(3):450-64 doi 10.1016/j.radonc.2017.09.043.
31. Lee JM, Nair J, Zimmer A, Lipkowitz S, Annunziata CM, Merino MJ, *et al.* Prexasertib, a cell cycle checkpoint kinase 1 and 2 inhibitor, in BRCA wild-type recurrent high-grade serous ovarian cancer: a first-in-class proof-of-concept phase 2 study. *Lancet Oncol* **2018**;19(2):207-15 doi 10.1016/S1470-2045(18)30009-3.
32. Lengyel E. Ovarian cancer development and metastasis. *Am J Pathol* **2010**;177(3):1053-64 doi 10.2353/ajpath.2010.100105.
33. Bowtell DD, Bohm S, Ahmed AA, Aspuria PJ, Bast RC, Jr., Beral V, *et al.* Rethinking ovarian cancer II: reducing mortality from high-grade serous ovarian cancer. *Nat Rev Cancer* **2015**;15(11):668-79 doi 10.1038/nrc4019.
34. Klein AM, Mazutis L, Akartuna I, Tallapragada N, Veres A, Li V, *et al.* Droplet barcoding for single-cell transcriptomics applied to embryonic stem cells. *Cell* **2015**;161(5):1187-201 doi 10.1016/j.cell.2015.04.044.

35. Broz ML, Binnewies M, Boldajipour B, Nelson AE, Pollack JL, Erle DJ, *et al.* Dissecting the tumor myeloid compartment reveals rare activating antigen-presenting cells critical for T cell immunity. *Cancer Cell* **2014**;26(5):638-52 doi 10.1016/j.ccell.2014.09.007.
36. Jiang Y, Li Y, Zhu B. T-cell exhaustion in the tumor microenvironment. *Cell Death Dis* **2015**;6:e1792 doi 10.1038/cddis.2015.162.
37. Wherry EJ. T cell exhaustion. *Nat Immunol* **2011**;12(6):492-9 doi 10.1038/ni.2035.
38. Kumar V, Patel S, Tcyganov E, Gabilovich DI. The Nature of Myeloid-Derived Suppressor Cells in the Tumor Microenvironment. *Trends Immunol* **2016**;37(3):208-20 doi 10.1016/j.it.2016.01.004.
39. Giuntoli RL, 2nd, Webb TJ, Zoso A, Rogers O, Diaz-Montes TP, Bristow RE, *et al.* Ovarian cancer-associated ascites demonstrates altered immune environment: implications for antitumor immunity. *Anticancer Res* **2009**;29(8):2875-84.
40. Kipps E, Tan DS, Kaye SB. Meeting the challenge of ascites in ovarian cancer: new avenues for therapy and research. *Nat Rev Cancer* **2013**;13(4):273-82 doi 10.1038/nrc3432.
41. Cardenas H, Jiang G, Thomes Pepin J, Parker JB, Condello S, Nephew KP, *et al.* Interferon-gamma signaling is associated with BRCA1 loss-of-function mutations in high grade serous ovarian cancer. *NPJ Precis Oncol* **2019**;3:32 doi 10.1038/s41698-019-0103-4.
42. Jimenez-Sanchez A, Memon D, Pourpe S, Veeraraghavan H, Li Y, Vargas HA, *et al.* Heterogeneous Tumor-Immune Microenvironments among Differentially Growing Metastases in an Ovarian Cancer Patient. *Cell* **2017**;170(5):927-38 e20 doi 10.1016/j.cell.2017.07.025.
43. Jimenez-Sanchez A, Cybulska P, Mager KL, Koplev S, Cast O, Couturier DL, *et al.* Unraveling tumor-immune heterogeneity in advanced ovarian cancer uncovers immunogenic effect of chemotherapy. *Nat Genet* **2020**;52(6):582-93 doi 10.1038/s41588-020-0630-5.
44. Lee J, Ahn E, Kissick HT, Ahmed R. Reinvigorating Exhausted T Cells by Blockade of the PD-1 Pathway. *For Immunopathol Dis Therap* **2015**;6(1-2):7-17 doi 10.1615/ForumImmunDisTher.2015014188.
45. Wherry EJ, Kurachi M. Molecular and cellular insights into T cell exhaustion. *Nat Rev Immunol* **2015**;15(8):486-99 doi 10.1038/nri3862.
46. Stewart RA, Pilie PG, Yap TA. Development of PARP and Immune-Checkpoint Inhibitor Combinations. *Cancer Res* **2018**;78(24):6717-25 doi 10.1158/0008-5472.CAN-18-2652.
47. Ding L, Kim HJ, Wang Q, Kearns M, Jiang T, Ohlson CE, *et al.* PARP Inhibition Elicits STING-Dependent Antitumor Immunity in Brca1-Deficient Ovarian Cancer. *Cell Rep* **2018**;25(11):2972-80 e5 doi 10.1016/j.celrep.2018.11.054.
48. Subramanian A, Tamayo P, Mootha VK, Mukherjee S, Ebert BL, Gillette MA, *et al.* Gene set enrichment analysis: a knowledge-based approach for interpreting genome-wide expression profiles. *Proc Natl Acad Sci U S A* **2005**;102(43):15545-50 doi 10.1073/pnas.0506580102.
49. Farkkila A, Gulhan DC, Casado J, Jacobson CA, Nguyen H, Kochupurakkal B, *et al.* Immunogenomic profiling determines responses to combined PARP and PD-1 inhibition in ovarian cancer. *Nat Commun* **2020**;11(1):1459 doi 10.1038/s41467-020-15315-8.
50. Etemadmoghadam D, Weir BA, Au-Yeung G, Alsop K, Mitchell G, George J, *et al.* Synthetic lethality between CCNE1 amplification and loss of BRCA1. *Proc Natl Acad Sci U S A* **2013**;110(48):19489-94 doi 10.1073/pnas.1314302110.
51. Wei SC, Anang NAS, Sharma R, Andrews MC, Reuben A, Levine JH, *et al.* Combination anti-CTLA-4 plus anti-PD-1 checkpoint blockade utilizes cellular mechanisms partially distinct from monotherapies. *Proc Natl Acad Sci U S A* **2019**;116(45):22699-709 doi 10.1073/pnas.1821218116.

52. Sen T, Rodriguez BL, Chen L, Corte CMD, Morikawa N, Fujimoto J, *et al.* Targeting DNA Damage Response Promotes Antitumor Immunity through STING-Mediated T-cell Activation in Small Cell Lung Cancer. *Cancer Discov* **2019**;9(5):646-61 doi 10.1158/2159-8290.CD-18-1020.
53. Fazzini M, Vallejo G, Colman-Lerner A, Trigo R, Campo S, Baranao JL, *et al.* Transforming growth factor beta1 regulates follistatin mRNA expression during in vitro bovine granulosa cell differentiation. *J Cell Physiol* **2006**;207(1):40-8 doi 10.1002/jcp.20533.
54. Hedger MP, Winnall WR, Phillips DJ, de Kretser DM. The regulation and functions of activin and follistatin in inflammation and immunity. *Vitam Horm* **2011**;85:255-97 doi 10.1016/B978-0-12-385961-7.00013-5.
55. Kaneko H. Subchapter 33C - Follistatin. In: Takei Y, Ando H, Tsutsui K, editors. *Handbook of Hormones*. San Diego: Academic Press; 2016. p 298-e33C-2.
56. Ren P, Chen FF, Liu HY, Cui XL, Sun Y, Guan JL, *et al.* High serum levels of follistatin in patients with ovarian cancer. *J Int Med Res* **2012**;40(3):877-86 doi 10.1177/147323001204000306.
57. Antsiferova M, Werner S. The bright and the dark sides of activin in wound healing and cancer. *J Cell Sci* **2012**;125(Pt 17):3929-37 doi 10.1242/jcs.094789.
58. Morianos I, Papadopoulou G, Semitekolou M, Xanthou G. Activin-A in the regulation of immunity in health and disease. *J Autoimmun* **2019**;104:102314 doi 10.1016/j.jaut.2019.102314.
59. Saatcioglu HD, Kano M, Horn H, Zhang L, Samore W, Nagykerly N, *et al.* Single-cell sequencing of neonatal uterus reveals an Misr2+ endometrial progenitor indispensable for fertility. *Elife* **2019**;8 doi 10.7554/eLife.46349.
60. Yang L, Pang Y, Moses HL. TGF-beta and immune cells: an important regulatory axis in the tumor microenvironment and progression. *Trends Immunol* **2010**;31(6):220-7 doi 10.1016/j.it.2010.04.002.
61. Thomas DA, Massague J. TGF-beta directly targets cytotoxic T cell functions during tumor evasion of immune surveillance. *Cancer Cell* **2005**;8(5):369-80 doi 10.1016/j.ccr.2005.10.012.
62. Nagarsheth N, Wicha MS, Zou W. Chemokines in the cancer microenvironment and their relevance in cancer immunotherapy. *Nat Rev Immunol* **2017**;17(9):559-72 doi 10.1038/nri.2017.49.
63. Strickland KC, Howitt BE, Shukla SA, Rodig S, Ritterhouse LL, Liu JF, *et al.* Association and prognostic significance of BRCA1/2-mutation status with neoantigen load, number of tumor-infiltrating lymphocytes and expression of PD-1/PD-L1 in high grade serous ovarian cancer. *Oncotarget* **2016**;7(12):13587-98 doi 10.18632/oncotarget.7277.
64. Emens LA, Middleton G. The interplay of immunotherapy and chemotherapy: harnessing potential synergies. *Cancer Immunol Res* **2015**;3(5):436-43 doi 10.1158/2326-6066.CIR-15-0064.
65. Kampan NC, Madondo MT, McNally OM, Stephens AN, Quinn MA, Plebanski M. Interleukin 6 Present in Inflammatory Ascites from Advanced Epithelial Ovarian Cancer Patients Promotes Tumor Necrosis Factor Receptor 2-Expressing Regulatory T Cells. *Front Immunol* **2017**;8:1482 doi 10.3389/fimmu.2017.01482.
66. Park MJ, Lee SH, Kim EK, Lee EJ, Baek JA, Park SH, *et al.* Interleukin-10 produced by myeloid-derived suppressor cells is critical for the induction of Tregs and attenuation of rheumatoid inflammation in mice. *Sci Rep* **2018**;8(1):3753 doi 10.1038/s41598-018-21856-2.
67. Vignali DA, Collison LW, Workman CJ. How regulatory T cells work. *Nat Rev Immunol* **2008**;8(7):523-32 doi 10.1038/nri2343.

68. Shi L, Resaul J, Owen S, Ye L, Jiang WG. Clinical and Therapeutic Implications of Follistatin in Solid Tumours. *Cancer Genomics Proteomics* **2016**;13(6):425-35 doi 10.21873/cgp.20005.
69. Cash JN, Rejon CA, McPherron AC, Bernard DJ, Thompson TB. The structure of myostatin:follistatin 288: insights into receptor utilization and heparin binding. *EMBO J* **2009**;28(17):2662-76 doi 10.1038/emboj.2009.205.
70. Dreaden EC, Kong YW, Quadir MA, Correa S, Suarez-Lopez L, Barberio AE, *et al.* RNA-Peptide nanoplexes drug DNA damage pathways in high-grade serous ovarian tumors. *Bioeng Transl Med* **2018**;3(1):26-36 doi 10.1002/btm2.10086.
71. Gu L, Deng ZJ, Roy S, Hammond PT. A Combination RNAi-Chemotherapy Layer-by-Layer Nanoparticle for Systemic Targeting of KRAS/P53 with Cisplatin to Treat Non-Small Cell Lung Cancer. *Clin Cancer Res* **2017**;23(23):7312-23 doi 10.1158/1078-0432.CCR-16-2186.
72. Zhang S, Iyer S, Ran H, Dolgalev I, Wei W, Foster C, *et al.* Genetically Defined, Syngeneic Organoid Platform for Developing Combination Therapies for Ovarian Cancer. *bioRxiv* **2020**:2020.04.06.028597 doi 10.1101/2020.04.06.028597.
73. Zhang S, Dolgalev I, Zhang T, Ran H, Levine DA, Neel BG. Both fallopian tube and ovarian surface epithelium are cells-of-origin for high-grade serous ovarian carcinoma. *Nat Commun* **2019**;10(1):5367 doi 10.1038/s41467-019-13116-2.
74. Lanni JS, Jacks T. Characterization of the p53-dependent postmitotic checkpoint following spindle disruption. *Mol Cell Biol* **1998**;18(2):1055-64 doi 10.1128/mcb.18.2.1055.
75. Oplustil O'Connor L, Rulten SL, Cranston AN, Odedra R, Brown H, Jaspers JE, *et al.* The PARP Inhibitor AZD2461 Provides Insights into the Role of PARP3 Inhibition for Both Synthetic Lethality and Tolerability with Chemotherapy in Preclinical Models. *Cancer Res* **2016**;76(20):6084-94 doi 10.1158/0008-5472.CAN-15-3240.
76. Ianevski A, He L, Aittokallio T, Tang J. SynergyFinder: a web application for analyzing drug combination dose-response matrix data. *Bioinformatics* **2017**;33(15):2413-5 doi 10.1093/bioinformatics/btx162.
77. Dobin A, Davis CA, Schlesinger F, Drenkow J, Zaleski C, Jha S, *et al.* STAR: ultrafast universal RNA-seq aligner. *Bioinformatics* **2013**;29(1):15-21 doi 10.1093/bioinformatics/bts635.
78. Liao Y, Smyth GK, Shi W. featureCounts: an efficient general purpose program for assigning sequence reads to genomic features. *Bioinformatics* **2014**;30(7):923-30 doi 10.1093/bioinformatics/btt656.
79. Love MI, Huber W, Anders S. Moderated estimation of fold change and dispersion for RNA-seq data with DESeq2. *Genome Biol* **2014**;15(12):550 doi 10.1186/s13059-014-0550-8.

Supplementary Method Table 1. Primer sequences for PCR--

Gene	Forward primer	Reverse primer
Brca1	TATCACCCTGAATCTCTACCG	TCCATAGCATCTCCTTCTAAA
Mutant p53 (R172H)	TGTGCACGTACTCTCCTCCC	CTTCTGTACGGCGGTCTCTC
Kras G12V	CATGGTCCTGCTGGAGTTCGTG	ACTCCTCTTGACCTGCTGTG

Supplementary Method Table 2. CRISPR/Cas9 Plasmids and sgRNA sequences for CRISPR/Cas9 targeting and confirmation using Sanger Sequencing of Modified Loci--

Mouse Target Gene/Plasmid	gRNA sequence 1	gRNA sequence 2	gRNA sequence 3
Pten (SC-422475)	ACCGCCAAATTTA ACTGCAG	GCAGCAATTCCT GTAAAGC	
Nf1 (SC-421861)	TCCGAAGTTCGGC TGCATGT	AGTCAGCACCGA GCACAACA	GTTGATCATATTG GATACAC
S100a4 (SC-422782)	GGTTACCATGGCA AGACCCT	AGGTGGACACAAT TACATCC	CCAAGTTGCTCAT CACCTTC
Fst (SC- 420417)	CGGCGGGAAAAA ATGCCTAT	AAGAGTGTTCAG CACCGGC	ATTGTCGTTTACA TCCTCCT
IL-33 (SC- 429508)	TACTGCATGAGAC TCCGTTC	CATAGTAGCGTAG TAGCACC	GTGATCAATGTTG ACGACTC

Supplementary Method Table 3. Antibodies used for immunofluorescence/immunohistochemistry analyses and western blotting--

Protein	Antibody Catalog no.	Company	Type	IF (dilution)	IHC (dilution)	Dilution Western
Pax8	10336-1-AP	Proteintech	Rabbit	1:250	1:2500	-
WT-1	ab89901	Abcam	Rabbit	-	1:300	-
CK-7	ab181598	Abcam	Rabbit	1:100	1:8000	-
Ki67	9449S	Cell Signaling	Rat	-	1:400	-
CD3e	ab16669	Abcam	Rabbit	-	1:50	-
CD8a	ab209775	Abcam	Rabbit	-	1:2000	-

Ly6G/Ly6C	14-5931-85	Invitrogen	Rat	-	1:50	-
F4/80	MF48000	Invitrogen	Rat	-	1:50	-
PD-L1	50-100-3217	Fisher Scientific	Mouse	-	1:1000	-
PTEN	9188S	Cell Signaling	Rabbit	-	-	1:1000
NF1	A300-140A	Bethyl Laboratories	Rabbit	-	-	1:2000
Myc	ab32072	Abcam	Rabbit	-	-	1:1000
SMARCA4	49360S	Cell Signaling	Rabbit	-	-	1:1000
BRD4	ab128874	Abcam	Rabbit	-	-	1:1000
CCNE1	20808S	Cell Signaling	Rabbit	-	-	1:1000
AKT2	5239S	Cell Signaling	Mouse	-	-	1:1000
Ras (G12V)	14412	Cell Signaling	Rabbit	-	-	1:1000
p53	2524S	Cell Signaling	Mouse	-	-	1:1000
Vinculin	13901S	Cell Signaling	Rabbit	-	-	1:1000
Phospho RPA32 (S4/S8)	A300-245A	Bethyl Laboratories	Rabbit	-	-	1:2000
Phospho-Histone H2A.X (Ser139)	2577S	Cell Signaling	Mouse	-	-	1:1000
β-Actin (13E5)	4970	Cell Signaling	Rabbit	-	-	1:1000
Phospho-Akt (Ser473) (D9E)	4060S	Cell Signaling	Rabbit	-	-	1:1000
Akt (pan) (11E7)	4685S	Cell Signaling	Rabbit	-	-	1:1000
p44/42 MAPK (Erk1/2) (137F5)	4695S	Cell Signaling	Rabbit	-	-	1:1000
Phospho-p44/42 MAPK	4370S	Cell Signaling	Rabbit	-	-	1:1000

(Erk1/2) (Thr202/Tyr204) (D13.14.4E)						
p21 Waf1/Cip1 (Mouse preferred)	64016S	Cell Signaling	Rabbit	-	-	1:1000
HSP90	4874S	Cell Signaling	Rabbit	-	-	1:1000
Phospho-mTOR (Ser2448) (D9C2)	5536T	Cell Signaling	Rabbit	-	-	1:1000
mTOR (7C10)	2983T	Cell Signaling	Rabbit	-	-	1:1000
Phospho-p70 S6 Kinase (Thr389) (108D2)	9234T	Cell Signaling	Rabbit	-	-	1:1000
p70 S6 Kinase (49D7)	2708T	Cell Signaling	Rabbit	-	-	1:1000
Akt2 (5B5)	2964S	Cell Signaling	Rabbit	-	-	1:1000
Phospho-p70 S6 Kinase (Ser371)	9208T	Cell Signaling	Rabbit	-	-	1:1000

Supplementary Method Table 4. Antibody panels used for multi-parameter flow cytometry-

Channel	Panel 1: T-Cell and T-reg	Panel 2: Myeloid	Panel 3: T-cell exhaustion phenotype	Panel 5: M1- like/M2- like
BUV396	CD25	CD274	PD-1/ Isotype	MHCII
BUV737	-	-	Lag3/ Isotype	CD86

BV421	FOXP3/ Isotype	F4/80	Tim3/ Isotype	F4/80
BV525	CD3e	CD11b	CD3e	CD11b
BV605	CD19	CD11c	TIGIT/ Isotype	CD11c
BV786	CD45	CD45	CD45	CD45
BB700	CD4	Ly6C	CD4	Ly6G
PE-Cy7	CD8	TIM-3	CD8	CD206
APC	NK1.1	Ly6G	CTLA4/ Isotype	iNOS/ Isotype

Channel	Panel for Chemotaxis assay
V450	DAPI
BV786	CD45
APC	CD11b
PE	F4/80
PerCP	Ly6G
PE-Cy7	Ly6C

Supplementary Table 5. Antibodies used for multi-parameter flow cytometry--

Marker	Antibody (Catalog Number)	Company
CD25	564022	BD Biosciences
FOXP3	562996	BD Biosciences
Isotype BV421	562603	BD Biosciences
CD3e	100353	BioLegend
CD19	115540	BioLegend
CD45	564225	BD Biosciences
CD4	100538	BioLegend
CD8a	100722	BioLegend
NK1.1	108710	BioLegend

CD274 (PDL1)	124321	BioLegend
F4/80	123132	BioLegend
CD11b	101263	BioLegend
CD11c	117334	BioLegend
Ly6C	128028	BioLegend
CD366 (TIM-3)	747626	BD Biosciences
Ly6G	127614	BioLegend
Ly6G	127615	BioLegend
CD279 (PD-1)	744549	BD Biosciences
CD223 (Lag-3)	741820	BD Biosciences
CD366 (Tim-3)	747626	BD Biosciences
CD366 (Tim-3)	134009	BioLegend
TIGIT	744212	BD Biosciences
CD152 (CTLA-4)	564331	BD Biosciences
MHCII	743876	BD Biosciences
CD86	741757	BD Biosciences
CD206	141719	BioLegend
iNOS	17-5920-82	Thermo Fisher Scientific
CD45	BDB564225	Thermo Fisher Scientific
CD11c	117337	BioLegend
CD11b	101212	BioLegend
Ly-6C	128017	BioLegend
Ly-6G	127653	BioLegend
F4/80	123110	BioLegend
CD3 ϵ	100306	BioLegend

Figure legends

Figure 1. Engineering strategy and *in vitro* characterization of the murine FTE-derived cells.

Schema showing the strategy for generation of (A) Non-classified and HR-deficient Pax8⁺ murine FTE-derived cells, *p53*^{-/-R172H}*Pten*^{-/-}*Nf1*^{-/-}*Myc*^{OE} (PPNM) and *Brca1*^{-/-}*p53*^{-/-R172H}*Pten*^{-/-}*Nf1*^{-/-}*Myc*^{OE} (BPPNM) and (B) HR-proficient Pax8⁺ murine FTE-derived cell lines *p53*^{-/-R172H}*Ccne1*^{OE}*Akt2*^{OE}*Brd4*^{OE} (BPCA), *p53*^{-/-R172H}*Ccne1*^{OE}*Akt2*^{OE}*Smarca4*^{OE} (SPCA) and *p53*^{-/-R172H}*Ccne1*^{OE}*Akt2*^{OE}*KRAS*^{G12V} (KPCA). (C) Representative images showing immunofluorescence staining of nuclear Paired box gene 8 (Pax8) (pink) and cytoplasmic Cytokeratin-7 (CK7) (white). Cell nuclei were stained with DAPI (blue). Images were taken with 63x magnification. (D) Representative images showing immunofluorescence staining of RAD51 and γ H2AX (upper panel) and, the quantification of the number of Rad51 foci per nuclei (lower panel). Cell nuclei were stained with DAPI (blue). Images were taken with 63x magnification. Dose-response curves for *p53*^{-/-}, BPPNM, PPNM, BPCA, SPCA, and KPCA cells with the treatment of (E) Carboplatin, (F) Niraparib and (G) Prexasertib. Cell viability was calculated relative to 0.01% vehicle-treated control cells, measured with Cell TiterGlo assay 72 hours after treatment. Data depicted are pooled from 2 independent experiments.

Supplemental Figure 1. *In vitro* validation and drug sensitivity of the engineered murine FTE-derived cells related to Figure 1.

(A) OncoPrint showing the mutation frequencies of HR-deficient associated and, HR-proficient associated genes in human HGSC (TCGA, PanCancer Atlas). (B) Agarose gel electrophoresis of PCR amplified products using the murine *Brca1* primer set. The order of the samples; 1. *p53*^{-/-}. 2. KPCA 3. *p53*^{-/-}*Brca1*^{-/-} 4. *p53*^{-/-}*Pten*^{-/-}*Nf1*^{-/-} 5. *p53*^{-/-}*Brca1*^{-/-}*Pten*^{-/-}*Nf1*^{-/-} 6. PPNM, 7. BPPNM. *Brca1* deleted allele detected at 594-bp in 3, 5, and 7. Sequence alignment results of (C) mutant *p53* *R172H* to PCR amplified products of BPPNM, PPNM, BPCA, SPCA, and KPCA cell lines. The analysis shows the point mutation *p53* *R172H* in all cell lines, (D) Mutant *KRAS* *G12V* to PCR amplified product of KPCA. The analysis showed the point mutation *KRAS* *G12V* in the KPCA cell line. SnapGene 5.1 was used for the analysis. (E) Sanger sequencing results of CRISPR/Cas9 modified loci showing the inactivating mutations of *Pten* and *Nf1* in PPNM and BPPNM cell lines. Western blot analysis showing expression of (F) PTEN, NF1, and Myc in established ovarian cancer cell lines and generated HR-deficient cell line, BPPNM and non-classified cell line, PPNM and (G) SMARCA4, BRD4, CCNE1, AKT2 and *KRAS*^{G12V} in established ovarian cancer cell lines and engineered HR-proficient cell lines BPCA, SPCA and KPCA. Vinculin served as a loading control. (H) Western blot analysis showing expression of Phospho-mTOR (Ser2448), mTOR, Phospho-AKT (Ser473), Pan-AKT, Phospho-p44/42 MAPK (Erk1/2) in A2780 established ovarian cancer cell line and engineered HR-deficient cell line, BPPNM and non-classified cell line, PPNM. p44/42 MAPK (Erk1/2) served as a loading control. (I) Western blot analysis showing expression of p21 Waf1/Cip1 with (+) or without (-) Nocodazole treatment in generated m-FTE cell lines. *p53* wild-type expressing MEF's served as a positive control for the assay. HSP90 served as a loading control. (J) Dose-response curves for the depicted cell lines with the treatment of Erlotinib. Cell viability was calculated relative to 0.01% vehicle-treated control cells, measured with Cell TiterGlo assay 72 hours after treatment. Data depicted are pooled from 2 independent experiments.

Supplemental Figure 2. *In vitro* validation and drug sensitivity of the engineered murine FTE-derived cells related to Figure 1 and Pax8 expression validation related to Figure 2

(A) Whole-genome copy-number profiles from Control-FREEC analysis are displayed, with red and blue points indicating 50kb windows with copy number greater than 2n or less than 2n, respectively. (B) Number of LOH events in the genetically engineered cell lines. Dose-response curves for the depicted cell lines with the treatment of (C) Cisplatin (D) Olaparib (E) Birabresib (OTX-015) (F) CPI-203 (G) JQ1. Cell viability was calculated relative to 0.01% vehicle-treated control cells, measured with Cell TiterGlo assay 72 hours after treatment. Data depicted are pooled from 2 independent experiments. (H) Validation of Pax8 expression by IHC, in the normal fallopian tube and the omental tumors derived from HGSC models.

Figure 2. *In vivo* characterization and drug sensitivity of the engineered murine FTE-derived BPPNM, PPNM and KPCA cells

(A) Genotypes of the engineered murine FTE-derived cell lines used for *in vivo* characterization. (B) Representative images showing ascites and peritoneal metastasis formation in immune-proficient C57BL/6 mice after intraperitoneal injection with engineered murine FTE-derived cells. Kaplan-Meier curves showing percent probability of survival of mice injected with (C) $p53^{-/-R172H}$, $p53^{-/-R172H}Pten^{-/-}$, $p53^{-/-R172H}Nf1^{-/-}$, $p53^{-/-R172H}Pten^{-/-}Nf1^{-/-}$, PPNM, and BPPNM cells and (D) with $p53^{-/-R172H}$, $p53^{-/-R172H}Ccne1^{OE}Akt2^{OE}$, BPCA, SPCA and KPCA cells. n=5 or more/group. (E) Representative images showing Hematoxylin and eosin (H&E) staining and immunohistochemical analysis of indicated markers on harvested BPPNM, PPNM, BPCA, SPCA and KPCA tumors. Scale bars: 200 μ m. (F) Experimental treatment strategy for single-agent Carboplatin, Olaparib, and Prexasertib as two weekly doses via the intraperitoneal route of administration for four weeks of duration. Kaplan-Meier curves showing percent probability of survival of mice injected with indicated engineered murine FTE-derived cell lines BPPNM, PPNM, and KPCA upon single-agent treatment with (G) Carboplatin, (H) Olaparib and (I) Prexasertib. n=5 or more/group. A log-rank test compared the survival curves of individual groups to vehicle-matched control mice, ns- non-significant, *p<0.05, **p<0.001, ***p<0.0001.

Figure 3. Cellular microenvironment analyses of omental tumors and ascites from BPPNM, PPNM, and KPCA tumor-bearing mice.

(A) UMAP plot of unbiased clustering the cellular components of merged BPPNM, PPNM, and KPCA omental tumors, where each color-coded cluster represents one cell type/state. Inset relative composition of the clusters. Each point represents one cell that is colored by its cell type/state. (B) Markers used to classify the clusters in panel 3A (see Supplemental Table 3 for the details). Immunophenotypic analysis by multi-parameter flow-cytometry showing the frequency of live adaptive and innate immune cells of representative (C) Omental tumors and (D) Ascites derived from HGSC mouse models. (E) Cytokine analysis of ascites supernatant HGSC mouse models. Data are presented as mean \pm SEM, * BPPNM vs KPCA, + PPNM vs KPCA and # BPPNM vs PPNM, *p<0.05, **p<0.001, ***p<0.0001, Multiple t-test. n=5 or more/group. (F) Depicts the transcript level cytokines and chemokine expression within the omental tumors of the HGSC mouse models by scRNA seq cluster analysis (panel 3A and 3B)

Supplemental Figure 3. Immune microenvironment and cytokine analyses of omental tumors and ascites from BPPNM, PPNM, and KPCA tumor-bearing mice related to Figure 3.

(A) UMAP plot of unbiased clustering the cellular components of merged BPPNM, KPCA and PPNM omental tumors, depicting the tumor genotypes, BPPNM (red), PPNM (purple) and KPCA (blue). Immunophenotypic analysis by multi-parameter flow cytometry showing the frequency of (B) M1- and M2-like macrophages and (C) CD8 T-cell exhaustion status of representative omental

tumors (D) CD8 T-cell exhaustion status of representative ascites derived from HGSC models. Data are presented as mean \pm SEM, * BPPNM vs KPCA, + PPNM vs KPCA and # BPPNM vs PPNM, * $p < 0.05$, ** $p < 0.001$, *** $p < 0.0001$, Multiple t-test. $n = 5$ or more/group. (E) Representative images showing H&E staining and immunohistochemical analysis of indicated immune markers on tumors harvested from HGSC models. Scale bars: 200 μm . (F) Heat map depicting the differentially expressed cytokines derived from ascites supernatant between the HGSC mouse models. (G) Heat map depicting the cytokines of pre-implanted cell culture supernatant derived from HGSC cell lines. (H) Cytokine levels of pre-implanted cell culture supernatants. * BPPNM vs KPCA, + PPNM vs KPCA and # BPPNM vs PPNM, * $p < 0.05$, ** $p < 0.001$, *** $p < 0.0001$, Multiple t-test. (I) Cytokine analysis of ascites supernatant HGSOC patients (*BRCA* mutated and *CCNE1*-amplified). (J) Comparison of cytokines from HGSOC patients and mouse model (this study). For human cytokine analysis, non-parametric Mann-Whitney test was used identify differentially expressed cytokines between the two groups.

Supplemental Figure 4. Gating strategy employed for immunophenotypic analyses and Immune cell migration assay Related to Figure 3.

Gating strategy for (A) Panel 1, adaptive immune cells and NK-cells, (B) Panel 2, Myeloid (C) Panel 3, T-cell exhaustion markers, and (D) Panel 4, M1- and M2-like macrophages. (E) Gating strategy of the bulk CD45⁺ cells and MACS sorted CD45⁺ cells from spleen, BPPNM tumors and KPCA tumors. (F) Schema showing the strategy for chemotaxis of CD45⁺ cells upon indirect co-culture with supernatants taken from BPPNM or KPCA cell lines. (G) Frequency of live CD45⁺ singlets cells from KPCA tumors upon anti-TGF- β 1/2/3 treatment. (H) Frequency of macrophages, Ly6G^{high}/Ly6C^{low} and Ly6G^{low}/Ly6C^{high} populations (Live CD45⁺) from KPCA tumors upon anti-TGF- β 1/2/3 treatment. (I) Frequency of live CD45⁺ singlets cells from BPPNM tumors upon anti-GM-CSF treatment. (J) Frequency of macrophages, Ly6G^{high}/Ly6C^{low} and Ly6G^{low}/Ly6C^{high} populations (Live CD45⁺) from BPPNM tumors upon anti-GM-CSF treatment. (K) Frequency of live CD45⁺ singlets cells from BPPNM tumors upon anti-TGF- β 1/2/3 treatment. (L) Frequency of macrophages, Ly6G^{high}/Ly6C^{low} and Ly6G^{low}/Ly6C^{high} populations (Live CD45⁺) from BPPNM tumors upon anti-TGF- β 1/2/3 treatment.

Figure 4. Evaluating optimal combination treatment strategies in BPPNM and PPNM tumor models.

Synergy analysis of Prexasertib and Olaparib treatment in (A) BPPNM and (B) PPNM cell lines. Synergy and antagonism between the drugs were determined using SynergyFinder (see material and methods section for more details). Cell viability was calculated relative to 0.01% vehicle-treated control cells, measured with Cell TiterGlo assay 72 hours after treatment. Data depicted are pooled from 2 independent experiments. (C) Experimental treatment strategy. Kaplan-Meier curves showing percent probability of survival of mice injected with engineered murine FTE-derived cell lines (D) BPPNM and (E) PPNM upon indicated treatment. $n = 5$ or more/group. A log-rank test compared the survival curves of individual groups to vehicle-matched control mice, * $p < 0.05$, ** $p < 0.001$, *** $p < 0.0001$. (F) Bulk-tumor RNA-seq analysis showing enrichment of distinct hallmark terms in *Brca1*-null HR-deficient ovarian model, BPPNM and non-classified *Brca1* wild-type, PPNM model. The figure shows the categories enriched in each comparison. The x-axis shows the normalized enrichment score. Gene sets are shown on the y-axis. The size of the dot represents the number of genes from the ranked list present on each gene set, and the color shows the FDR q-value. Cartoon models depicting (G) BPPNM and (H) PPNM tumor immune-microenvironment and sensitization strategies.

Figure 5. The sensitivity of HR-proficient *Ccne1*-overexpressing ovarian models to cell cycle checkpoint kinase- and immune checkpoint- inhibitors.

(A) Experimental treatment strategy. Kaplan-Meier curves showing percent probability of survival of mice injected with KPCA cell line (B and D) and KPCA.C cell line (C and E) upon indicated treatment. (F) Experimental treatment strategy for the depletion of CD8 T-cells using the anti-CD8 antibody. (G) KPCA (H) KPCA.C tumor-bearing mice with triple agents of Prexasertib plus anti-PD-L1 and anti-CTLA-4 combination therapies with or without anti-CD8 treatment. Data depicted are pooled from 2 independent experiments. (I) Experimental treatment strategy for mid-point immune analysis of omental tumor of KPCA and KPCA.C tumor-bearing mice treated with Prexasertib plus anti-PD-L1 and anti-CTLA-4 combination therapies compared to vehicle-matched control mice. A log-rank test compared the survival curves of individual groups to vehicle-matched control mice. $n=5$ or more/group, $*p<0.05$, $**p<0.001$, $***p<0.0001$. Data depicted are pooled from 3 independent experiments.

Supplemental Figure 5. Characterization of *Ccne1*-overexpressing ovarian mouse models related to Figure 5.

(A) Tumor-free mice (at least seven months post last therapy of Prexasertib plus anti-PD-L1 and anti-CTLA-4 combination, $n=6$) and tumor-naïve mice ($n=3$) were re-challenged with same KPCA cell line. A log-rank test compared Kaplan-Meier curves showing percent probability of survival of mice and the curves of individual groups to matched-control mice, $**p<0.001$. Sequence alignment result of (B) mutant *p53 R172H* to PCR amplified products (C) mutant *KRAS G12V* to PCR amplified products of KPCA, KPCA.C and KPCA.A cell lines. SnapGene 5.1 was used for the analysis. (D) Western blot analysis showing the expression of CCNE1, *KRAS^{G12V}*, Phospho-AKT (Ser473), Pan-AKT, Phospho-p44/42 MAPK (Erk1/2) and p44/42 MAPK (Erk1/2) in established ovarian cancer cell lines and KPCA, KPCA.C and KPCA.A cell lines. Vinculin served as a loading control. (E) Whole-exome analysis, including a comparison of the most prevalent single nucleotide variants (SNVs) of (left panel) KPCA.C vs KPCA cell lines and (right panel) KPCA.A vs KPCA cell lines. Note: some difference at the the single-nucleotide level between KPCA.A versus KPCA cells are denoted in blue, for more details refer to Supplemental Table 7. (F) Number of LOH events in the cell lines (G) Whole-genome copy-number profiles from Control-FREEC analysis are displayed, with red and blue points indicating 50kb windows with copy number greater than $2n$ or less than $2n$, respectively. (H) Western blot analysis showing expression of CHK1, phospho-RPA32 (S4/8), and phospho- γ H2A.X (Ser139) in KPCA, KPCA.C and KPCA.A cell lines upon Prexasertib or Niraparib treatment as indicated. β -actin served as a loading control. (I) Representative images showing Hematoxylin and eosin (H&E) staining and immunohistochemical analysis of indicated markers on harvested KPCA, KPCA.C and KPCA.A tumors. Scale bars: 200 μ m.

Supplemental Figure 6. Immune characterization of *Ccne1*-overexpressing ovarian mouse models and response to cell cycle checkpoint kinase- and immune checkpoint inhibitors related to Figure 5.

Immunophenotypic analysis by multi-parameter flow cytometry showing the frequency of live adaptive and innate immune cells in representative (A) Omental tumors and, (C) Ascites of KPCA and KPCA.C tumor-bearing mice. CD8 T-cell exhaustion status in representative (B) Omental tumors and (D) Ascites of KPCA and KPCA.C tumor-bearing mice. Data are presented as mean \pm SEM, $*p<0.05$, $**p<0.001$, $***p<0.0001$, Multiple t-test. $n=5$ or more/group. (E) Experimental treatment strategy for mid-point analysis. (F) Comparison of omental tumor weights of KPCA and KPCA.C tumor-bearing mice treated with Prexasertib plus anti-PD-L1 and anti-CTLA-4 combination therapies relative to vehicle-matched control mice. Data are presented as mean \pm SEM, $*p<0.05$, $**p<0.001$, $***p<0.0001$, Multiple t-test. $n=3$ or more/group.

Figure 6. Identification and ablation of Follistatin in *Ccne1*-overexpressing KPCA.C model to sensitize the tumor to cell cycle checkpoint kinase- and immune checkpoint-inhibitors.

(A) Bulk-tumor RNA-seq analysis showing enrichment of distinct hallmark terms in *Ccne1*-overexpressing ovarian models. The figure shows the categories enriched in each comparison. The x-axis shows the normalized enrichment score. Gene sets are shown on the y-axis. The size of the dot represents the number of genes from the ranked list present on each gene set, and the color shows the FDR q-value. (B) UMAP plot of unbiased clustering the cellular components of merged KPCA and KPCA.C omental tumors, where each color-coded cluster represents one cell type/state. Inset relative composition of the clusters. Each point represents one cell that is colored by its cell type/state. (C) sc-RNA-seq analysis showing enrichment of distinct hallmark terms in *Ccne1*-overexpressing ovarian models. The figure shows the categories enriched in each comparison. The x-axis shows the normalized enrichment score. Gene sets are shown on the y-axis. The size of the dot represents the number of genes from the ranked list present on each gene set, and the color shows the FDR q-value. (D) Cancer cluster identified by sc-RNA seq of KPCA.C and KPCA omental tumors, depicting genes upregulated in KPCA.C tumors versus KPCA tumors. (E) Follistatin concentration in cell culture supernatants taken from KPCA and KPCA.C cell lines and, KPCA.C *sgFstKO* single-cell clones. (F) *In situ* hybridization of Follistatin on omental tumor sections derived from KPCA and KPCA.C ovarian models using RNA-scope methodology (Pink= Follistatin). Scale bars: 200 μ m. (G) Experimental treatment strategy for mid-point analysis (H) Comparison of omental tumor weights of untreated and Prexasertib plus anti-PD-L1 and anti-CTLA-4 combination therapy treated KPCA.C or KPCA.C *sgFstKO* cohorts. (I) Kaplan-Meier curves showing percent probability of survival of mice injected with KPCA.C or KPCA.C *sgFstKO* cell line upon indicated treatment. A log-rank test compared the survival curves of individual groups to vehicle-matched control mice. n=5 or more/group, *p<0.05, **p<0.001, ***p<0.0001. Data depicted is pooled from 2 independent experiments. (J) Follistatin concentration in cell culture supernatants taken from KPCA and KPCA.A cell lines and, KPCA.A *sgFstKO* single-cell clones. *In situ* hybridization of Follistatin on omental tumor section derived from KPCA.A ovarian model using RNA-scope methodology (Pink= Follistatin). Scale bar: 200 μ m. (K) Experimental treatment strategy for mid-point analysis. (L) Comparison of omental tumor weights of untreated and Prexasertib plus anti-PD-L1 and anti-CTLA-4 combination therapy treated KPCA.A or KPCA.A *sgFstKO* cohorts. (M) Kaplan-Meier curves showing percent probability of survival of mice injected with KPCA.A or KPCA.A *sgFstKO* cell line upon indicated treatment. A log-rank test compared the survival curves of individual groups to vehicle-matched control mice. n=5 or more/group, *p<0.05, **p<0.001, ***p<0.0001. Data depicted is pooled from 2 independent experiments.

Supplemental Figure 7. Identification and ablation of candidate genes in the KPCA.C model to sensitize the tumor to cell cycle checkpoint kinase- and immune checkpoint-inhibitors related to Figure 6 and 7.

(A) UMAP plot of unbiased clustering the cellular components of merged KPCA and KPCA.C omental tumors, depicting the tumor genotypes, KPCA (blue) and KPCA.C (grey). Normalized RNA counts of CCL7, IL33, FST, Sparc, and S100a4 from (B) sc-RNA seq analysis from the cancer cluster of KPCA- and KPCA.C- omental tumors and, (C) RNAseq analysis of pre-implanted KPCA- and KPCA.C- cell lines. Kaplan-Meier curves showing percent probability of survival of mice injected with (D) KPCA.C or KPCA.C *sgIl33KO* cell line (E) KPCA.C or KPCA.C *sgS100a4KO* cell line upon indicated treatments. A log-rank test compared the survival curves of individual groups to vehicle-matched control mice. n=3 or more/group, *p<0.05, **p<0.001, ***p<0.0001. (F) Whole-genome analysis showing copy number variations at *Fst* loci in (left panel) KPCA.C and KPCA cell lines and (right panel) KPCA.A and KPCA cell lines. (G) Kaplan-Meier curves depicting overall survival (OS) grouped to High and Low by median FST mRNA expression

in patients with *CCNE1*-amplified HGSCs. (H) Kaplan-Meier curves depicting overall survival (OS) grouped to High and Low by median *FST* mRNA expression in patients with *BRCA1/2*-deficient HGSCs (see material and methods for details).

Figure 7. Epigenetic features and Follistatin overexpression in *Ccne1*-overexpressing model

(A) Schema depicting ATAC-seq experimental setup using KPCA, KPCA.C and KPCA.A cell lines. (B) Chromatin accessibility (ATAC-seq read pileups) in the *Fst* genomic region. Comparisons are shown for each peak and for all 4 peaks together. (C) Follistatin concentration in cell culture supernatants taken from KPCA and KPCA *Fst* overexpression (OE) cell lines. (D) Kaplan-Meier curves showing percent probability of survival of mice injected with KPCA or KPCA *Fst* OE cell line upon indicated treatment. A log-rank test compared the survival curves of individual groups to vehicle-matched control mice. $n=5$ or more/group, $*p<0.05$, $**p<0.001$, $***p<0.0001$. Data depicted is pooled from 3 independent experiments. (E) Bulk-tumor RNA-seq analysis showing enrichment of distinct hallmark terms in KPCA *Fst* OE and KPCA tumors. The figure shows the categories enriched in each comparison. The x-axis shows the normalized enrichment score. Gene sets are shown on the y-axis. The size of the dot represents the number of genes from the ranked list present on each gene set, and the color shows the FDR q-value. Cartoon models of (F) KPCA-responder and (G) KPCA.C-partial responder tumors depicting tumor immune-microenvironment and sensitization strategies. (H) Kaplan-Meier curves depicting progression-free survival (PFS) in patients with *CCNE1*-amplified HGSCs grouped to High and Low by median *FST* mRNA expression). (I) Kaplan-Meier curves depicting progression-free survival (PFS) in patients with *BRCA1/2*-deficient HGSCs grouped to High and Low by median *FST* mRNA expression (see material and methods for details).

Supplemental Table Legends

Supplemental Table 1. Nonlinear Regression Analysis (*in vitro* Drug assays) showing the IC50 values of engineered murine FTE-derived ovarian cancer cell lines upon treatment with Carboplatin, Cisplatin, Niraparib, Olaparib, Prexasertib, Birabresib (OTX-015), CPI-203 and JQ1. Related to Figure 1 and Supplemental Figure 1 and 2.

Supplemental Table 2. Collection of engineered murine-fallopian tube epithelial (m-FTE) cells and their tumorigenic potential (median survival in C57BL/6 mice, intraperitoneal route of administration). Related to Figure 2

Supplemental Table 3. CellRanger_Summary (scRNA analysis)- Figure 3A and 6B. Related to Figure 3 and 6

Supplemental Table 4. Top10 Markers (scRNA analysis) for Figure 3A Related to Figure 3 and 6

Supplemental Table 5. Top10 Markers (scRNA analysis) for Figure 6B Related to Figure 3 and 6

Supplemental Table 6. R code for scRNA seq analysis- Related to Figures 3A-B and 6B. Related to Figure 3 and 6

Supplemental Table 7. Whole-exome analysis for KPCA.A versus KPCA. The table contains the genes that are different at the single-nucleotide level between KPCA.A versus KPCA cells (denoted in blue in Supplemental Figure 5E). Related to Supplemental Figure 5.

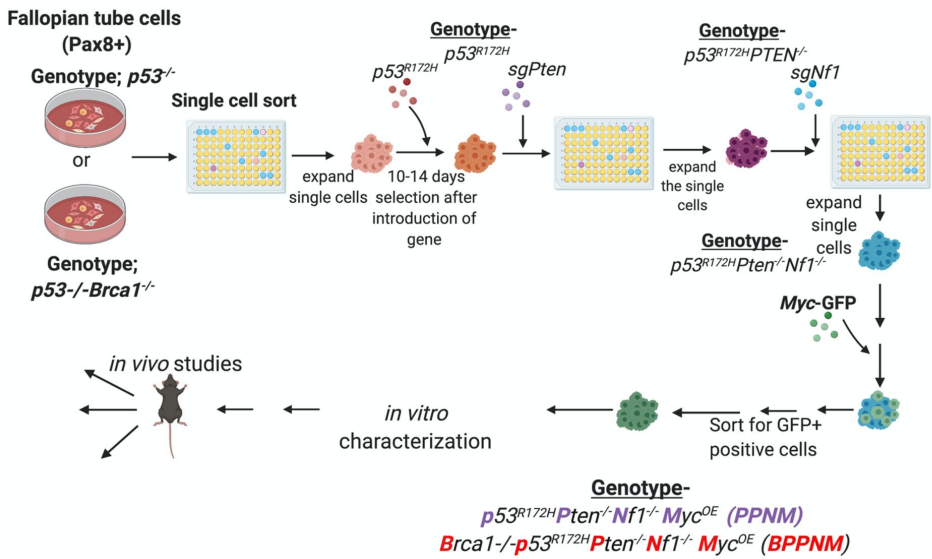
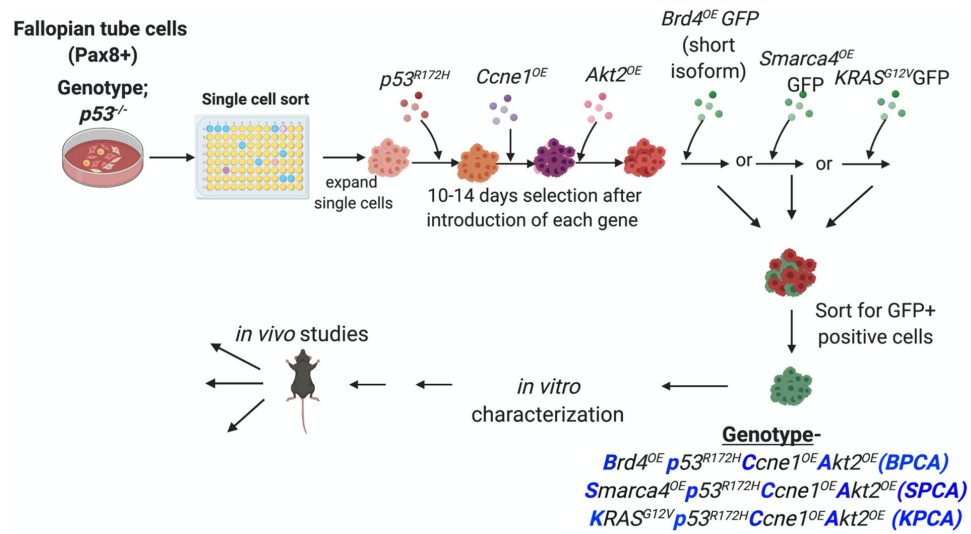
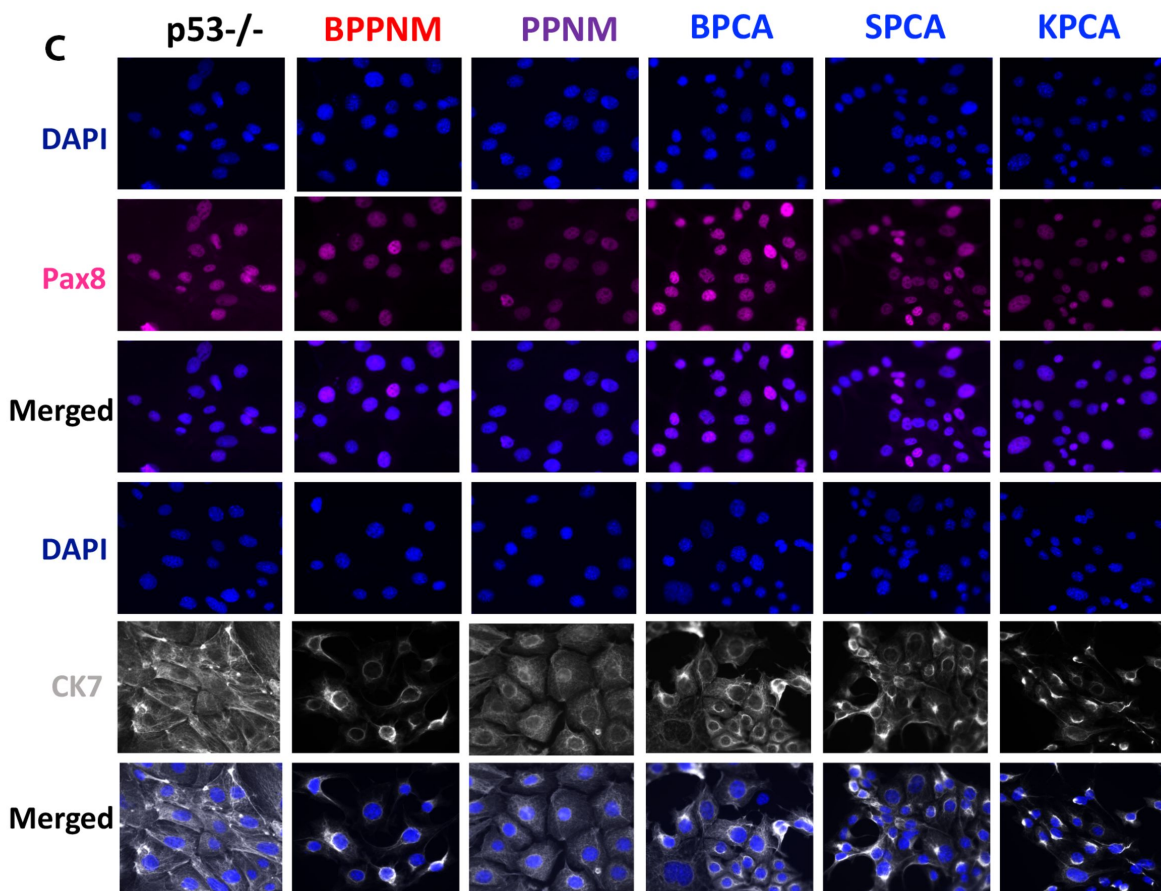
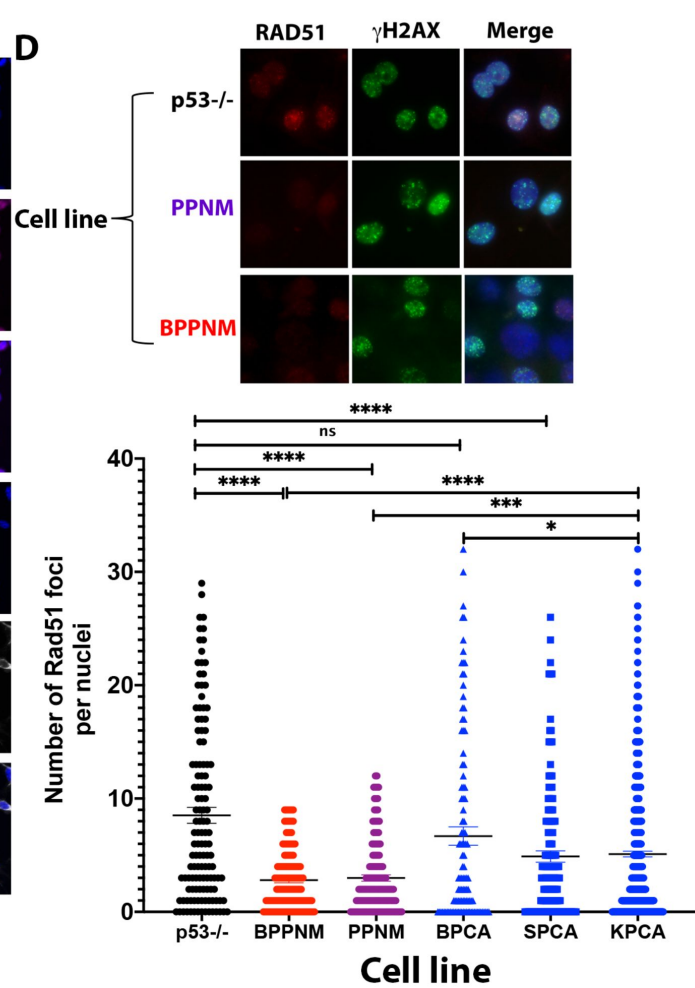
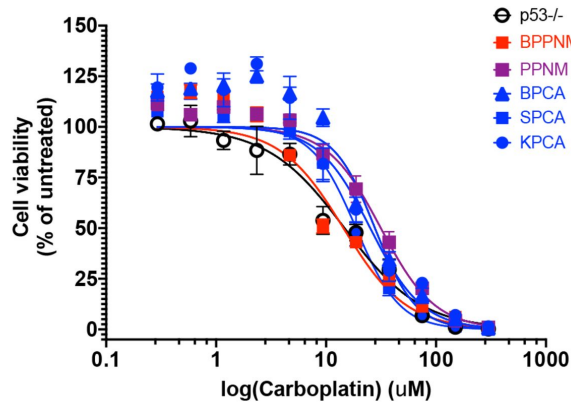
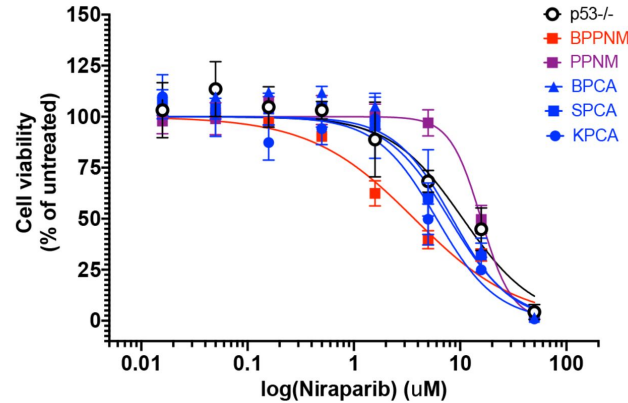
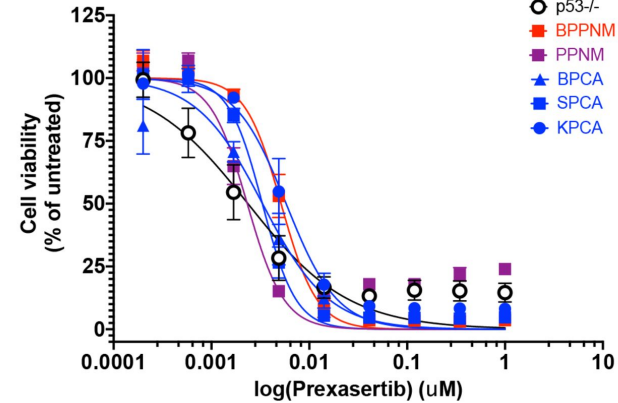
Figure 1**A****B****C****D****E****F****G**

Figure 2

A

Genotype-

BPPNM *Brca1^{-/-}p53^{-/-R172H}Pten^{-/-}Nf1^{-/-}Myc^{OE}*

PPNM *p53^{-/-R172H}Pten^{-/-}Nf1^{-/-}Myc^{OE}*

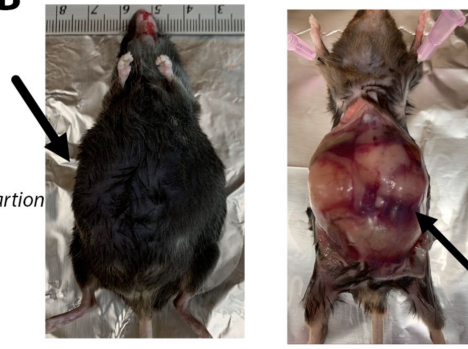
BPCA *BRD4^{short isoformOE}p53^{-/-R172H}Ccne1^{OE}Akt2^{OE}*

SPCA *SMARCA4^{OE}p53^{-/-R172H}Ccne1^{OE}Akt2^{OE}*

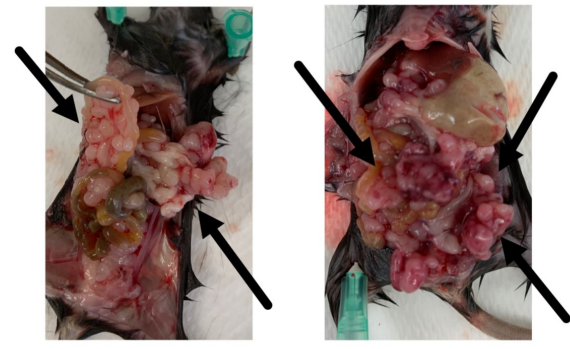
KPCA *KRAS^{G12V}p53^{-/-R172H}Ccne1^{OE}Akt2^{OE}*

in vivo
characterization

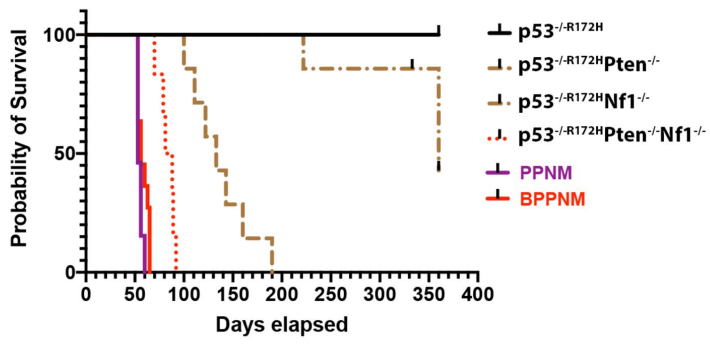
B **ASCITES**



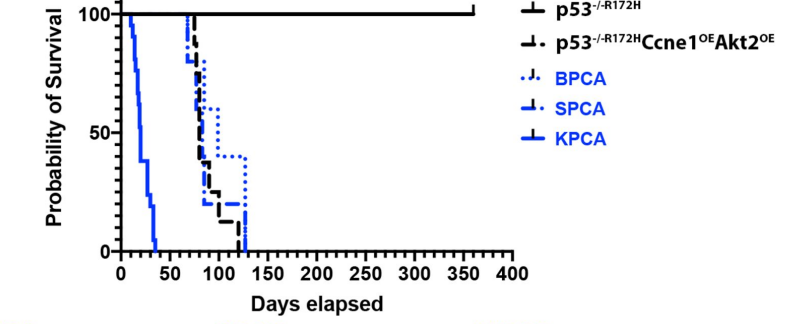
PERITONEAL METASTASIS



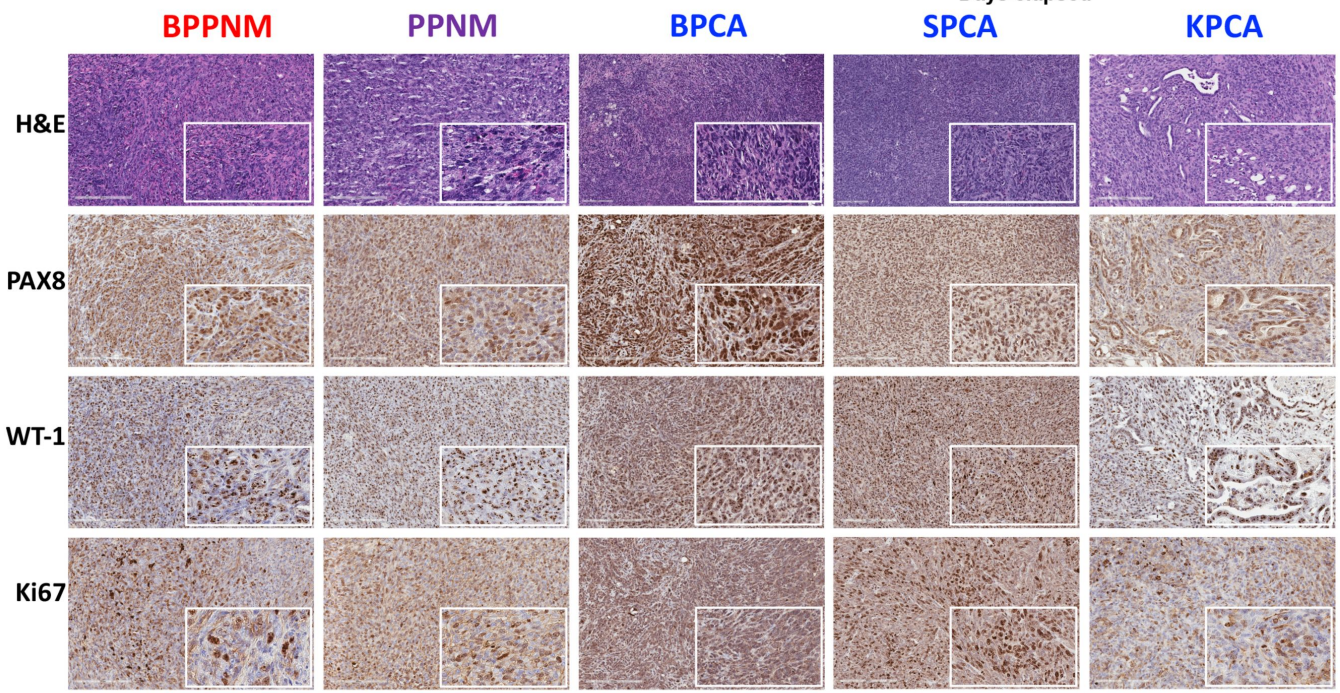
C



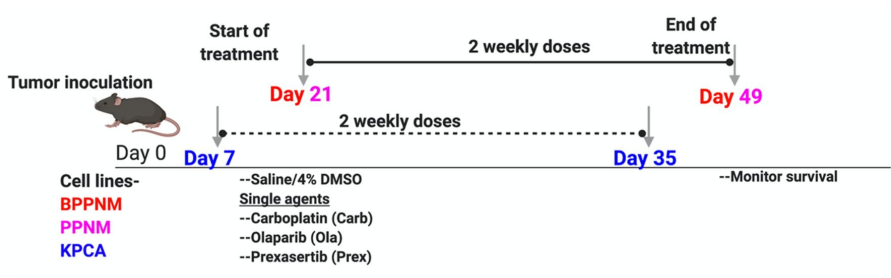
D



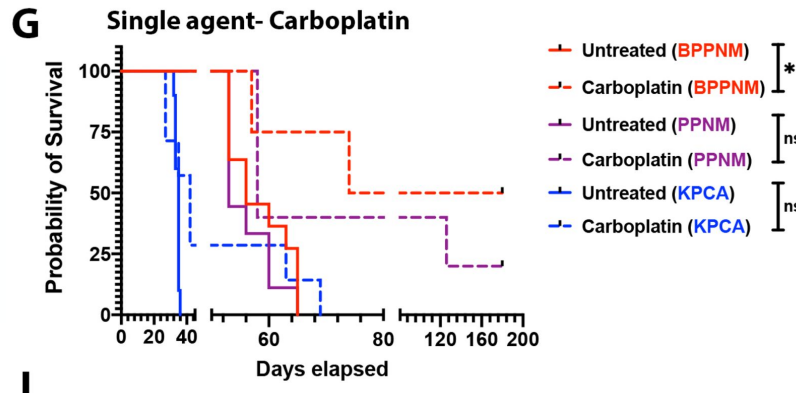
E



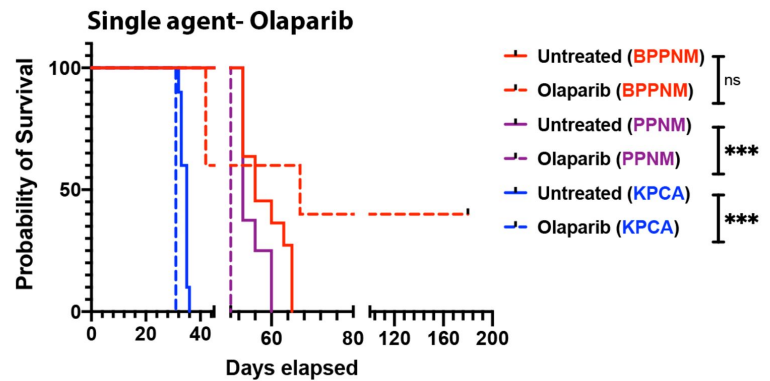
F



G



H



I

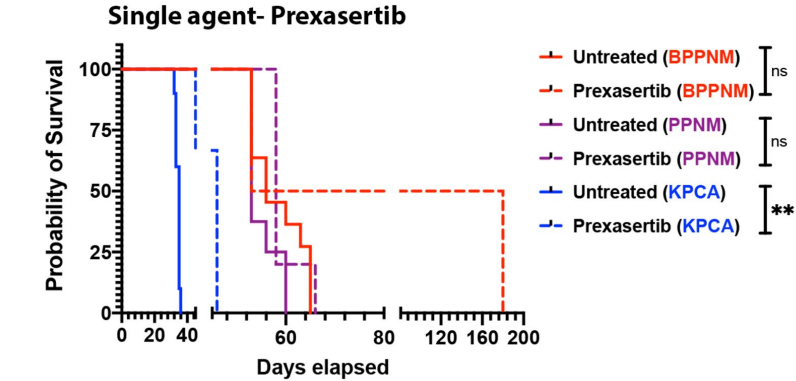


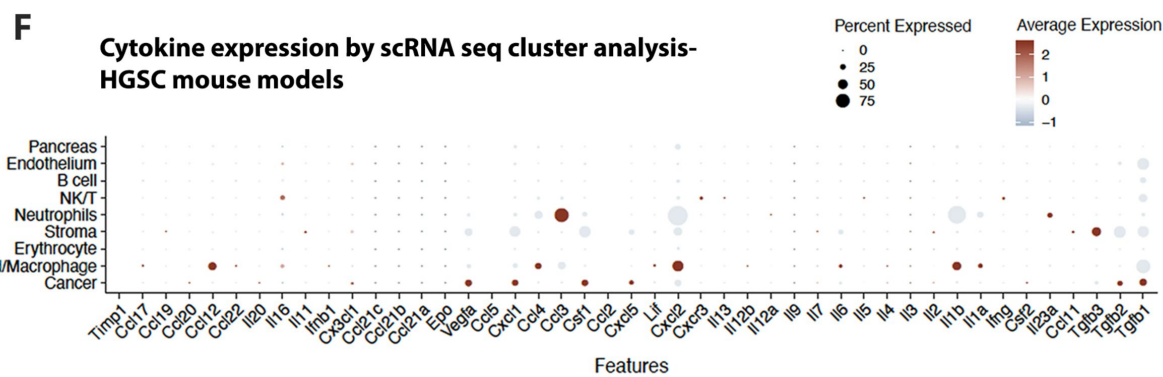
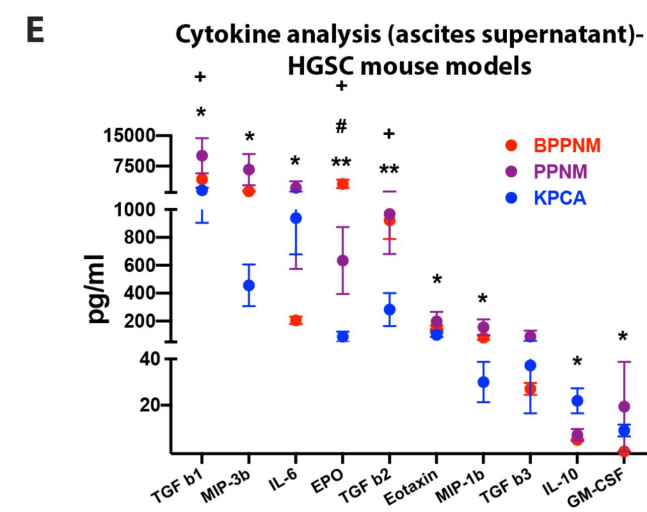
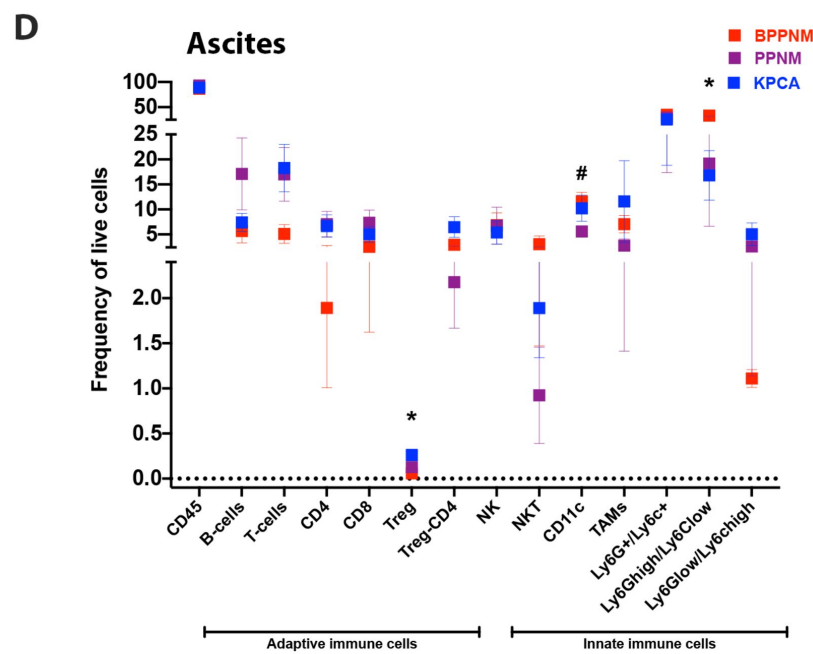
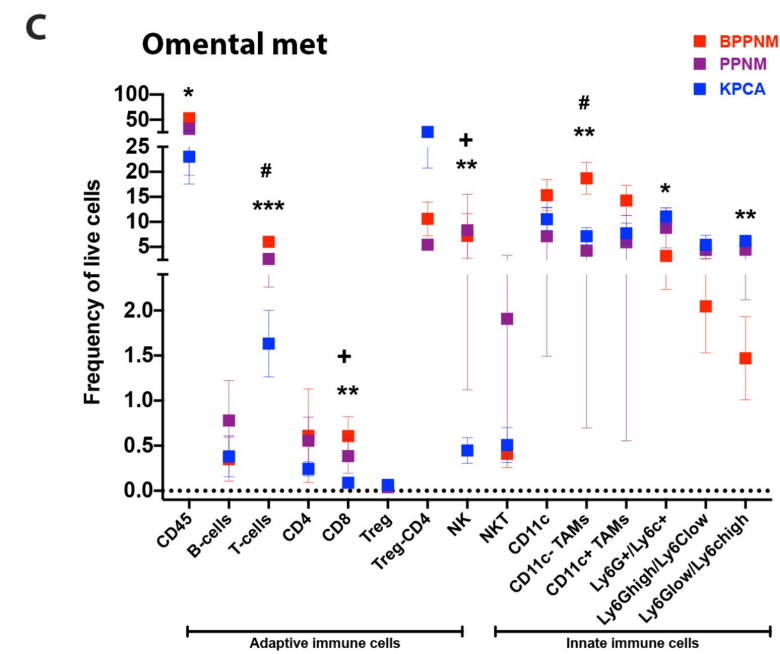
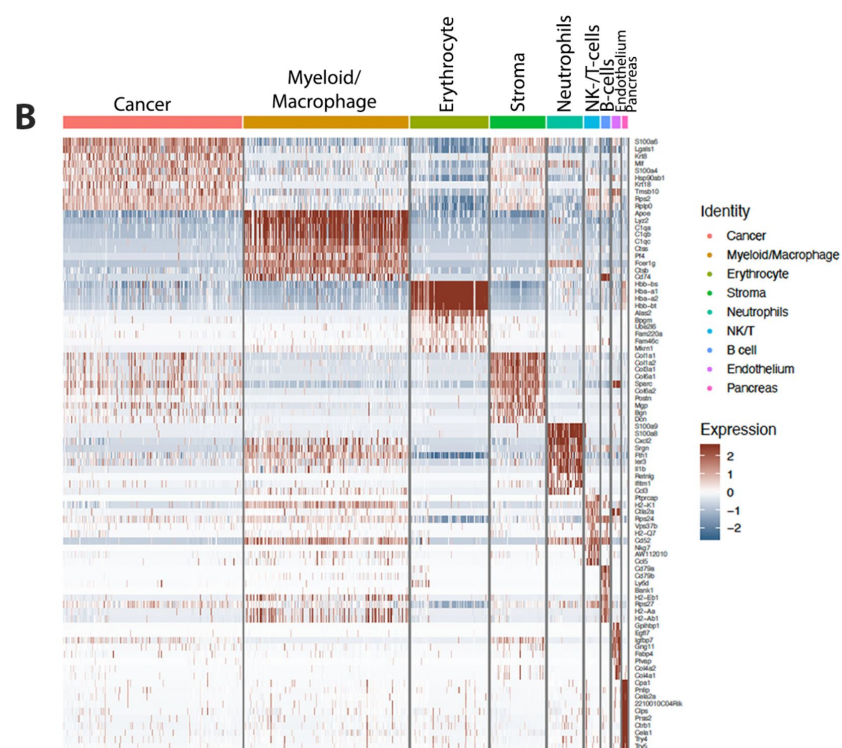
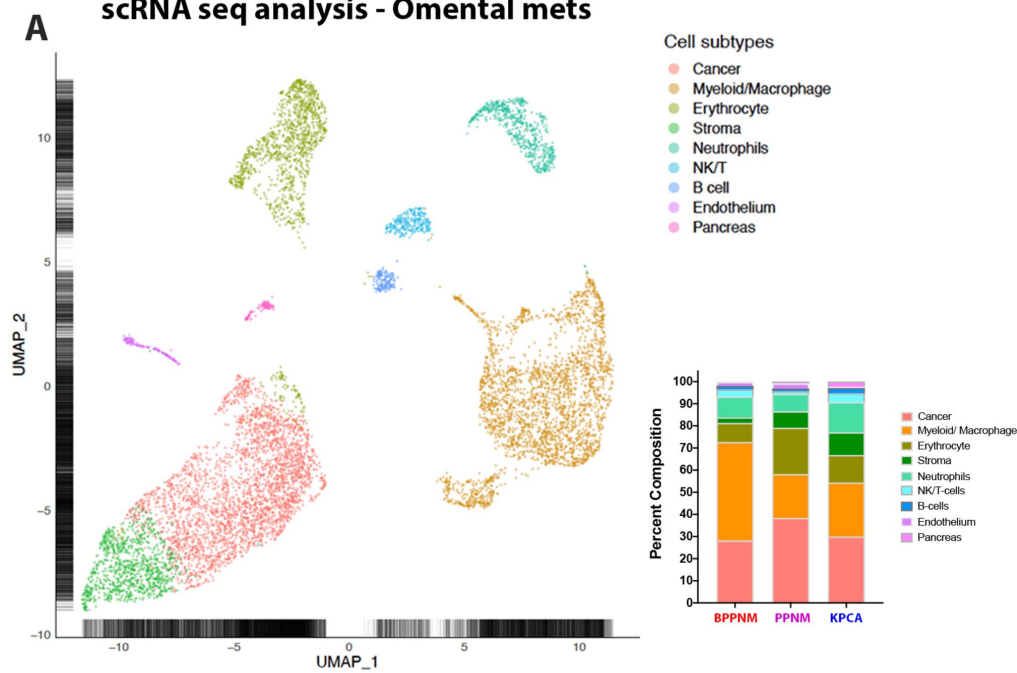
Figure 3**scRNA seq analysis - Omental mets**

Figure 4

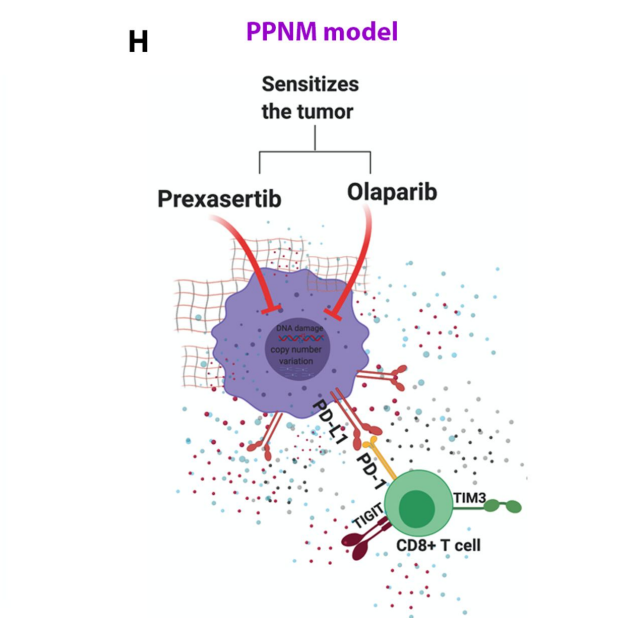
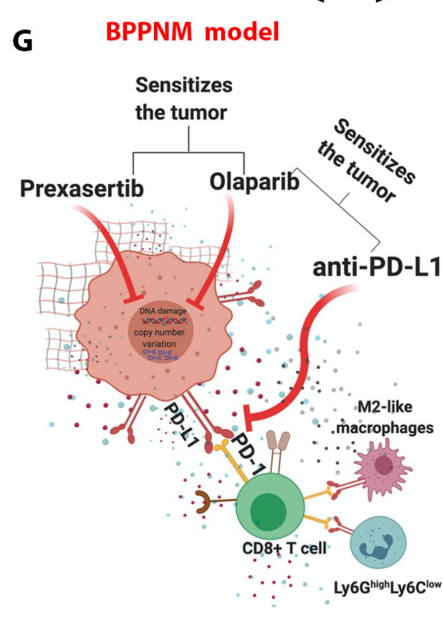
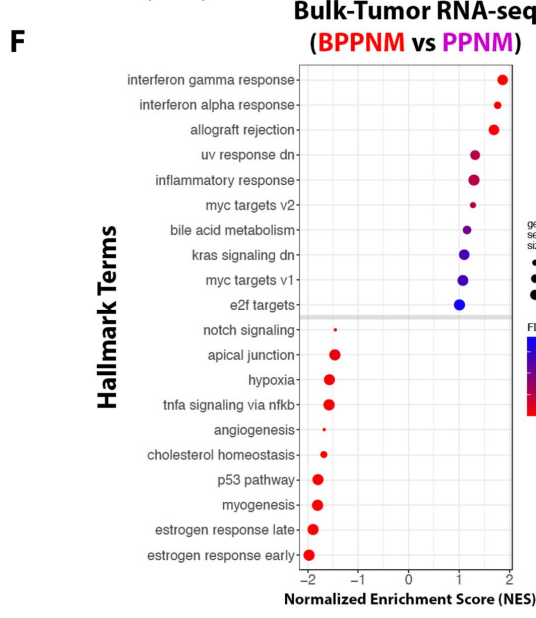
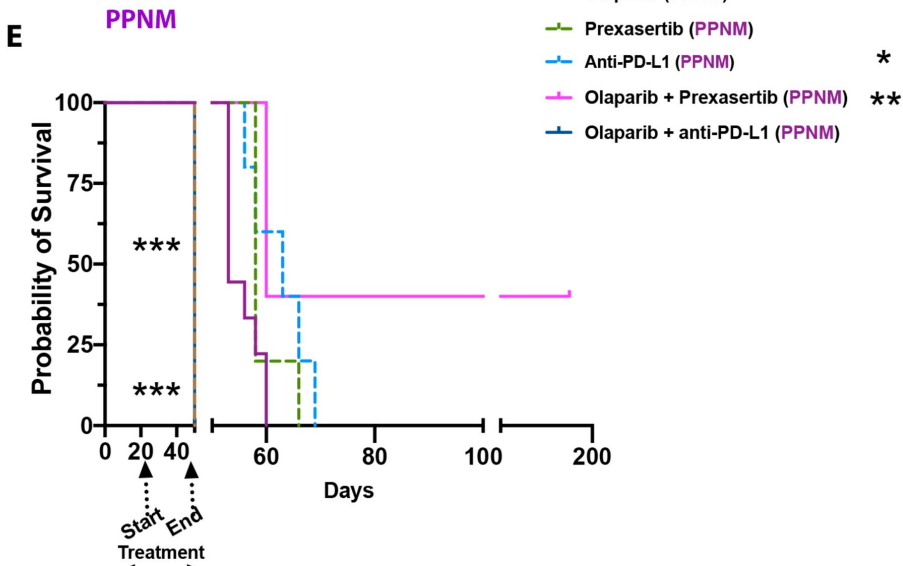
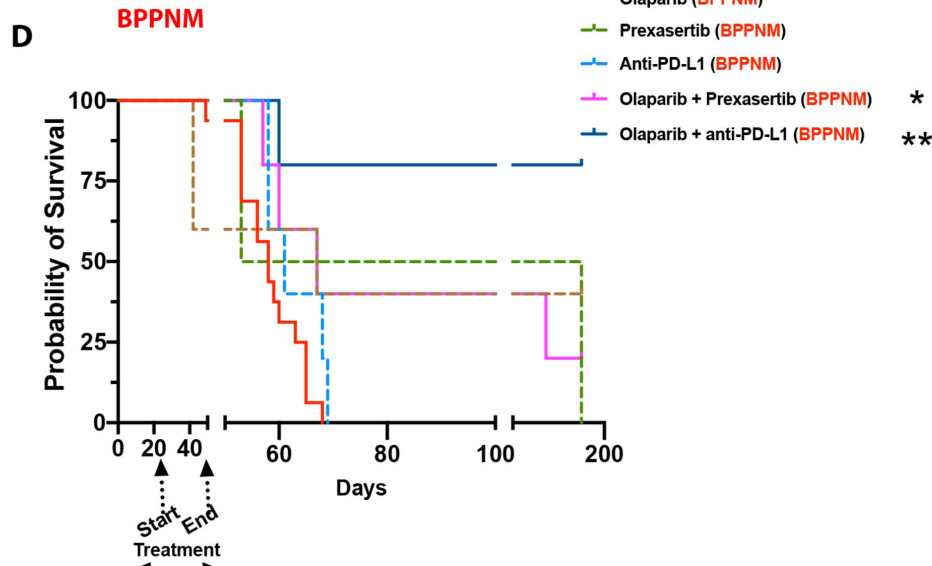
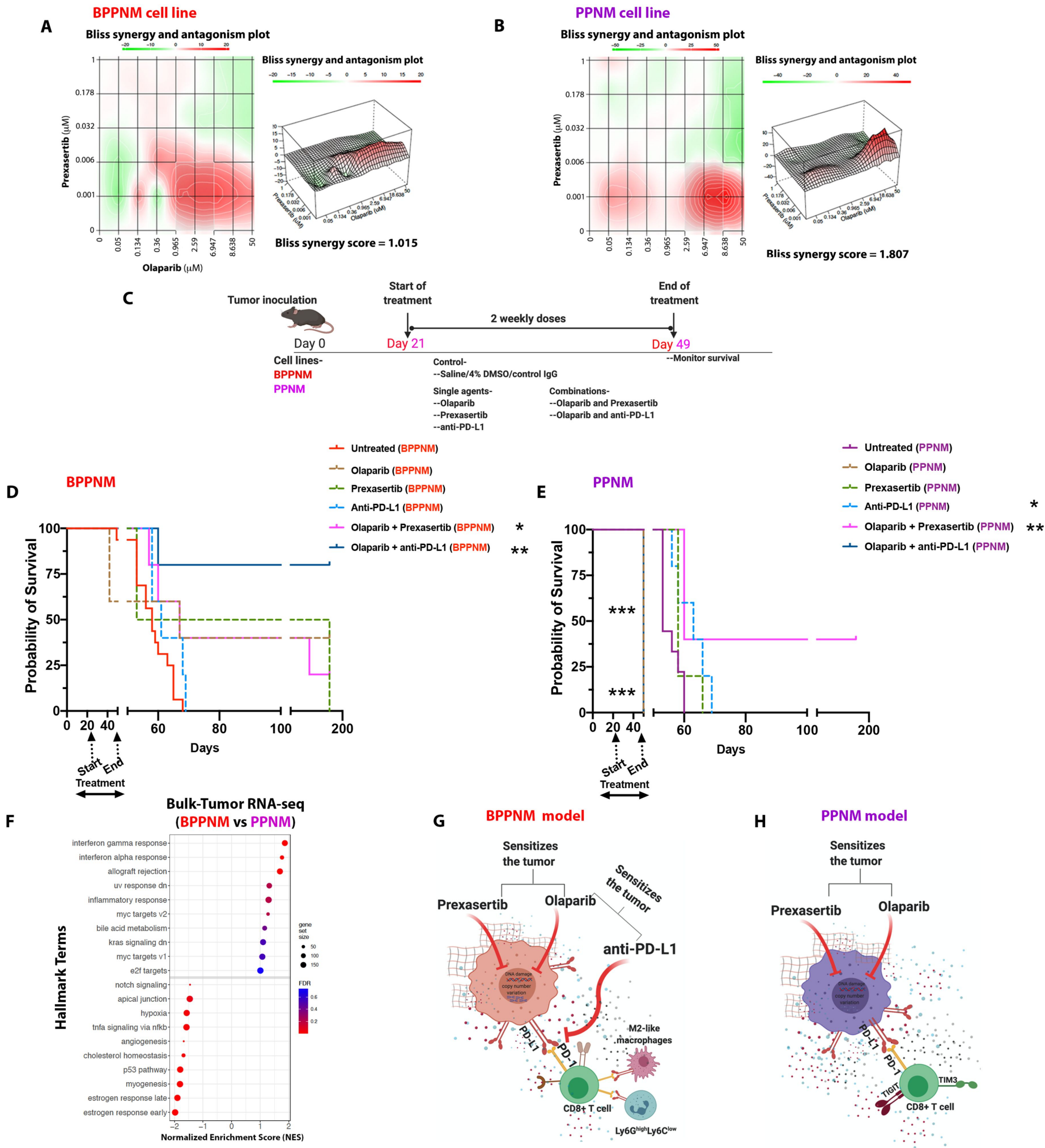
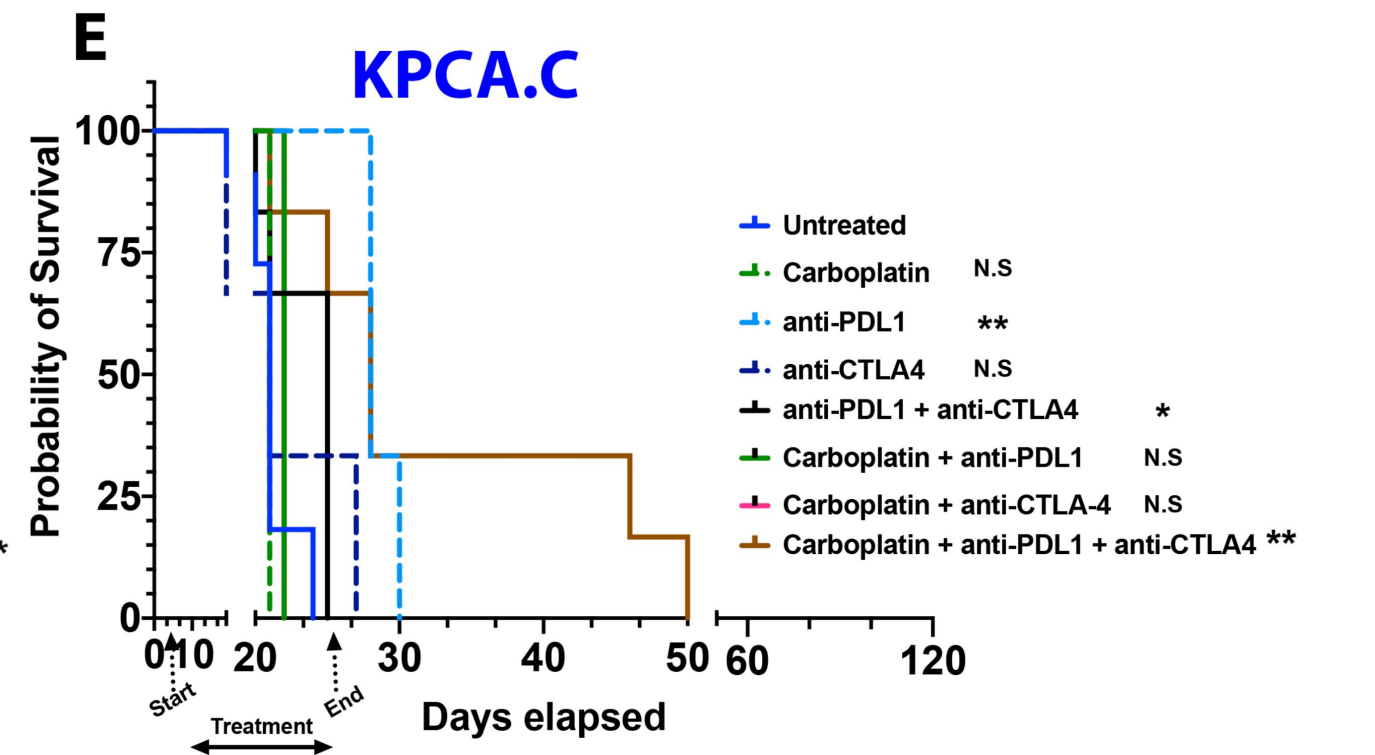
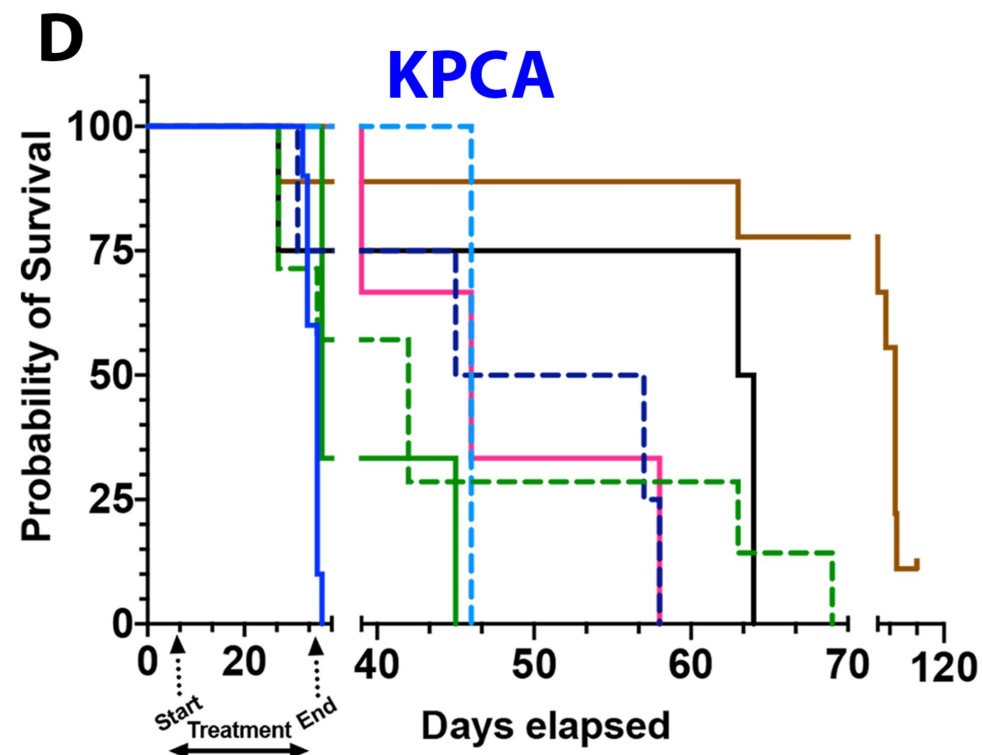
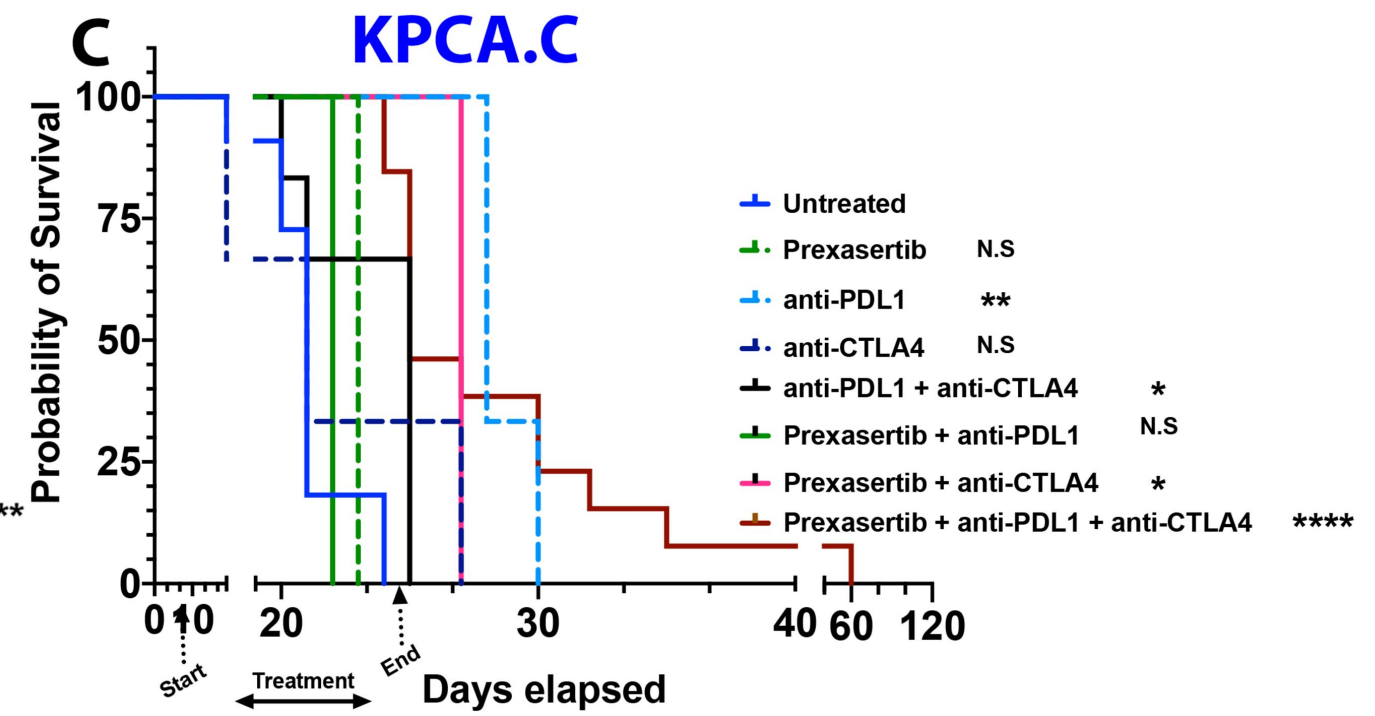
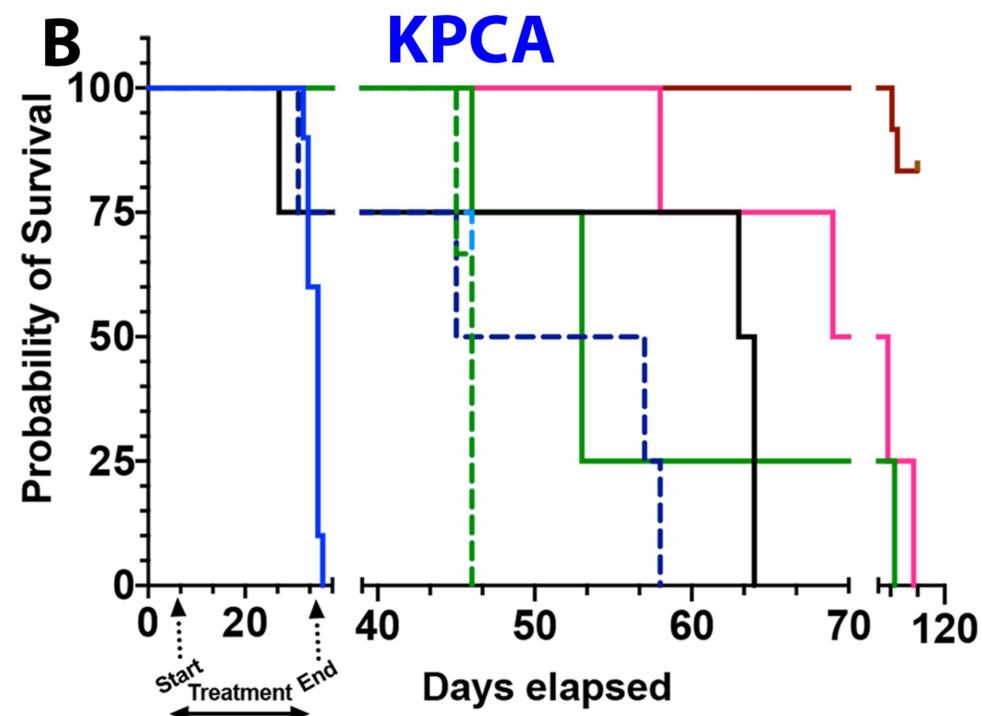
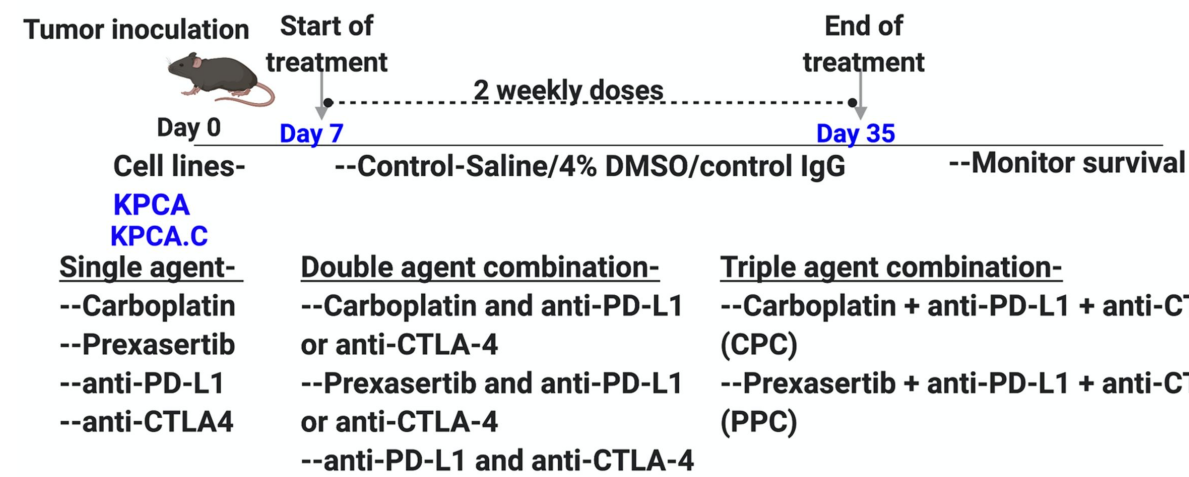
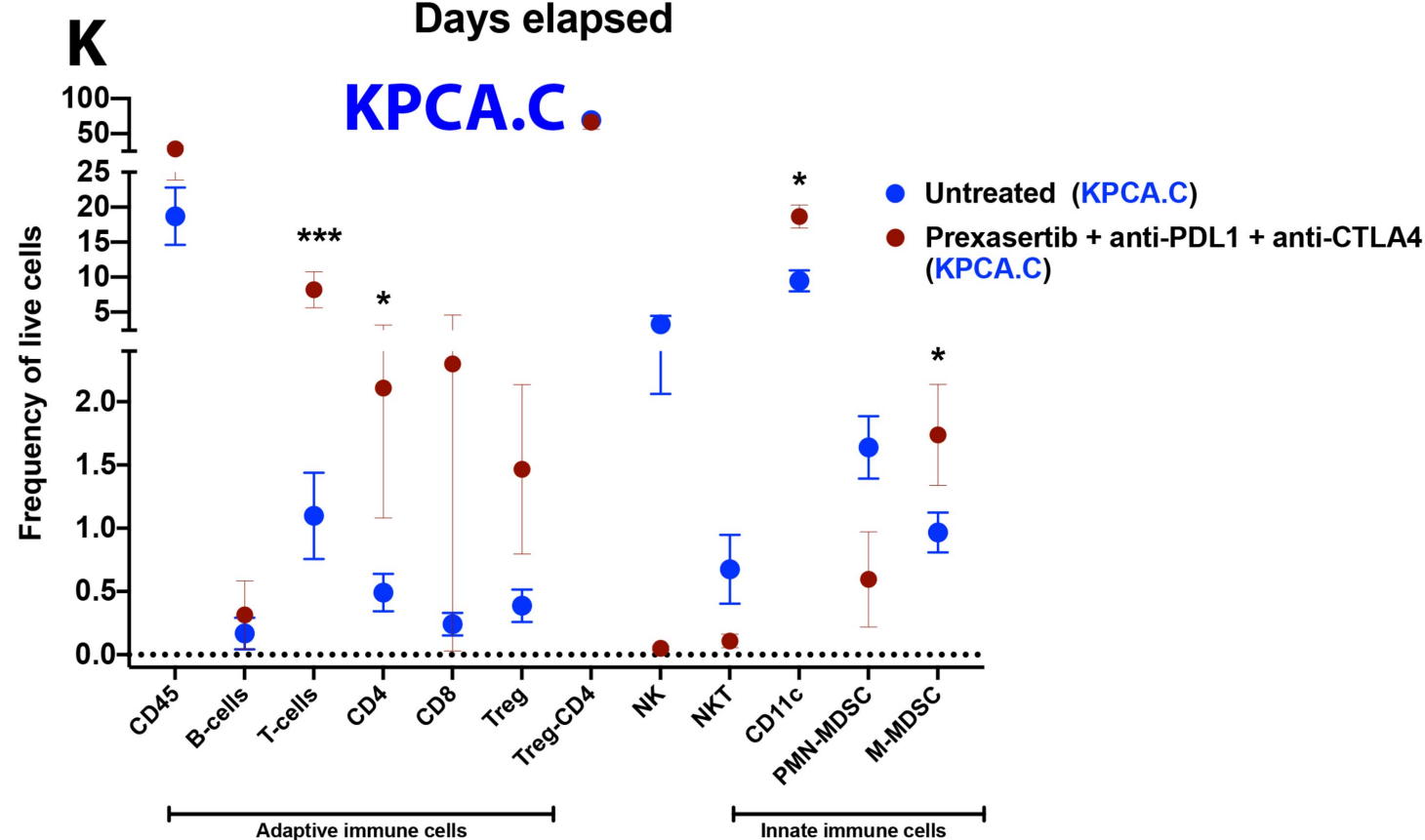
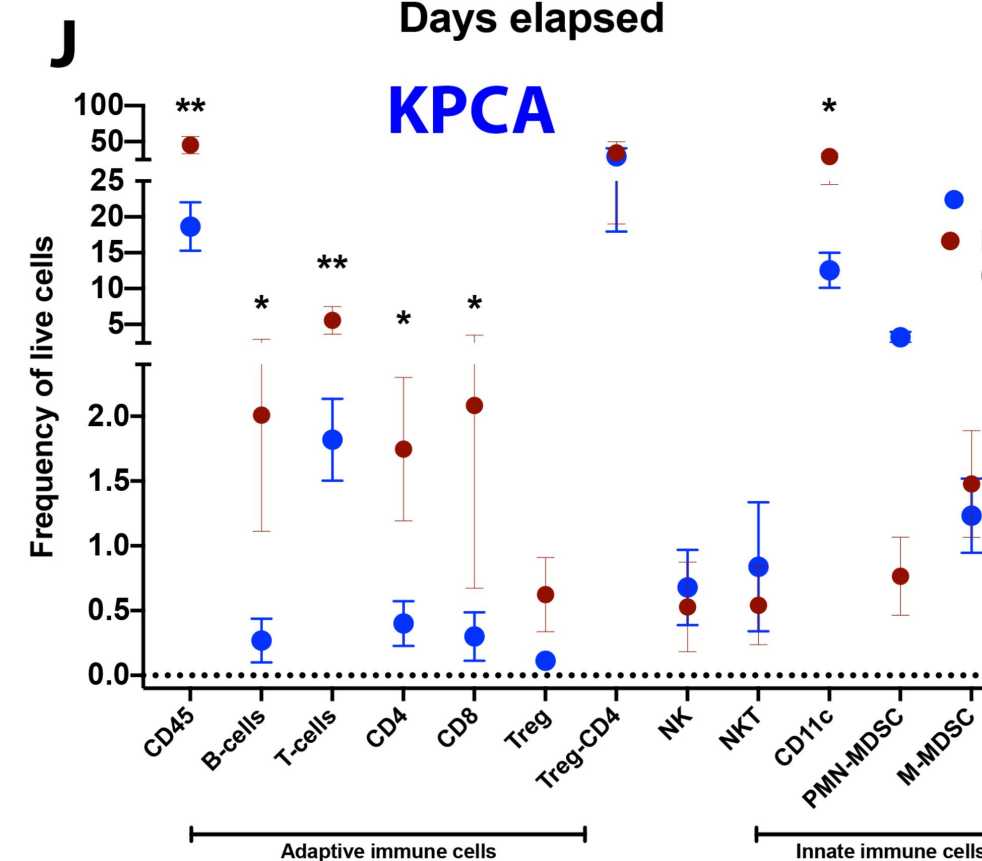
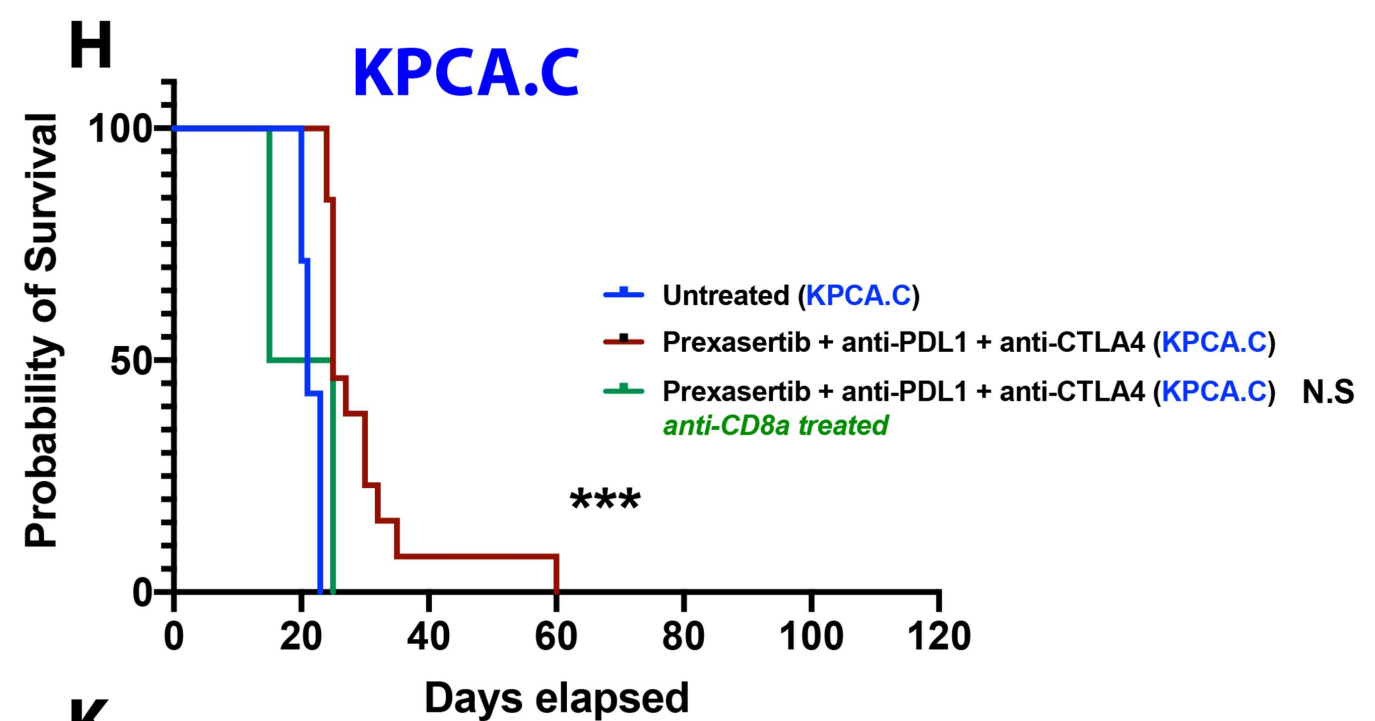
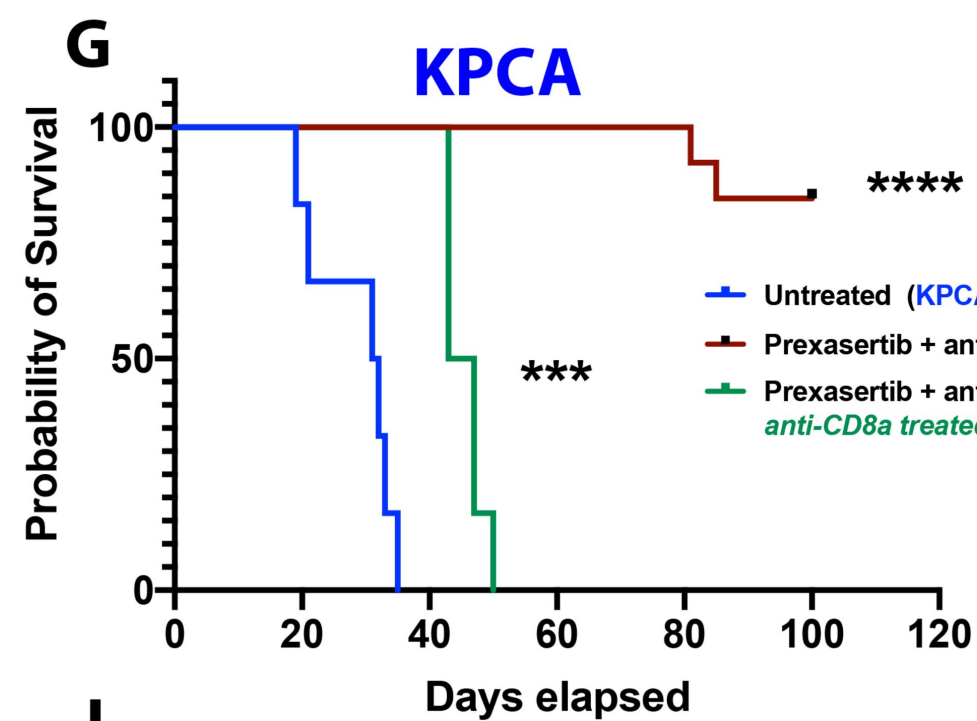
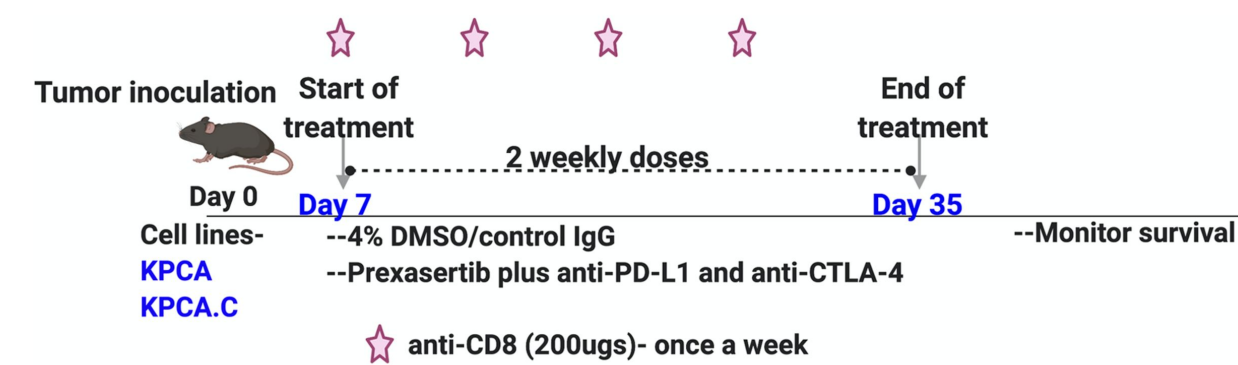


Figure 5

A



F



I

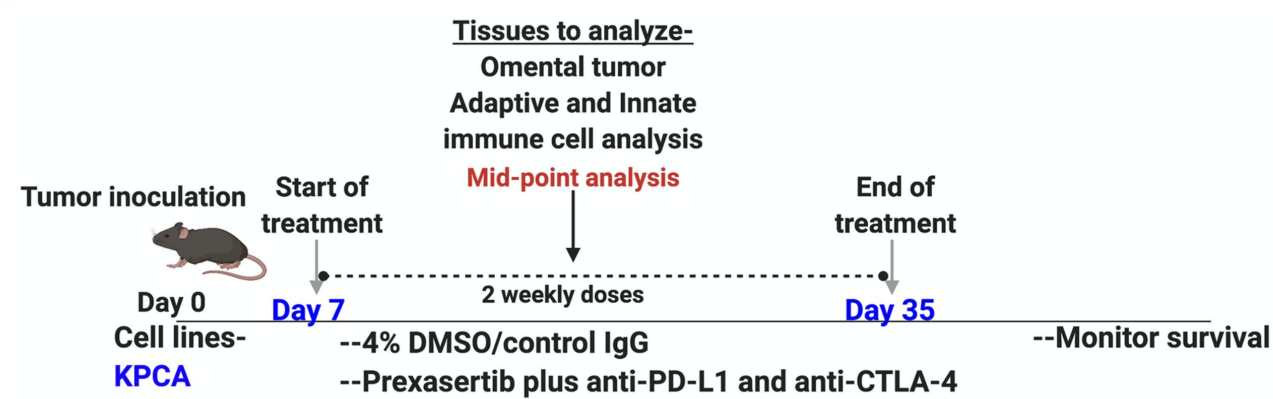


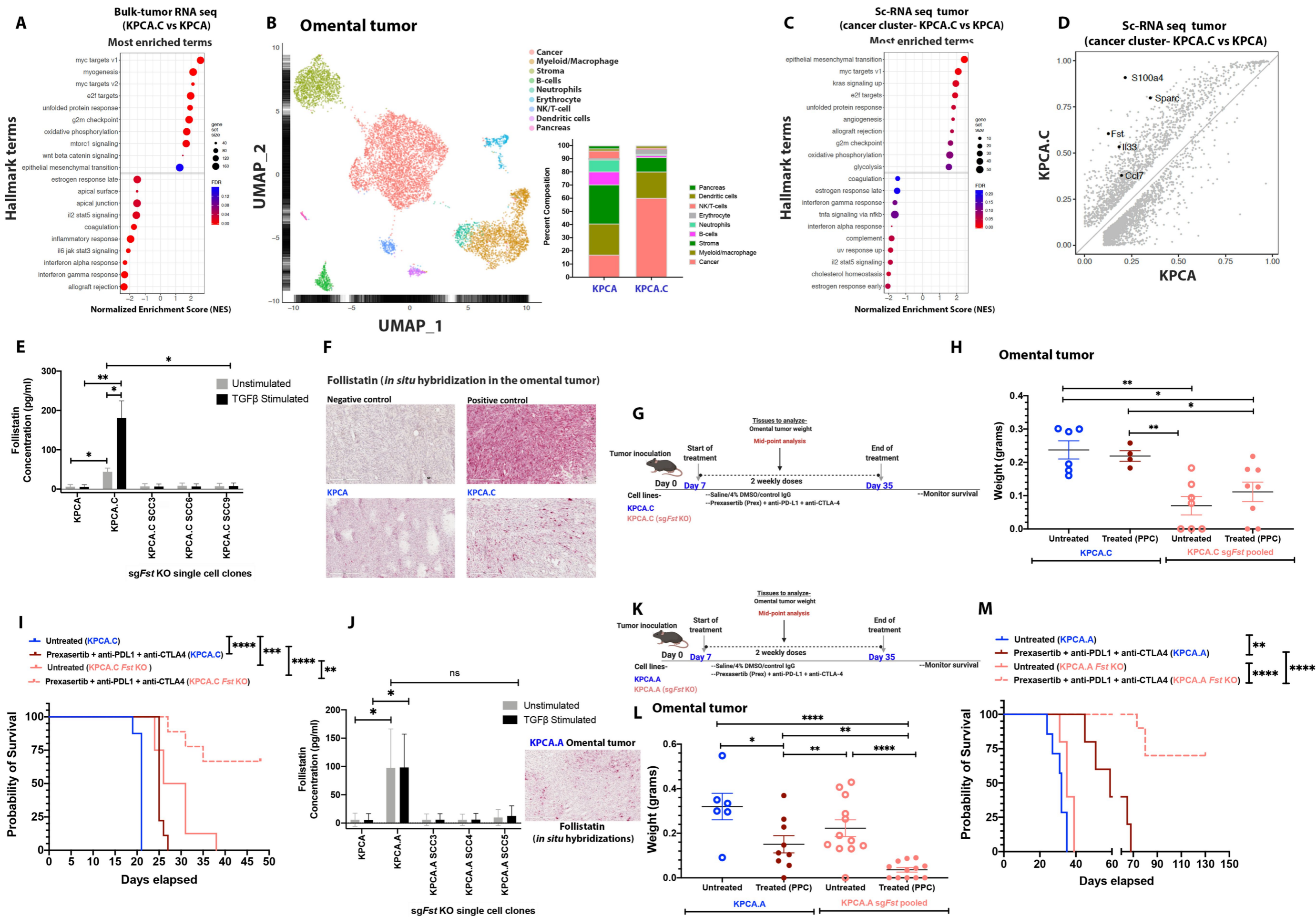
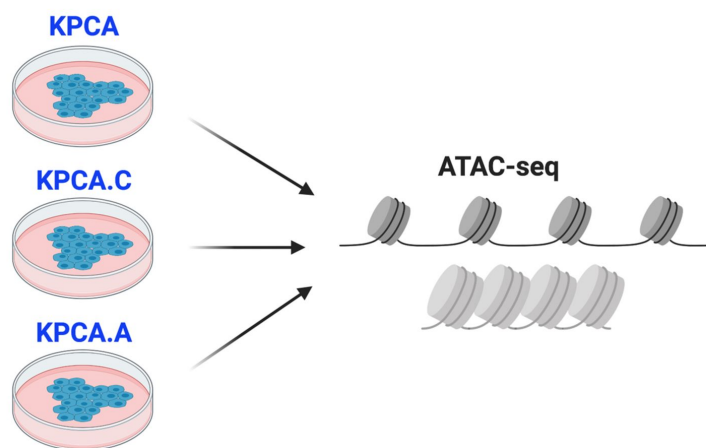
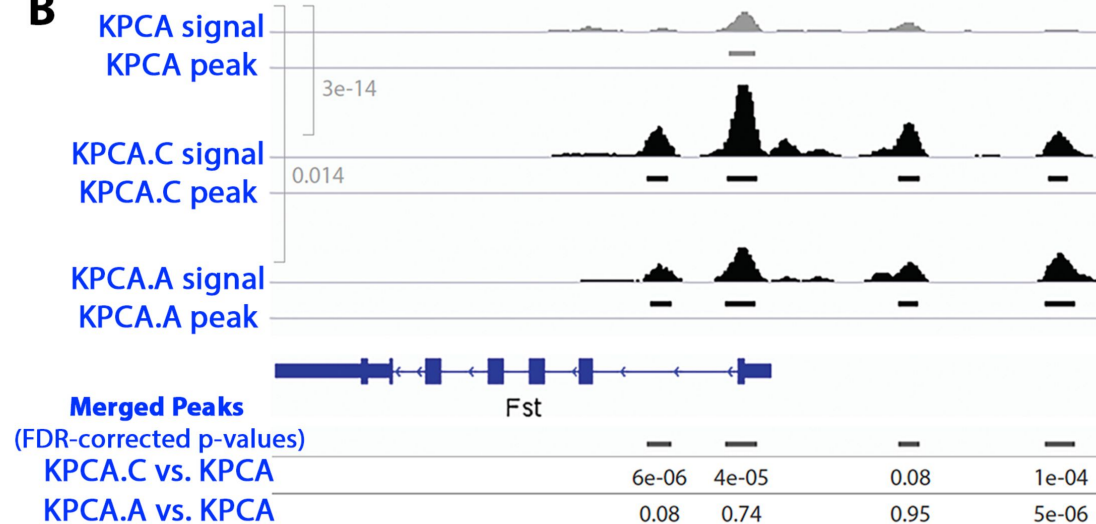
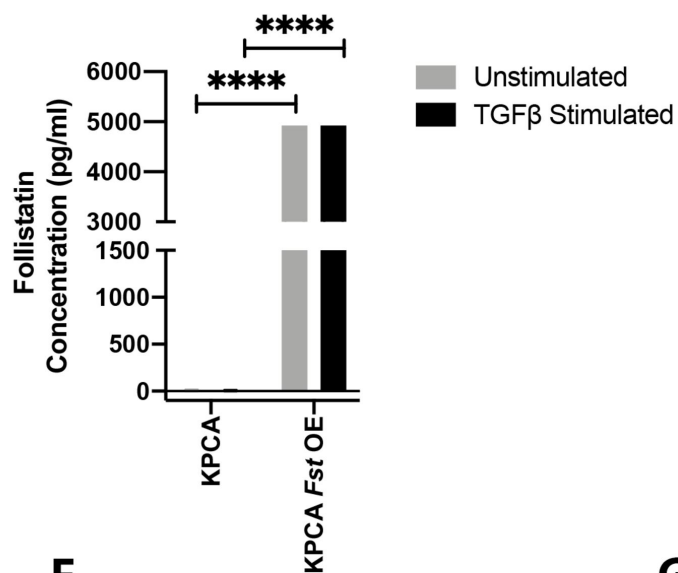
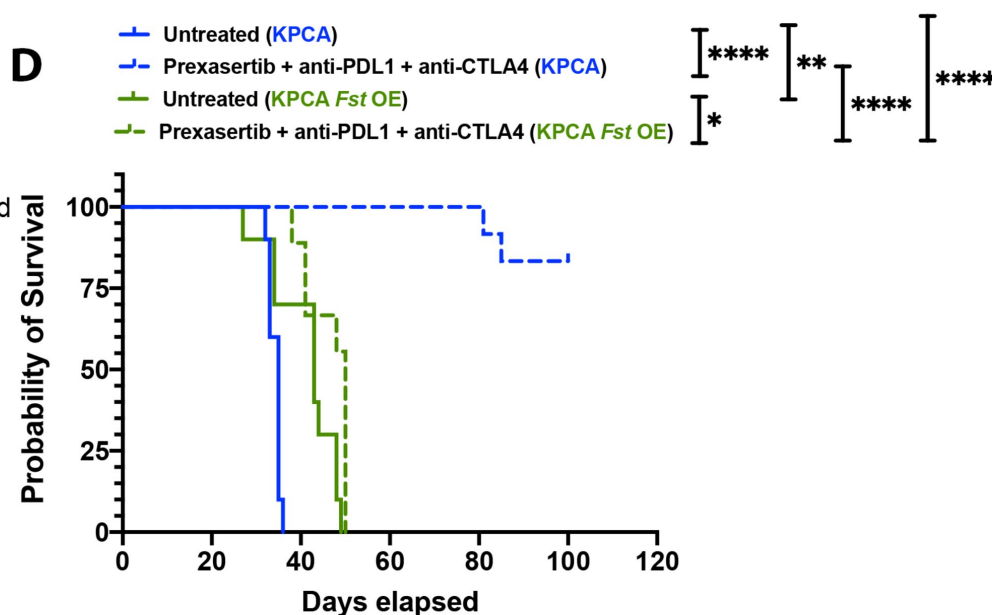
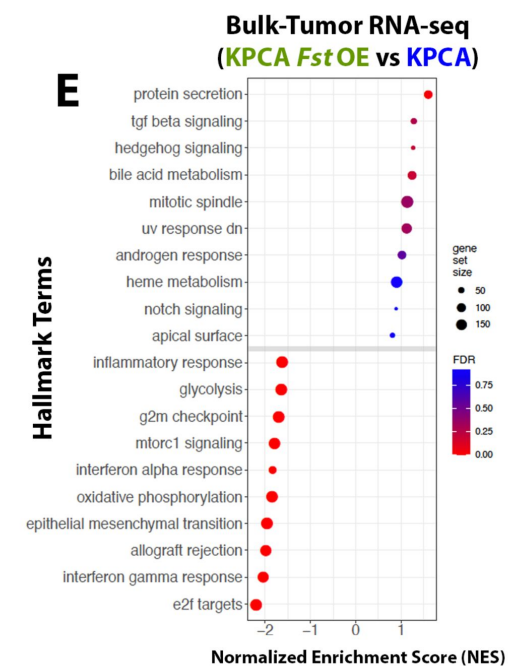
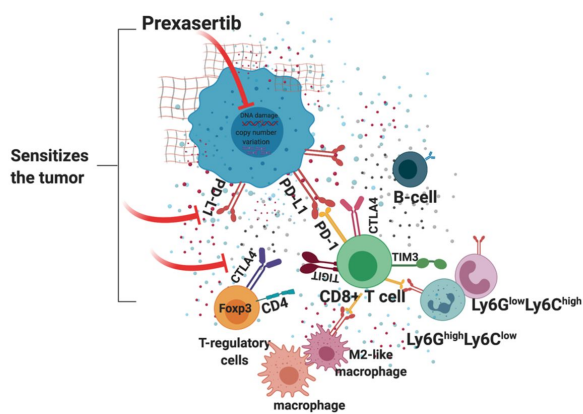
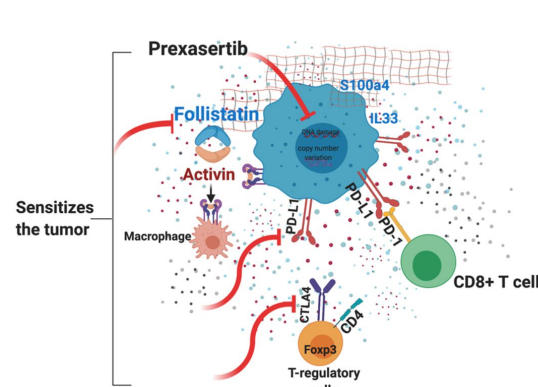
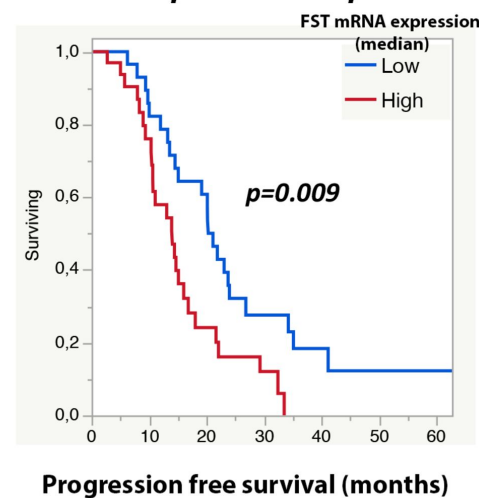
Figure 6

Figure 7**A****B****C****D****E****F****Responders: KPCA tumors****G****Partial-responders: KPCA.C tumors****H****CCNE1-amplified HGSC patients****I****BRCA1/2-deficient HGSC patients**